PREPARATION, CHARACTERIZATION AND ELECTRICAL PROPERTIES OF NANOCOMPOSITES BASED ON HYPERBRANCHED POLYMERS

vorgelegt von

M.Sc.

Shereen Said Shabaan OMARA

geboren in Kairo, Ägypten

von der Fakultät III – Prozesswissenschaften
der Technischen Universität Berlin

zur
Erlangung des akademischen Grades
Doktor der Naturwissenschaften
(Dr. rer. nat.)
genehmigte Dissertation

Promotionsausschuss:

Vorsitzender: Prof. Dr. rer. nat. **Walter REIMERS**

Gutachter: Prof. Dr.-Ing. **Manfred H. WAGNER**

Gutachter: Prof. Dr. rer. nat. **Andreas SCHÖNHALS**

Tag der wissenschaftlichen Aussprache: 02. Februar 2018

Berlin 2018

ACKNOWLEDGEMENTS

I would like to thank my supervisor Prof. Dr. Andreas Schönhals (Federal Institute for Materials Research and Testing BAM), for giving me the opportunity to work in his research group. It was a great experience. His guidance, helpful suggestions, encouragement, and patience helped me not only to successfully complete this thesis but also to develop my scientific knowledge, skills and attitude. I would like to express my sincere gratitude and real appreciation to Prof. Dr.–Ing. Manfred H. Wagner (Technical university of Berlin), for being my supervisor at the university and for his support and many valuable suggestions and his support.

I am grateful to the Ministry of Higher Education and scientific research of the Arab Republic of Egypt "MHESR" for the financial support.

I particularly want to thank Prof. Dr. Gamal M. Turky, Prof. Dr. Ahmed Ghoneim, and Prof. Dr. Mona H Abdel Rehim (National Research center NRC, Egypt), for suggesting the point of research, and continuous guidance and encouragement.

Furthermore, I would like to thank Prof. Dr. Andreas F. Thünemann, for his help with the SAXS measurements. Meanwhile, I would to thank the helps from MSc. Sherif Madkour, for the AC measurements and multiple hours spent in discussions. I would like to take this opportunity to thank Dr. Haujie Yin, for his encouragement and discussion.

I would like to thank all my colleagues in BAM for their kind help and co-operation. Thanks for your time in the four years. Mr. Neubert is thanked for the DSC measurements.

I am grateful to all my family. Special thanks to my parents, my husband Hosam Goda, my children Bassel, Lamar and the little one Lugein, for their moral support, encouragement, and for everything they did for me. Further, I would like to thank all my good friends in and out of Berlin for their love, and support.

A final praise goes out to the Lord my God (ALLAH) who is my source and has provided me with a community of friends and family that has made my life so enjoyable and worthwhile. I know and avow that without Him I cannot do anything.

ZUSAMMENFASSUNG

Nanokomposite, die auf hyperverzweigten Polymeren (englisch: hyperbranched polymers; HBP) und Schichtsilikate als Nanofüllstoff basieren, sind eine relativ neue Klasse von Hybridmaterialien. Aufgrund ihrer guten physikalischen/chemischen Eigenschaften weckten sie das Interesse der Wissenschaft. Diese Arbeit versucht, ein besseres Verständnis der Beziehung zwischen der Struktur, der Dynamik und den Eigenschaften für verschiedene Typen von HBP/Kaolinit (Ka)-Nanoverbundwerkstoffen zu liefern.

Zur Präparation verschiedener Systeme von HBP/Ka-Nanoverbundwerkstoffen wurden zwei verschiedene Methoden angewandt. Die erste Methode war eine ‘‘ex situ’’-Methode, bei dem das Polymer mit Ka gemischt wurde, welches zuvor mit Dodecylamin (DCA) modifiziert wurden was Die zweite Methode war ein ‘‘in situ’’ -Ansatz, eine polymerisations-basierte Methode. Bei diesem Vorgehen wurden die Ka-Schichten durch das flüssige Monomer verändert und danach fand die Polymerisation des Polymers zwischen den Ka-Platten statt. Die Struktur-Eigenschafts-Beziehung der HBPs und der Nanoverbundwerkstoffe wurden durch eine Kombination aus Dynamischer Differenzkalorimetrie (DSC), Fourier-Transformations-Infrarotspektroskopie (FTIR), Röntgenkleinweitwinkelstreuung (SAXS), Transmissionselektronenmikroskopie (TEM) und Spezifischer-Wärmespektroskopie (SHS) untersucht. Die molekulare Dynamik wurde mit Hilfe der dielektrischen Spektroskopie (BDS) studiert. Die dielektrischen Spektren wurden für alle Proben bei hohen Temperaturen durch den Beitrag der Leitfähigkeit dominiert.

Als erstes System wurden hyperverzweigte Polyamine Ester (HPAE)/Ka-Nanoverbundwerkstoffe hergestellt. Die in situ Polymerisations-Methode führte zu einer interkalierten Morphologie, wogegen die ex situ-Methode zu einer exfolierten Struktur führte, was mittels SAXS und TEM nachgewiesen wurde. Aufgrund des starken Beitrags der Leitfähigkeit zum dielektrischen Verlust ist die segmentale Dynamik überdeckt und kann lediglich durch die SHS aufgelöst werden. Eine Entkopplung der segmentalen Dynamik und der Leitfähigkeit wurde durch einen Vergleich zwischen den Temperaturabhängigkeiten der entsprechenden

Relaxationszeiten gezeigt. Diese Entkopplung wurde mit sinkender Fragilität schwächer.

Als zweites System wurden hyperverzweigte Poly(amidoamine) (HPAMAM)/Ka-Nanoverbundwerkstoffe mittels der in situ-Polymerisation und der ex situ-Methode hergestellt. Mit der zweiten Methode wurde eine teilweise exfolierte Struktur der Nanoverbundwerkstoffe erhalten, während die erste Methode zu einer exfolierten Morphologie führt. Für die HPAMAM/Ka-DCA-Nanoverbundwerkstoffe zeigen die Ergebnisse, dass mit steigender Konzentration des Nanofüllmaterials die DC-Leitfähigkeit um 4 Größenordnungen ansteigt. Ferner wurde für alle Proben eine signifikante Trennung der Temperaturabhängigkeit der Relaxationszeit bzgl. der Leitfähigkeit und der segmentalen Dynamik beobachtet. Das Phänomen der Entkopplung des Leitfähigkeitsmechanismus wurde im Detail diskutiert.

Im letzten Teil der Arbeit wurden hyperverzweigt Polyester Amide (Hybrane S 1200®)/Ka-DCA Nanokomposite mittels der ex situ-Methode herstellt. SAXS- und TEM-Messungen zeigen, dass das Ausmaß der Exfolierung von der Konzentration von Ka-DCA abhängt. Für die Hybrane /Ka-DCA Nanokomposite mit 10 und 20 wt-% Ka-DCA wurde eine exfolierte Struktur nachgewiesen, während eine teilweise interkalierte Struktur für Nanoverbundwerkstoffe mit 30, 50 und 70 wt-% der Nanofüllstoffe beobachtet wurde. DSC-Messungen zeigen eine Verringerung der Glasübergangstemperatur T_g bei Erhöhung des Ka-DCA-Anteils. Die dielektrischen Spektren von reinem Hybrane und des Nanoverbundwerkstoffes zeigen eine α-Relaxation bzw. einen dynamischen Glasübergang bei Temperaturen oberhalb T_g und eine β-Relaxation, die in Beziehung zu lokalisierten Bewegungen steht bei Temperaturen niedrigeren als T_g oder bei höheren Frequenzen als für die α-Relaxation. Der Relaxationsmechanismus und die DC-Leitfähigkeit wurden im Detail diskutiert.

ABSTRACT

Nanocomposites based on hyperbranched polymers (HBPs) and layered silicates as nanofillers are a relatively new class of nanocomposites. Due to their unique physical/chemical properties, they have attracted scientific interests. This study provides to a better understand the structure-dynamics-properties relationship, for different types of HBP/ kaolinite (Ka) nanocomposites.

Two different methods were employed to prepare different series of HBP/ Ka nanocomposites. One was the solution "ex situ" route, where the polymer was mixed with Ka, which was previously modified by dodecylamine (DCA). The other route was an "in situ" technique, a polymerization-based method. In this approach, the Ka layers are modified by the liquid monomer, and thus the polymerization of the polymer can occur in between the Ka sheets. The structure–property relationship of HBPs and nanocomposites were investigated by a combination of methods like differential scanning calorimetry (DSC), Fourier transform infrared spectroscopy (FTIR), small angle X-ray scattering (SAXS), transmission electron microscopy (TEM), and specific heat spectroscopy (SHS). The molecular dynamics was studied by means of broadband dielectric spectroscopy (BDS). The dielectric spectra are dominated by the conductivity contribution at higher temperatures, for all samples investigated.

As a first system, hyperbranched polyamine ester (HPAE) / Ka nanocomposites were prepared. The in situ polymerization approach led to an intercalated morphology, whereas the ex situ method resulted in an exfoliated structure, as proofed by SAXS and TEM. Due to the conductivity effects, the segmental dynamics is screened and can only be detected by SHS. A decoupling of segmental dynamics and conductivity relaxation was suggested by a comparison of their temperature dependencies. Further, this decoupling became weaker with decreasing fragility.

As a second system, hyperbranched poly(amidoamine) (HPAMAM)/ Ka nanocomposites was prepared via an in situ polymerization and an ex situ method. The latter approach showed a partly exfoliated structure of the nanocomposites, while the former method resulted in an exfoliated morphology. For the HPAMAM/ Ka-DCA nanocomposites (an ex-situ samples), the results indicated that the dc conductivity is increased by 4 orders of magnitude, with increasing concentration of

the nanofiller. For the HPAMAM/ EDA nanocomposites (an in-situ polymerization), the dc conductivity is also increased with increasing the concentration of the Ka-EDA. Further, a significant decoupling between the characteristic time for conductivity and that of segmental dynamics was observed, for all samples investigated. The decoupling phenomenon and the conductivity mechanism were discussed in detail.

In the last part of this work, hyperbranched polyester amide (Hybrane S 1200®)/ Ka-DCA was prepared via an ex situ approach. SAXS and TEM revealed that the degree of exfoliation is related to the concentration of the Ka-DCA. For the Hybrane/Ka-DCA with 10 and 20 wt-% Ka-DCA, an exfoliated structure was proved. While, a partly intercalated structure was observed, for nanocomposites with 30, 50, and 70 wt-% of the nanofiller. DSC revealed a decrease of the glass transition temperature, T_g, with increasing Ka-DCA content. The dielectric spectra of Hybrane and nanocomposites showed the α-relaxation, related to the dynamic glass transition at temperatures above T_g, and the β-relaxation originating from localized motions at temperatures below T_g or at higher frequencies than that of the α-relaxation. The relaxation processes and the dc conductivity were discussed in detail, for Hybrane and nanocomposites.

LIST OF ABBREVIATIONS AND SYMBOLS

BDS	Broadband dielectric spectroscopy
SHS	Specific heat spectroscopy
FTIR	Fourier transform infrared spectroscopy
SAXS	Small angle X-ray scattering
WAXS	Wide angle X-ray scattering
DSC	Differential scanning calorimetry
TEM	Transmission electron microscopy
NMR	Nuclear magnetic resonance
HBPs	Hyperbranched polymers
DB	Degree of branching
L_{unit}	Linear unit
D_{unit}	Dendritic unit
T_{unit}	Terminal unit
PDI	Polydispersity index
M_w, M_n	Molecular weight, number average molecular weight
HPAE	Hyperbranched polyamine ester
HPAMAM	Hyperbranched poly(amidoamine)
Hybrane	Hyperbranched polyester amide (Hybrane S 1200®)
Ka	Kaolinite
MMA	Montmorillonite
DMF	N,N-dimethyl formamide
DMSO	Dimethyl sulfoxide
MeOH	Methanol
DEA	Diethanolamine
EDA	Ethylenediamine
DCA	Dodecylamine
MA	Methyl acrylate
VFT	Vogel-Fulcher-Tammann-equation
HN	Havriliak-Negami function
CC	Cole-Cole function
CD	Cole-Davidson function

LIST OF ABBREVIATIONS AND SYMBOLS

MWS	Maxwell/Wagner/Sillars polarization
$\overline{E}$	Electric field
T	Temperature
T_g	Glass transition temperature
T_0	Vogel temperature
δ	Chemical shift
τ	Relaxation time
c_p	Specific heat capacity
E_A	Activation energy
ε^*	Complex dielectric function
ε'; ε''	Real and imaginary part of the complex dielectric function
ω	Angular frequency
$\overline{D}$	Dielectric displacement
D_0	Dielectric displacement of free space
$\overline{\mu}$	Dipole moment
$\overline{P}$	Polarization
M*	Complex modulus
M′; M′′	Real and imaginary part of the complex modulus
σ^*	Complex conductivity
σ' ; σ"	Real and imaginary part of the complex conductivity
$\mu_{mob.}$	Mobility
R_τ	Decoupling index
f_p	Relaxation rate
D_f	Fragility parameter
$\Delta\varepsilon$	Dielectric strength
ΔU	Complex differential voltage
U_R	Real part of complex differential voltage
ϕ	Phase angle of complex differential voltage
$D_{diff.}$	Diffusion coefficient

TABLE OF CONTANTS

1. INTRODUCTION 1

2. THEORETICAL BACKGROUND 6

2.1. Dendritic polymers 6

2.2. Hyperbranched polymers (HBPs) 7

2.2.1. Selected properties of HBPs 8

2.2.2. Synthesis methodologies of HBPs 10

2.3. Polymers nanocomposites 13

2.3.1 Polymer/layered silicate nanocomposites 13

2.4. Kaolinite (Ka) 15

2.4.1. Structural features of Ka 15

2.4.2. Modification of kaolinite 17

2.5. Thermal glass transition 18

2.6. Molecular dynamics of polymers 21

3. MEASUREMENT TECHNIQUES 24

3.1. Broadband dielectric spectroscopy (BDS) 24

3.1.1. The fundamentals 21

3.1.2. The origin of dielectric response of polymeric materials 26

3.1.3. Time-dependent dielectric processes 29

3.1.4. Analysis of dielectric relaxation spectra 31

3.1.5. Conductivity contribution 34

3.1.6. Maxwell Wagner Sillars (MWS) polarization 36

3.1.7. Dielectric measurements 37

3.1.8. Fitting HN-function to the experimental results 38

3.2. Specific heat spectroscopy (SHS) 39

3.3. Small angle X-ray scattering (SAXS) 42

3.4. Differential scanning calorimetry (DSC) 43

3.5. Fourier transform infrared spectroscopy (FTIR) 43

3.6. Transmission electron microscopy (TEM) 44

4. MATERIALS AND PREPARATION 45

4.1. Materials 45

4.2. Intercalation of kaolinite (Ka) 45

4.3. Characterization of the modified Ka 47

4.4. Preparation of hyperbranched polyamine ester (HPAE)/kaolinite (Ka) nanocomposite 53

4.5. Preparation of hyperbranched poly(amidoamine)(HPAMAM)/kaolinite (Ka) 55

TABLE OF CONTANTS

nanocomposites……..

4.6. Preparation of hyperbranched polyester amide (Hybrane)/kaolinite (Ka) nanocomposites…….. **57**

5. STRUCTURE-PROPERTY RELATIONSHIPS OF HPAE/KA NANOCOMPOSITES **59**

5.1. Characterization of HPAE nanocomposites…… **59**

5.2. Dielectric spectroscopy…….. **67**

6. DECOUPLING BETWEEN STRUCTURAL RELAXATION AND CONDUCTIVITY IN HPAMAM/KA NANOCOMPOSITES **77**

6.1. Ex situ prepared samples…….. **77**

6.1.1. Characterization of HPAMAM/Ka nanocomposites…….. **77**

6.1.2. Dielectric spectroscopy…….. **83**

6.2. In situ prepared samples…… **93**

6.2.1. Characterization of HPAMAM/ Ka-EDA nanocomposites…….. **93**

6.2.2. Dielectric spectroscopy…….. **98**

7. DIELECTRIC STUDY OF MOLECULAR MOBILITY IN HYBRANE/ KAOLINITE NANOCOMPOSITES **104**

7.1. Characterization of Hybrane/Ka-DCA nanocomposites…….. **104**

7.2. Dielectric spectroscopy …….. **111**

8. CONCLUSIONS **122**

9. REFERENCES **128**

10. PUBLICATIONS **137**

1. INTRODUCTION

Adjusting the architecture of macromolecules has been recognized as an important tool to obtain polymers with tailored properties. Hyperbranched polymers (HBPs) are highly branched three-dimensional macromolecules. In 1952, Flory predicted that the highly-branched polymers could be synthesized without gelation by the polycondensation of multifunctional monomers, such as a monomer containing one A functional group and two or more B functional ones capable of reacting with A (AB_x monomer $x \geq 2$) [1]. Kricheldorf and co-workers obtained branched copolymers by a one-step copolymerization of AB- and AB_2-type monomers in 1982. The terminology of ''hyperbranched polymers'' was first coined by Kim and Webster [2] in the late 1980s, referring to dendritic macromolecules with random branch-on-branch topology, prepared by a one-step polymerization. HBPs began to seriously attract the attention of scientists in the early 1990s when Swedish chemist Jöns Jacob Berzelius first reported a resin synthesized from tartaric acid (A_2B_2 type monomer) and glycerol (B_3 type monomer) [3]. Afterwards, this field was more intensely studied, especially over the recent years.

HBPs have a globular and dendritic architecture, which gives them excellent flow and processing properties such as low viscosity, high solubility, and high reactivity due to the large number of end groups, which can be further modified [4-6]. The most outstanding feature of HBPs is their degree of branching "DB" or the "branching factor," which defines the ratio of branched, terminal, and linear units in the polymer structure. According to this definition, the DB is 100% for dendrimers and lower for hyperbranched structures (50% for a statistical growth). Further, HBPs display typical polymer features, as isomerism, a molar mass distribution, and an irregular growth with a statistical distribution of the functional groups within the structure. Moreover, they can be prepared in a random one-step synthesis but with low control over structure and molar mass. It has been reported that the above-mentioned features of HBPs make them promising materials for numerous applications, such as biosensors, drug delivery systems, energy storage, coatings, etc. [7-9].

The special structure of HBPs, densely branched with a large number of end groups, can be exploited in the synthesis of nanocomposites, as they allow a better

interaction of the polymer matrix with the nanofillers [10-14]. On the one hand, their unique 3D architecture offers a large enough steric hindrance to avoid aggregation of the nanoparticles. Therefore, HBPs are good dispersants and surface modifiers for nanoparticles [15,16]. On the other hand, incorporation of nanofillers into polymers results in many interfaces with different interactions, which could be utilized to enhance the polymer properties. Moreover, properties of polymers like the transport of charge carriers are strongly related to the segmental dynamics. It has been demonstrated that nanofillers offer a possibility to tailor and optimize the dielectric and conductive properties of HBPs [17-19]. Thus, knowledge of the structure and the dynamics of HBPs and their nanocomposites are important to widen their range of potential applications.

Broadband dielectric spectroscopy (BDS) is a powerful technique to investigate the properties of polymeric systems, as proved by many investigations (see for instance [20-24]). This is mainly because of the fact that a broad dynamical range can be covered by this method. Therefore, the motional processes which take place in polymers on quite different length scales (localized fluctuations, segmental dynamics, and motions of the whole chain), can be investigated in a broad range of frequencies and temperatures. Further, BDS is applied to inspect the effect of the nanofiller on the molecular mobility of different polymeric systems. Moreover, charge transport processes depend on the morphology and micro-morphology of the system under investigation. Thus, the information on the structural state of the materials can be indirectly extracted by taking the molecular mobility and/or charge transport as a probe of the structure.

The molecular mobility of HBPs can be investigated by different techniques like BDS [25-30], quasielastic neutron scattering [31], ellipsometry [32] and specific heat spectroscopy (SHS) [33]. Principally, HBPs show an α-relaxation (segmental dynamics) related to the dynamic glass transition and secondary relaxations, resulting from localized motions. Above the thermal glass transition temperature, T_g, the α-relaxation is observed, that is a typical relaxation processes known for polymers and glass forming liquids. Whereas, below the T_g, the secondary relaxations are observed.

Specific heat spectroscopy (SHS), employing for instance differential AC-chip calorimetry, is useful to investigate the dynamic glass transition [34-37]. Here, the measurements are performed in a specific frequencies and temperatures range. To better investigate the effect of the nanofillers on the molecular mobility of HBPs, it is necessary to discuss the dynamic glass transition. Unfortunately, for the most HBPs, the segmental dynamics (α-relaxation) cannot or only hardly be observed by BDS, due to overlaying conductivity effects [38,39]. To overcome this difficulty, SHS is employed. Because of the fact that SHS detects the thermal response of a sample investigated, whereas BDS senses the fluctuations of dipoles within a sample, SHS is a fruitful technique for investigating the dynamics of HBPs and to retrieve the segmental dynamics. Thus, SHS is a complementary method to BDS to study the structure-property relationships of HBPs and nanocomposites.

Objective and challenges: The main goal of the present work is to prepare and characterize nanocomposites based on HBPs and kaolinite to attain materials of unique properties. This study provides a better understanding of the relationships between structure, morphology, and charge transport properties of nanocomposites based on HBPs. There were four main objectives in this work research:

1) Modification of kaolinite (Ka) to increase the interlayer spacing;
2) Preparation and characterization of two HBPs: hyperbranched polyamine ester (HPAE) and hyperbranched poly(amidoamine) (HPAMAM);
3) Preparation and characterization of HBP/Ka nanocomposites, with respect to the structure and thermal properties, as well as the determination of the influence of the nanofiller on the properties of the hyperbranched polymers. For comparison, a commercial hyperbranched polyester amide (Hybrane S 1200®) was also investigated;
4) Investigation of the molecular dynamics and the conductivity contribution in pure HBPs and nanocomposites. The effect of the nanofiller on the fragility of polymers and the degree of separation between the conductivity relaxation time τ_σ and the segmental dynamics τ_α (decoupling phenomenon) was studied.

To approach these aims, two different routes for the preparation of nanocomposite were employed and used to prepare different series of HBP/ Ka nanocomposites. One was the solution “ex situ” approach, where the polymer was mixed with Ka, which was previously modified by dodecylamine (DCA). The other was a “in situ” technique, a polymerization-based method. In this approach, the Ka layers are modified by the liquid monomer, and thus the polymerization of the polymer can take place in between the Ka sheets. The structure–property relationship of HBPs and nanocomposites were investigated by a combination of differential scanning calorimetry (DSC), Fourier transform infrared spectroscopy (FTIR), small angle X-ray scattering (SAXS), transmission electron microscopy (TEM), specific heat spectroscopy (SHS), and broadband dielectric spectroscopy (BDS).

Chapter 1 comprises an introduction of this study and the aim of this work. Chapter 2 provides the theoretical background and the fundamental understanding of HBPs, nanocomposites as well as the Ka nanofiller. Chapter 3 discusses the experimental methods used to characterize the polymeric systems under investigation. Further, BDS and SHS are discussed in detail. Chapter 4 briefly introduces the materials used in the study. Afterwards, the detailed description of sample preparation is given.

Chapter 5 and 6 address the main results and discussion of different polymeric systems under investigation. The structure-property relationships of HPAE/Ka nanocomposites are discussed in Chapter 5. The first part presents a characterization for all samples by combination of different methods. The results showed that an ex situ, solution based method, results in an exfoliated structure, while the in situ polymerization leads to an intercalated morphology, as proofed by SAXS and TEM. In the second part, the molecular dynamics of the pure polymer and of the nanocomposites were investigated by BDS and SHS, in detail.

The experimental findings of the second series, HPAMAM/Ka nanocomposites, were given in Chapter 6. Also, the different processing routes, resulting in different nanocomposite morphologies were addressed. The charge carrier transport was studied in a wide frequency and temperature range by means of the BDS. The

obtained results indicated that the dc conductivity increases with increasing concentration of the nanofiller. Further, a significant separation between the conductivity relaxation time τ_σ and that of the segmental dynamics τ_α was observed. In other words, a strong decoupling between charge mobility and segmental mobility was detected. The decoupling phenomenon and the conductivity mechanism were discussed in detail.

Chapter 7 represents the results of the Hybrane/ Ka-DCA nanocomposites. The different concentrations were prepared to study the confinement effect in nanocomposites.

Lastly, the conclusions and a brief outlook were given in Chapter 8.

2. THEORETICAL BACKGROUND

2.1. Dendritic polymers

The origin of the word dendritic drives from the Greek word, dendro, (meaning tree). Accordingly, dendritic polymers are characterized by densely branched structures and a large number of terminal groups - a tree-like globular structure [40-42]. The dendritic architecture is recognized as a major class of macromolecular architecture [43,44], that have been widely studied and industrially used. Till now, eight subclasses of dendritic polymers have been developed (Figure 2.1): (A) dendrimers, (B) dendrimer-like star macromolecules (DendriMacro), (C) dendronized polymers, (D) linear-dendritic hybrids, (E) hyperbranched polymers (HBP), (F) hyperbranched polymer-like star macromolecules (HyperMacro), (G) hyperbranched polymer-grafted linear macromolecules and (H) hyperbranched polymer brushes. The first four subclasses exhibit uniform structures and have a degree of branching (DB) equals 1.0, while the latter four display an irregular branched structure with a lower DB [45]. Linear polymers connected with side dendron are called as dendronized polymers.

HBPs and Dendrimers have been extensively studied as the representative irregular and regular dendritic polymers, respectively. Even though HBPs have irregular structures with randomly branched topology, they still have properties similar to dendrimers, such as high solubility, low viscosity, and a large number of functional groups. Thus, HBPs retain the main features of dendritic macromolecules and show properties intermediate to those of dendritic and linear polymers [39,46]. HBPs have the additional advantage of a cost-effective synthesis, as compared to dendrimers, because of their one-pot synthetic approach and the lack of need for tedious purification procedures [47,48].

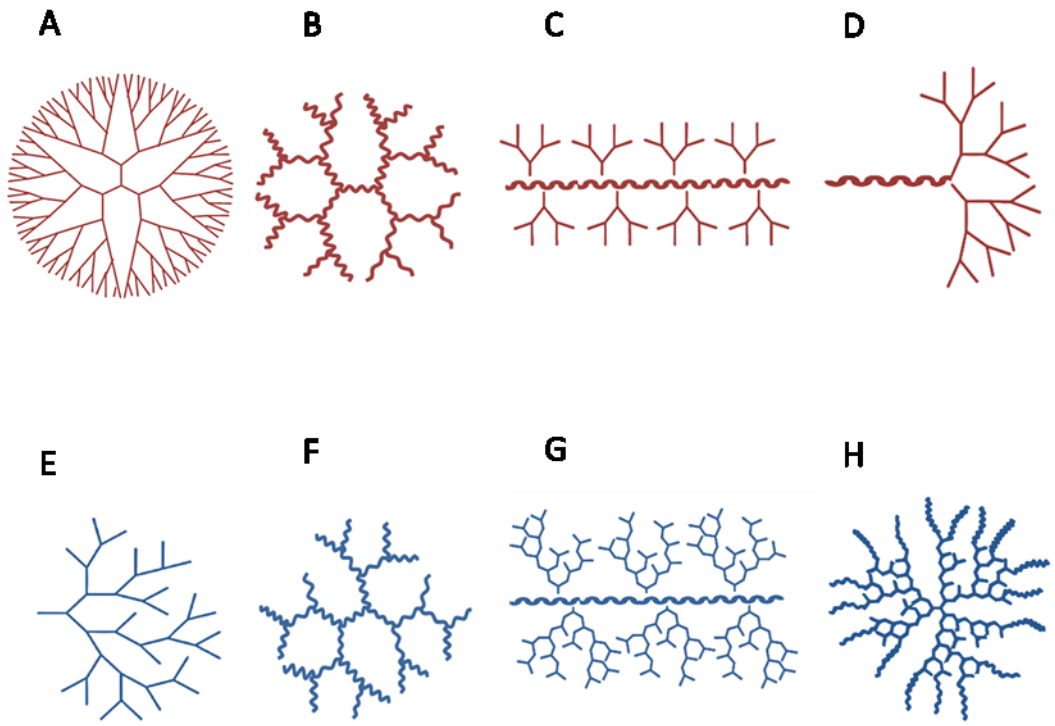

Figure 2.1: Dendritic polymers with different structures. (A) Dendrimer, (B) DendriMacro, (C) dendronized polymer, (D) linear-dendritic hybrid, (E) hyperbranched polymer HBP, (F) HyperMacro. (G) HBP-grafted linear polymer and H) multiarm star polymer or hyperbranched polymer brush. The figure was adapted from Ref. [4].

2.2. Hyperbranched polymers (HBPs)

HBPs are macromolecules that are characterized by a highly branched structure and multiplicity of reactive end groups. They belong to the family of dendritic polymers [38-40], but are less perfectly branched than the monodisperse dendrimers. HBPs have a molecular size generally ranging from several nanometers to dozens of nanometers [49,50].

During the last three decades, HBPs have received a great attention due to their unique physical/chemical properties as well as the potential applications [6,38,51]. A lot of potential applications of HBPs have been reported, in a large variety of fields, such as rheological modifiers [52], membranes [53], coatings [54], super molecular chemistry [55], drug delivery [56], and nanomaterials [57].

2.2.1. Selected properties of HBPs

***High activity*:** The globular structure of HBPs, densely branched with a large number of end groups, differs from the structure of linear polymers. Hence, the properties differ as well. The functional end groups of HBPs can be synthesized with a vast number of active groups, for instance the hydroxyl groups, then their activity will be higher. Thus, HBPs can be exploited to introduce macromolecular materials with different properties. This can be understood by taking into account that the melt behavior of HBPs, besides other properties, has been observed to be greatly affected by type of the end groups. Whereas, an increase in the polarity of the end groups could increase the dynamic viscosity [40]. For example, three different aliphatic hyperbranched polyesters having three different structures of end groups, (propionate, benzoate, and hydroxyl end groups), were investigated [58]. The result showed that the complex dynamic viscosity as a function of temperature increased by several orders of magnitude, for the sample of hydroxyl end groups. In this regard, it is thought that with adjusting the type and the number of the end groups of HBPs, it is possible to make them are disciplined in different applications.

***Low viscosity*:** HBPs have a close relationship with polymer properties e.g., free volume, chain entanglement, glass transition temperature (T_g), degree of crystallization, etc. [4]. As the viscosity is related to the intermolecular interactions [59], the highly branched structure of HBPs results in less intermolecular entanglement, which gives them a low viscosity and a good solubility. In general, they have significantly lower viscosities than linear polymers of a similar molecular weight. Fréchet introduced [60] a comparison between linear polymers, HBPs and dendrimers with respect to the intrinsic viscosities, as a function of the molecular weight (see Figure 2.2). The result clearly showed the differences for molecular weight dependence of the intrinsic viscosity induced by variations in the architecture. In practice, it is observed that the intrinsic viscosity of HBP is lower than that of the linear analog. Another feature of HBPs is the relationship between molecular weight and melt viscosity. For linear polymers, the increase in melt viscosity with molecular weight is linear with a transition to a 3.4 power law when the molecular weight increases beyond a critical value [61]. This transition around the critical molecular weight is sharp and is supposed to be associated with the onset

of entanglement. For HBPs, having less intermolecular entanglements, the increase in melt viscosity shows a different behavior, whereas the curve is less pronounced and maintains constant at higher molecular weights [40,62] (Figure 2.3).

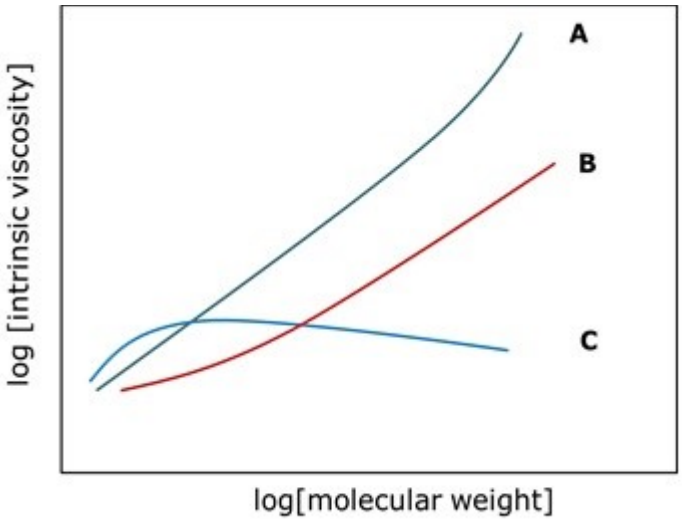

Figure 2.2: Scheme for the change of intrinsic viscosity with molecular weight of (A) linear polymers, (B) hyperbranched polymers, and (C) dendrimers.

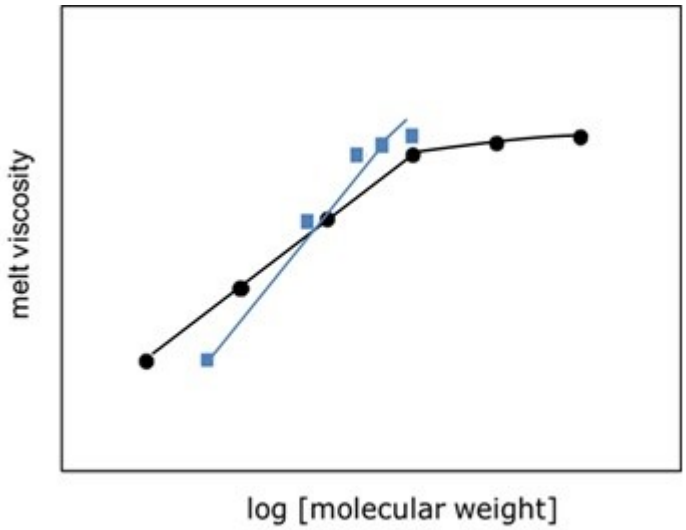

Figure 2.3: Melt viscosity versus molecular weight for hydroxy-functional hyperbranched aliphatic polyesters (circles), compared to linear polystyrene standards (squares). The figure was adapted from Ref. [40].

***High solubility*:** The large number of end groups strongly affects the interactions between the HBPs and its neighboring molecules, thus affecting the solubility. HBPs have high solubility in comparison to linear polymers of a similar molar mass. For example, it has been reported that [63], hyperbranched polyphenylenes exhibited good solubility in different solvents, compared to linear polyphenylenes, which have poor solubility. Taking these outstanding advantages into account, in addition to a special hyperbranched structure, HBPs are some of the most promising materials for both academia and industry.

2.2.2. Synthesis methodologies of HBPs

The synthesis of HBPs can often be simplified compared to that of dendrimers as it does not require the use of protection/deprotection steps. Four methodologies have been developed to prepare HBPs: (1) polycondensation of symmetric monomer pairs of A_2 and B_3 monomers under the rule of Flory's equal reactivity [64], (2) coupling-monomer methodology, CMM, as the principle of nonequal reactivity, (3) polycondensation of AB_x -type monomers, ($x \geq 2$) and (4) self-condensing chain-growth polymerization of AB^*-type monomers. The first two methodologies can also be considered as "double -monomer" strategy, and the last two can be ranged as "single-monomer" strategy [4,65].

Polycondensation of AB_x Monomers: Majority of HBPs are probably produced by the step-growth polycondensation of the AB_x -type monomers, ($x \geq 2$) [1,66-68]. The obtained HBP will have a highly-branched structure and a large number of end groups, which contains dendritic, linear and terminal units in addition to one focal group (A group), see Figure 2.4. If both B groups can react with the A group, it generates one dendritic unit. If only one B group of the AB_2 monomer is reacted, it forms one linear segment. If none of the B groups is reacted, this unit becomes a terminal one.

One of the most important aspects of HBPs characterization is the determination of its structure, namely the evaluation of the concentration of terminal (T_u), linear (L_u) and dendritic (D_u) units. These values will allow calculating the degree of

branching (DB). The DB is considered to be a main structural feature affecting the properties. Consequently, the DB for a linear polymer is zero (DB= 0), while a perfect dendrimer has a DB of 1.0. According to Fréchet [60], for polycondensation of an AB_2 type monomer, the DB can be calculated to

$$\mathrm{DB} = \left(\frac{D_u + T_u}{D_u + L_u + T_u} \right). \tag{2.1}$$

As a HBP with a high degree of polymerization, the number of T_u is approximately equal to that of D_u. So, Eq. (2.1) is simplified as [69]

$$\mathrm{DB} = \left(\frac{2D_u}{2D_u + L_u} \right). \tag{2.2}$$

Most often, the fraction of D_u, L_u and T_u repeating units are determined by NMR spectroscopy.

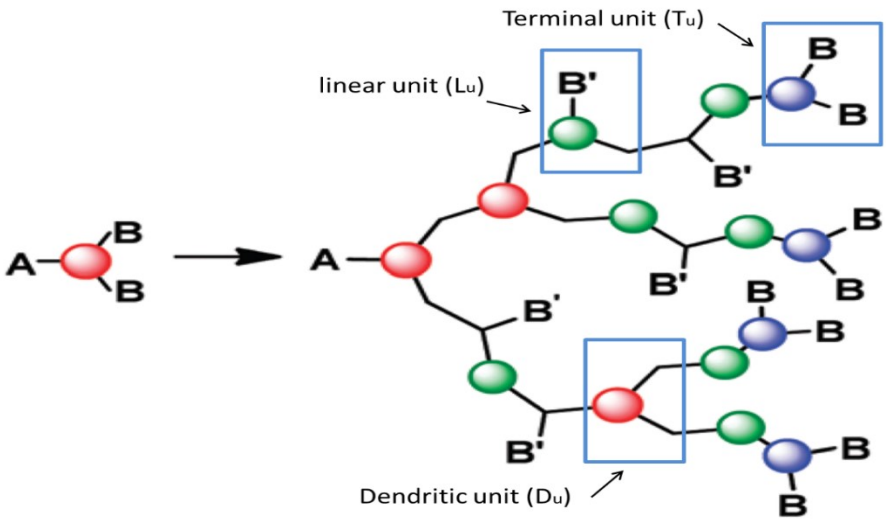

Figure 2.4: HBP formed from an AB_2 monomer exhibiting terminal (T_u), linear (L_u) and dendritic (D_u) sub-units as well as one unreacted [50].

Coupling-monomer methodology (CMM): More than 10 families of HBPs, including hyperbranched polyamine ester (HPAE) and hyperbranched

poly(amidoamine) (HPAMAM), have been prepared via the CMM method [70-72]. The CMM approach was invented by Gao and Yan [73]. Its theoretical base is a non-equal reactivity of functional groups in specific monomer pairs like AA′ and B′B_2. According to the reactivity of a monomer pair of AA′ and/or B′B_2, the CMM methodology degenerates into four subgroups; (1) the "A_2 + B_3" polymerization if A is equal to A′ and B is identical to B′, (2) the "AA′ + B_3" polymerization if A′ has a higher reactivity than A, (3) the "A_2 + B′B_2" polymerization if B′ is more active than B and (4) CMM affords "A_2 + B′B_2" and "A_2 + CB_2" polymerization systems when both A and B groups are different from A′ and B′ groups, CMM means an "AB + C_2" or "AB + CD_2" polymerization. The AB_2-type intermediate would mostly form in the initial stage of polymerization through all designed polymerization systems; further reaction would produce HBPs without gelation [45]. The basic principle of CMM is shown in Figure 2.5. Finally, CMM can be used to extend the availability and accessibility of HBPs with various new end groups, architectures, and properties, without the risk of cross-linking.

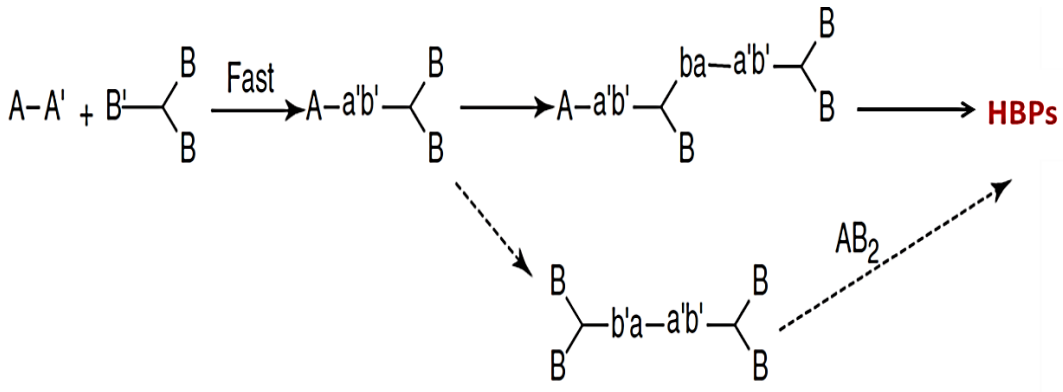

Figure 2.5: Schematic illustration for the preparation of HBPs by couple-monomer methodology (CMM) using "A′A + B′B2" approach as a typical example for the basic principle description of the CMM method [4].

Synthesis of hyperbranched polyamine ester (HPAE): The synthesis technique used to prepare (HPAE) belongs to "AB + CD_2" polymerization category. HPAE is prepared by polymerization of methyl acrylate MA (AB) and diethanolamine DEA (CD_n, n ≥ 2) monomer, which containing one secondary amino group and

multihydroxy groups. At mild temperatures, the vinyl group (B) reacts with the amino group (C) to form an AD_n intermediate, containing a methyloxy carbonyl ($CH_3OC=O$) group and n hydroxy groups. The HPAE can be prepared by self-condensation of the AD_n intermediate, under specified conditions (see section 4.4).

***Synthesis of hyperbranched poly(amidoamine) (HPMAM)**:* Methyl acrylate MA (AB-type monomer) react with ethylenediamine EDA (C_n monomers), according to "AB + C_2" polymerization system, to yield aliphatic HPAMAM. At room temperature, the AC_n or AC_{n-1} intermediate can be formed. The HPAMAM could then be obtained by self-condensation of the intermediates at higher temperatures under vacuum (see section 4.5).

2.3. Polymers nanocomposites

Polymer nanocomposites are a unique and vitalize class of nanomaterials. They can be produced by embedding fillers, having at least one dimension in the nanometer range, into the polymer. In recent years, they have attracted massive attention due to their potential applications in biomedical, microfabrication, fuel cell, capacitor, high flux gas transport, fire-resistance applications, etc [74]. Moreover, an improvement in mechanical properties such as tensile strength, tensile modulus, and young modulus of polymer nanocomposites is the most common feature exploiting in the engineering applications [75-79].

2.3.1. Polymer/layered silicate nanocomposites

Among all the potential nanocomposite precursors, those based on layered silicates have been most widely investigated. They display unique properties such as, improved thermal resistance, enhanced mechanical strength, reduced gas permeability, etc., which could be exploited in multiple potential applications [80-82]. The reasons behind property improvements stem from nanometer sizes, low filler loadings, and large surface areas [83 , 84]. The nanometer sizes allow tremendous interfacial contacts between the polymer and nanofiller that can significantly affect the charge transport properties at high operational fields [85,86].

The low nanofiller loadings can also support the formation of nanocomposite without change some of the intrinsic polymeric properties. Finally, the existence of a large interfacial area results in a huge interaction of polymer matrices with fillers. It is worth mentioning that the degree of dispersion of the nanoparticles is an important point in developing such nanocomposites. Thus, a homogeneous distribution of the layered silicates within the polymer matrix is required, to avoid the formation of phase separated composites or aggregates. If a phase separated composite is obtained, the final properties stay in the same range as traditional microcomposites.

Several strategies have been considered to prepare polymer-layered silicate nanocomposites. They include three main processes [87]; (1) *in situ polymerization*: in this approach, the layered silicate is modified by the liquid monomer, and thus polymer formation can occur in between the intercalated sheets, (2) *melt intercalation*: the layered silicate is mixed with the polymer matrix in the molten state. In this method, no solvent is required, and (3) *solution based method*: the nanofiller is exfoliated into single layers using the same solvent, in which polymer is soluble then mixed with the polymer solution.

The resulting nanocomposites can either be referred to as “exfoliated” if the regularity of layered silicate disappeared and their sheets are completely dispersed in the matrix and, or as “intercalated” if the polymer is present between the silicate sheets, but the order of the layered structure is maintained (Figure 2.6) [88]. Nevertheless, in experiments, the mixed structure from exfoliated and intercalated nanocomposites could be resulted from applying a solution based method or during an in situ polymerization. Further, the microcomposites could be formed, if the polymer is unable to intercalate within the silicate layers. And thus, the layers stacked together within the polymer matrix. It is worth mentioning that the method of the preparation of the nanostructures, the type of the nanofiller, and the treatment of its surface have a significant influence in preparing exfoliated or intercalated nanocomposites [89-91].

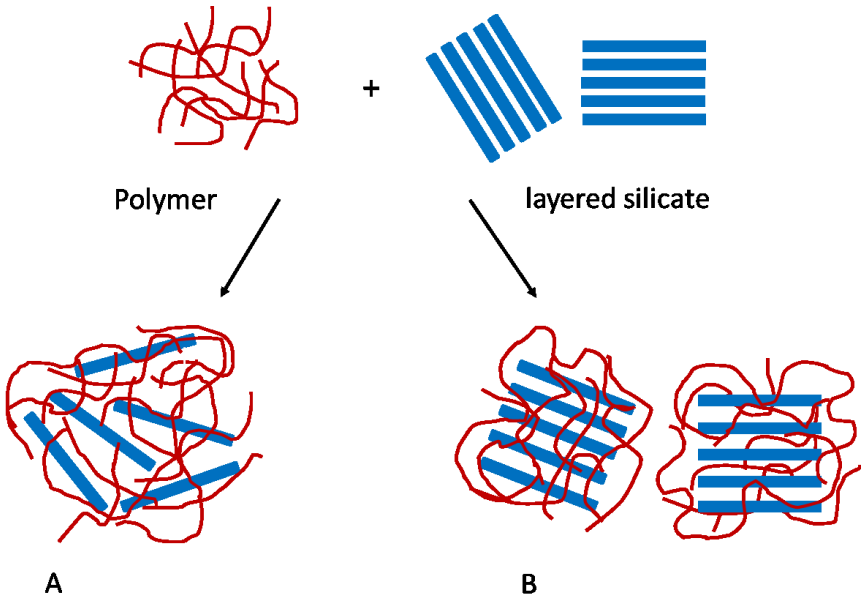

Figure 2.6: Scheme of different types of nanocomposite arising from the interaction of layered silicates and polymers: (A) exfoliated nanocomposite and (B) intercalated nanocomposite

2.4. Kaolinite (Ka)

2.4.1. Structural features of Ka

Layered silicates are minerals that assemble regularly with the unit crystalline layer, usually at the nanoscale. They are easily available and have a low cost. Corresponding minerals are montmorillonite (MMT), kaolinite, nacrite, dickite, sepiolite, etc. Kaolinite (Ka) is the most common of the kaolin-group, is also one the most abundant layered silicate minerals [92,93], which is used in various classical applications, e.g. pottery, ceramics, paper coating, paints, soaps, etc. [94].

The Ka belongs to a dioctahedral 1:1 layer structure of clay minerals, with the general composition of $[Al_2Si_2O_5(OH)_4]$. Ka, a layered silicate mineral, consists of nanometer thick layers. The individual silicate layer is composed of one tetrahedral sheet of silica (SiO_4) and one octahedral sheet of alumina (AlO_6). The silica and alumina sheets are linked to each other covalently in layers. Adjacent layers are linked to one another with hydrogen bonds, involving oxygen atoms situated in the silica sheet and hydroxyl groups in the alumina sheet (Al-O-H…….O-Si) (Figure 2.7). There are two types of hydroxyl groups in the structure. Inner-surface hydroxyls existed on the interlayer surfaces and inner hydroxyls located inside the layers,

between the two different sheets. The distance between two opposite layers, the interlayer spacing, is d= 0.71 nm. The individual layers are further linked by dipole–dipole interactions and van der Waals forces [95,96]. In addition, the cation exchange capacity of Ka is low ((3-15) meq/100g) [97].

As above-mentioned characteristics of Ka, the Ka layers are strongly held together by hydrogen bonding and by dipolar interaction. Therefore, intercalation, that is, the reversible insertion of a molecule or ion into layered compounds, is difficult in the case of Ka. Consequently, the Ka is not an optimal nanofiller for nanocomposites. To overcome these limitations, the modification of Ka is necessary for increasing the interlayer distance. Further, the intercalation of any compound, be it organic or inorganic, between the layers of Ka causes a breaking up the hydrogen bonding between the layers. Therefore, guest molecules acquire the ability to arrive at the reactive aluminol groups. These groups could be reacted with organic molecules; thus, the modified Ka is possible to be used in nanocomposites [98].

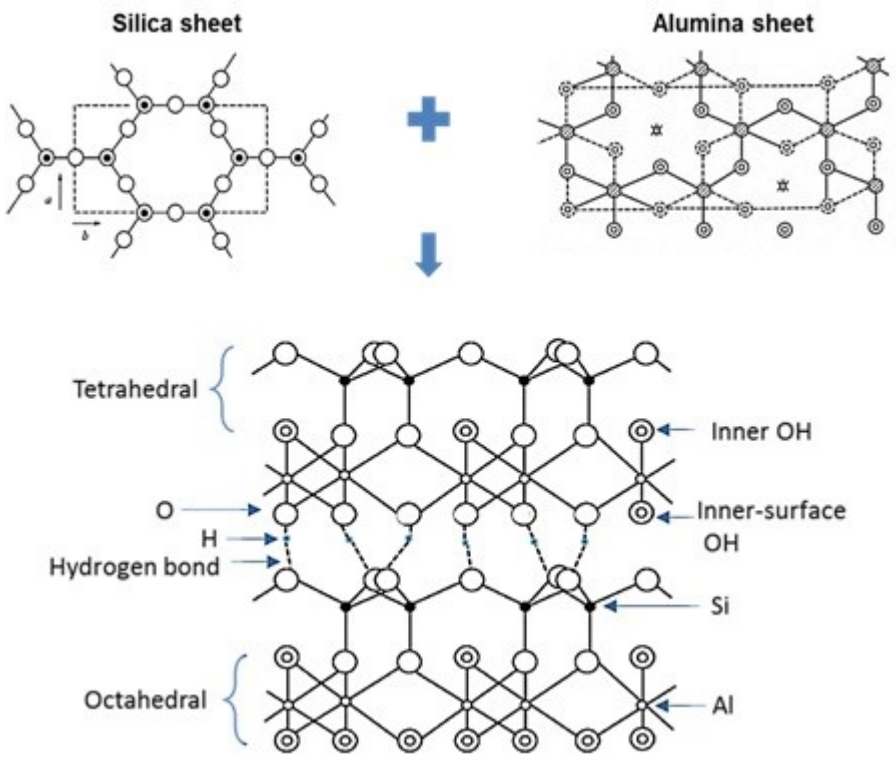

Figure 2.7: Sketch of kaolinite. Figure was adapted from Ref. [96].

2.4.2. Modification of kaolinite

Kaolinite (Ka) is generally known as a non-expandable clay mineral yields. However, in recent years, the progress in the intercalation of Ka has increased significantly [97,99]. One might expect that Ka–polymer nanocomposites will be developed, which could be utilized in various applications.

Modification of Ka, by intercalation or grafting of small molecules, has been reported for a different number of organic species, e.g. hydrazine [100], acetamide [101], ionic liquids [102], and urea [103]. The most common compounds used for direct intercalation are dimethyl sulfoxide (DMSO) [104] and N-methylformamide (NMF) [105-107]. Many other molecules can be inserted between the Ka interlayer spacing by indirect intercalation, use of pre-intercalated precursor via a displacement method. Once the Ka layers are partially separated, the intercalated molecules may be substituted by new chemical groups. The organics and polymers, which cannot directly enter into the layers, may be intercalated through substitution reactions. It has been reported [108] that the Ka was modified by N-methyl formamide then methanol was intercalated into the structure of Ka. And further, the methanol was replaced with alkylamines with different numbers of carbon atoms in the alkyl chain. Thus, the interlayer spacing of Ka increased from 0.72 up to 4.2 nm, just to mention one example besides many others. Several types of polymer/Ka nanocomposite were prepared by using different procedures [109]. For instance, polyvinylchloride/ Ka-DMSO nanocomposites were prepared via solution approach using tetrahydrofuran (THF) as a solvent. The resulting nanocomposite showed an improvement of the thermal stability [110]. Also, the melt intercalation approach was employed to produce polyethylene glycol (PEG)/ Ka nanocomposites [111,112]. In situ polymerization approach, that is, intercalation of the monomers followed by polymerization, was used for the preparation of a few more intercalated nanocomposites, such as Nylon6 [113] and poly(methacrylamide) [114]. For this study, the modification of Ka and the intercalation processes for nanoparticles will be described, in detail, in Chapter 4.

2.5. Thermal glass transition

The glass–liquid transition or glass transition, for short, is a transition from the equilibrium liquid state to the non-equilibrium solid-like glassy state (without crystallization) [115]. If a glass-forming material cools down with a constant rate, a typical behavior is observed for the temperature dependence of characteristic thermodynamic quantities, such as specific volume and enthalpy. In parallel, step-like changes in the materials properties such as the specific heat c_p are observed. This phenomenon is called thermal glass transition T_g. In general, the glass transition temperature can be obtained as the temperature at the intersection of extrapolated tangent lines from the glassy state (below T_g) and the supercooled melt state (above T_g) (see Figure 2.8A). During this transition, the slope of the temperature dependence of characteristic thermodynamic quantities changes as shown in Figure 2.8A. Further, T_g depends on the cooling rate. For fast cooling rate, it is higher than that in the case of slower cooling rate ($T_{g1} > T_{g2}$) (see Figure 2.8A). Moreover, the T_g takes place over a given temperature range called the glass transition region (see Figure 2.8B) [116].

It is worth mentioning that the glass transition is not a true thermodynamic phase transition because the behavior as illustrated in Figure 2.8A does not contain discontinuous changes in any physical property, such as specific volume and enthalpy [117]. Rather, it is a kinetic phenomenon. Practically, the thermal glass transition, T_g, can be determined by different methods such as differential scanning calorimetry (DSC) (see section 3.3), where step-like changes in material properties is detected, as a function of temperature.

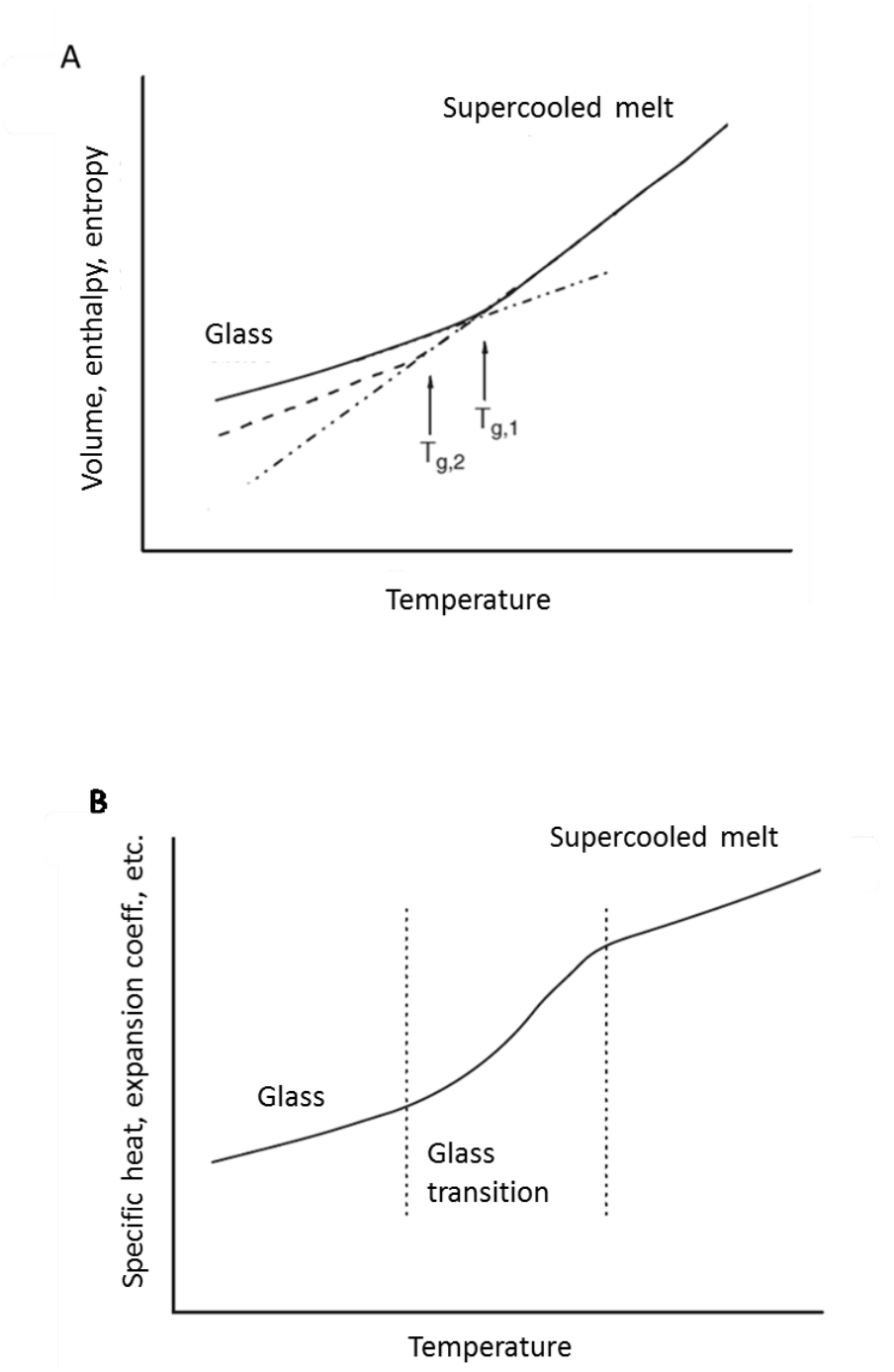

Figure 2.8: Scheme of the thermal glass transition. (A) Temperature dependence of thermodynamic quantities such as volume, enthalpy, or entropy in the temperature range of the glass transition. $T_{g,1}$ and $T_{g,2}$ indicate the glass transition temperatures for two cooling rates $T_1 > T_2$. (B) Temperature dependence of the material properties at the glass transition. The figure was adapted from Ref. [115].

Polymeric materials are rather complex systems. For example, the bulk a polymeric system can behave as an elastic solid, as a rubbery (viscoelastic) material which is highly deformable or as a melt in dependence on temperature. This can be recognized from the temperature dependence the shear modulus G (Figure 2.9). It is observed that the G drops down by three orders of magnitude when an amorphous polymer is heated from the glassy state to the viscous state. The glass transition temperature T_g can also be obtained from this step-like change, which approximately corresponds for low-measuring frequencies to the value that can be measured by calorimetry. The rubbery (viscoelastic) plateau at higher temperature is due to chain entanglements that are formed for molecular weights higher than the value of a critical molecular weight M_C. With further increasing temperature, the chains have a further more increased mobility, and the systems behave like an ordinary liquid, i.e. the shear modulus is approximately zero.

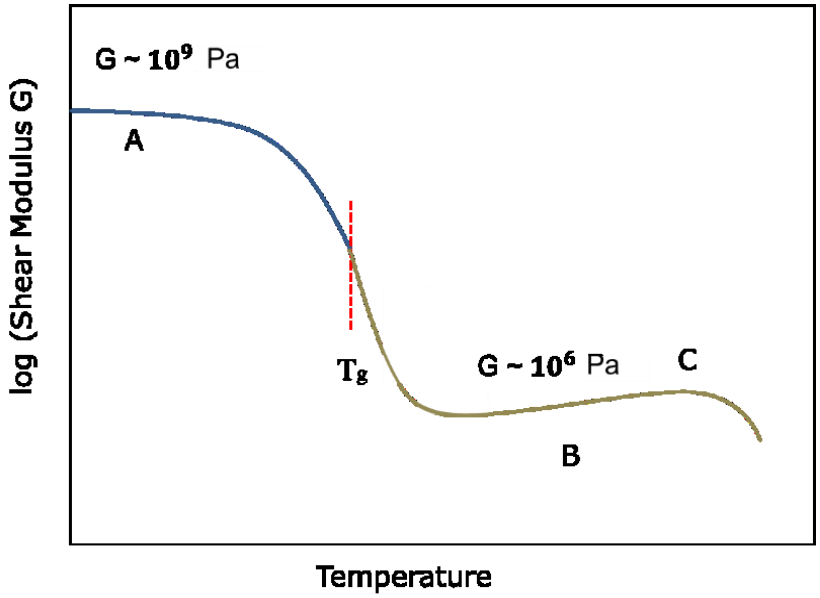

Figure 2.9: Typical temperature dependence of the shear modulus G of an amorphous polymer (A) Glassy region, (B) Viscoelastic region, and (C) Melt region. The figure was adapted from Ref. [24].

2.6. Molecular dynamics of polymers

Relaxation processes are related to the molecular mobility within polymers and other glass-forming substances. The fluctuations can be assigned to localized (secondary relaxation processes), segmental motions as well as collective motions involving the whole macromolecular. Each relaxation process has specific features in its frequency and temperature dependence of the real and imaginary part of the complex dielectric function (see section 3.1).

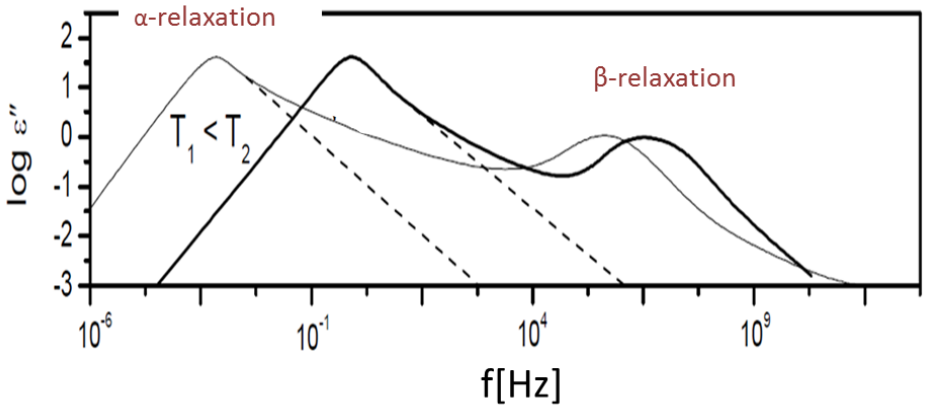

Figure 2.10: Schematic shows the molecular dynamics of amorphous polymers around the glass transition. The dielectric loss versus frequency for two temperatures T_1 and T_2. Two relaxation processes, the α-relaxation (dynamic glass transition) and the β-relaxation, are indicated. The figure was adapted from Ref. [24].

Figure 2.10 gives an overview about the relaxation processes in amorphous polymers around the glass transition using the dielectric loss as example. The most prominent process is the so called is α-relaxation which also called structural relaxation or the dynamic glass transition. It is observed at temperatures above T_g. In the viscoelastic region, a large number of amorphous polymer segments move simultaneously in a cooperative segmental motion. Further, macromolecules are affected by the local environment. Therefore, the α-relaxation involves both intramolecular and intermolecular interactions. It can be observed as an asymmetric broad peak, for instance in the dielectric loss over a range of 2 to 6 frequency decades. With increasing temperature, the process is shifted to higher frequencies. The

frequency of maximal loss related to α-relaxation is defined as the α-relaxation rate $f_{p,\alpha}$ or α-relaxation time $\tau_{p,\alpha}=1/(2\pi f_{p,\alpha})$.

Further, most amorphous polymers show a β-relaxation process, which can be assigned to rotational fluctuations of side groups or other intramolecular fluctuations in the polymer. This type of local dynamics is active even when the polymer is in the glassy state, that is, when the segmental motions are frozen [118,119]. The β-relaxation is characterized as a broad peak (with half widths of 4-6 decades).

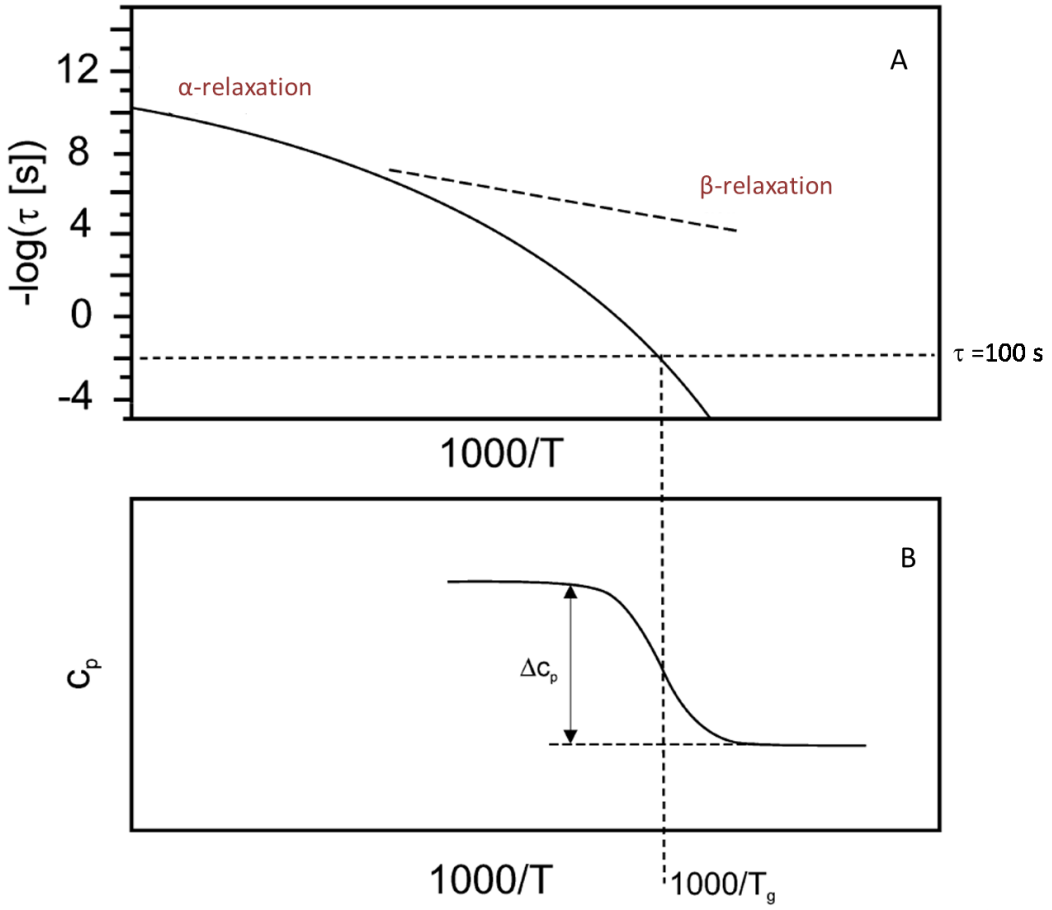

Figure 2.11 (A) Schematic indicates of the temperature dependence of the relaxation rate for the α- and the β- relaxations. The former can be described by the VFT function (Eq. 2.3) and the latter follows the Arrhenius function (Eq. 2.3). (B) Thermal glass transition where the specific heat capacity is plotted versus inverse temperature. The figure was adapted from Ref. [24].

A typical relaxation rate versus temperature for the α-and the β- relaxations was sketched in Figure 2.11A. The temperature dependence of the relaxation rate of the α-relaxation is curved and can be described by the Vogel-Fulcher-Tammann (VFT) equation [120-122].

$$log f_{p,\alpha} = log f_{\infty} - \left(\frac{A}{T - T_0}\right) = log f_{\infty} - \left(\frac{DT_0}{T - T_0}\right) \quad (2.3)$$

where f_{∞} and A are fitting parameters and T_0 is called ideal glass transition or Vogel temperature, which is found empirically to be 30-70 K below the thermal T_g. Further, extrapolating this dependence to lower frequency is in agreement with the data characterizing thermal glass transition with specific heat capacity in Figure 2.11B

Depending on how much the dependence of the relaxation rate versus the temperature for the α- relaxations deviates from the Arrhenius-type behavior, glassy materials are classified as fragile or strong. From Eq.2.3, the fragility parameter is $D= A/T_0$ (the fragility strength), can be estimated. It provides among others a useful quantity to classify glass forming systems [123-124]. Materials are called "fragile" if their f_p dependence deviates strongly from an Arrhenius-type behavior and "strong" if f_p is close to the latter.

The temperature dependence of the relaxation rate, $f_{p,\beta}$, of the β-relaxation follows an Arrhenius-type equation

$$f_{p,\beta} = f_{\infty} \exp\left(-\frac{E_A}{k_B T}\right) \quad (2.4)$$

where k_B is the Boltzmann constant, E_A the activation energy and f_{∞} the pre-exponential factor. The activation energy (the barrier height) represents the potential barrier between two possible states (e.g., two different positions of a polar group relatively to the main chain).

3. MEASUREMENT TECHNIQUES

Chapter 3 is organized as follows: The major techniques used in this work, broadband dielectric spectroscopy (BDS) and specific heat spectroscopy (SHS), are introduced in detail. While other techniques used for the characterization and morphologies are also mentioned.

3.1. Broadband dielectric spectroscopy

Broadband dielectric spectroscopy (BDS) studies the interaction of electromagnetic radiation with matter in a wide range of frequencies (from 10^{-3} to 10^{12} Hz) and temperatures. It was proved to be one of the most powerful and versatile techniques to investigate the dynamics of polymers in different states (i.e., solid or liquid state). A detailed description of dielectric theories is introduced by Kremer and Schönhals [24]. The discussion in the following section is based on this reference.

3.1.1. The fundamentals

BDS is based on Maxwell equations [125,126], which give the fundamental relationship between the electric field E, the dielectric displacement D, the magnetic field H, the density of charges ρ, the current density j, and the magnetic induction B. It is important to note that all components of the Maxwell equations are vectors and thus the dielectric properties are in general tensors. This becomes important for anisotropic systems like crystalline materials or liquid crystalline. For the sake of simplicity, the vectorial and tonsorial character of the dielectric properties is neglected in this work.

In the linear case, this means for small electric field strengths, the dielectric displacement can be represented by

$$D = \varepsilon^* \varepsilon_0 E. \qquad (3.1)$$

where ε_0 is the dielectric permittivity of vacuum (ε_0= 8.854 10^{-12} As V^{-1} m^{-1}) and ε^* is the complex dielectric function.

In general, differences in the time dependences of the outer electric field, E(t), and the resulting dielectric displacement D(t) are due to the time-dependent processes

within a material. For instance, in the case of a periodic electric field of $E^*(\omega) = E_0 \exp(-i\omega t)$ (ω- angular frequency, ω =2πf, f-frequency of applied electric field, i =√-1- imaginary unit) in the stationary state, the difference in the time dependence of E(t) and D(t) is a phase shift, which can be described by the complex dielectric function

$$\varepsilon^*(\omega) = \varepsilon'(\omega) - i\varepsilon''(\omega) \tag{3.2}$$

where $\varepsilon'(\omega)$ and $\varepsilon''(\omega)$ are real and imaginary part of the complex dielectric function, respectively. The former is related to the energy stored reversible during one period and the latter represents the energy loss during one cycle.

The polarization P describes the dielectric displacement which originates from the response of a material to an external field only. Whereas, Eq. 3. 1 contains contribution to the dielectric displacement of the free space D_0. Thus, the polarization of dielectric can be defined as

$$P = D - D_0 = (\varepsilon^* - 1)\varepsilon_0 E = \chi^* \varepsilon_0 E \tag{3.3}$$

where $\chi^* = (\varepsilon^* - 1)$ is the dielectric susceptibility of the material under external field.

Ohm's law gives the relationship between the electric field and the current density j. It is read as

$$j = \sigma^*(\omega)\, E \tag{3.4}$$

where $\sigma^*(\omega) = \sigma'(\omega) + i\,\sigma''(\omega)$ is the complex conductivity ($\sigma'(\omega)$and $\sigma''(\omega)$are the corresponding real and imaginary parts, respectively). In the case of absent magnetic fields, the time derivatives of the dielectric displacement and the current density are equivalent. Thus, the analogous between Eq. 3.4 and Eq.3.1 holds

$$\sigma^*(\omega) = i\omega\varepsilon_o\varepsilon^*(\omega) \tag{3.5}$$

The dielectric properties of a material can be expressed by $\varepsilon^*(\omega)$ or $\sigma^*(\omega)$. Further, the complex modulus can also be used. It is related to $\varepsilon^*(\omega)$ as follows:

$$M^*(\omega) = \frac{1}{\varepsilon^*(\omega)} = M'(\omega) + i\,M''(\omega), \tag{3.6}$$

$$M' = \frac{\varepsilon'}{\varepsilon'^2 + \varepsilon''^2}\,; \qquad M'' = \frac{\varepsilon''}{\varepsilon'^2 + \varepsilon''^2}$$

where $M'(\omega)$ and $M''(\omega)$ are real imaginary part of the complex electric modulus, respectively.

3.1.2. The origin of dielectric response of polymeric materials

The polarization of a dielectric submitted to an external electric field can take place by several different mechanisms. On a molecular level, polarization P as a macroscopic property originates from a dipole moments p_i. Hence, for molecule and/or particles in volume V, the polarization can be given by

$$P = \frac{1}{V}\sum p_i \tag{3.7}$$

where i counts all dipole moments in the system. In general, a dipole moment is created if electric centers of gravity of positive and negative charges do not overlap. A dipole moment is obtained if a positive and a negative charge q are separated by a distance d. Then the dipole moment is $\mu = q*d$ [24]. Depending on the frequency range, polarization involves several mechanisms:

a) Induced dipole polarization: The dipole moment is induced by the outer electric field itself which deforms a neutral distribution of charges [127]. One example of induced polarization is the electronic polarization. Under the influence of an external electric field, the negative electron cloud of an atom (molecule) is shifted with respect to the positive nucleus. Another example is the atomic polarization, which occurs when adjacent positive and negative ions "stretch" under the applied electric field. These effects can be summarized by an induced polarization P_∞.
b) Space charge polarization (interfacial or hopping polarization): This takes place mainly in amorphous, or polycrystalline solids materials, or in heterogeneous

materials. Charge carriers (electrons, holes, or ions), which could be emitted from electrical electrodes, may be trapped at the interfaces or may be impeded to be discharged or replaced at the electrical electrodes. In this case, space charges will be generated. These space charges, in turn, change the field distribution.

c) Permanent dipole moments: Before applying an electrical field, the permanent dipoles of a molecule are randomly distributed. If an electrical field is applied, these dipoles get oriented in the direction of the electrical field. This is further called an orientation polarization.

It is known that electronic polarization takes place on a time scale of 10^{-12} s, which is extremely fast, because of the low mass of the electron. Atomic polarization has a comparable time scale. Thus both electronic and atomic polarization are considered instantaneous in dielectric spectroscopy. Therefore, the main contribution to polarization phenomena observed in polymers, arises from the rotational mobility of permanent dipole moments. Further, because molecular dipoles are attached to molecules and thus their movement can be hindered by the surrounding, the response of orientation polarization is retarded. When an alternating electric field is applied, at low frequencies, the molecular dipoles fluctuate with the same frequency (or time constant) of applied field. However, at higher frequencies, dipoles cannot follow the field any more. Between these two phenomena, the dielectric relaxation process takes place with a characteristic time constant called relaxation time τ.

For molecules with a permanent dipole moment μ and containing only one kind of dipoles, Eq. 3.7 can be simplified to

$$P = \frac{1}{V}\sum \mu_i + P_\infty = \frac{N}{V}\langle\mu\rangle + P_\infty \tag{3.8}$$

where N denotes the whole number of dipoles in a volume V, and $\langle\mu\rangle$ the mean dipole moment. When the dipoles are assumed to be not interacting with each other (isolated dipoles) and the electrical field at the dipole moment is equal to the outer electric field, the mean dipole moment can be calculated, in the framework of Debye approach [128] and utilizing Boltzmann's statistics, as follows

$$\langle \mu \rangle = \frac{\mu^2}{3k_B T}\, E \tag{3.9}$$

where k_B is Boltzmann's constant. By inserting Eq. 3.9 into Eq. 3.8, the polarization can be calculated

$$P - P_\infty = \frac{\mu^2}{3k_B T}\, \frac{N}{V} E \tag{3.10}$$

Further, the change in the dielectric permittivity due to orientation polarization, $\Delta\varepsilon$, can be given by combining Eqs. 3.3 and 3.10. It holds

$$\Delta\varepsilon = \Delta\varepsilon_s - \Delta\varepsilon_\infty = \frac{1}{3\varepsilon_o} \frac{\mu^2}{k_B T}\, \frac{N}{V} \tag{3.11}$$

where $\varepsilon_s = \lim_{\omega \to 0} \varepsilon'(\omega), \varepsilon_\infty = \lim_{\omega \to \infty} \varepsilon'(\omega)$ covers all contributions to the dielectric function, which are due to induced polarization P_∞, $\Delta\varepsilon$ is also called the dielectric strength.

Dipole moments of in polymers: For long-chain molecules there are three different geometric possibilities for the orientation of molecular dipole vectors with respect to the backbone. A classification gives Figure 3.1. Type A polymers are macromolecules with dipole moments oriented parallel to the backbone, e.g., cis-1,4-polyisoprene. For type B polymers, the dipole moment is perpendicular to the backbone of the polymer, e.g., poly(vinyl chloride). The last category named as type C polymers includes polymers, such as poly(methyl methacrylate), where the dipole moment is located within a flexible side chain. However, a polymer possessing only one type of dipole moment is an exceptional case [129]. The overall polarization is the sum of dipole density in a unit volume V.

For a macromolecule, the polarization can be written as

$$P = \frac{1}{V} \sum_{all\ chains} \sum_{chain} \sum_{repeating\ unit} \mu_i \tag{3.12}$$

In which $\mu_i$is the dipole moment of the repeating unit *i.*

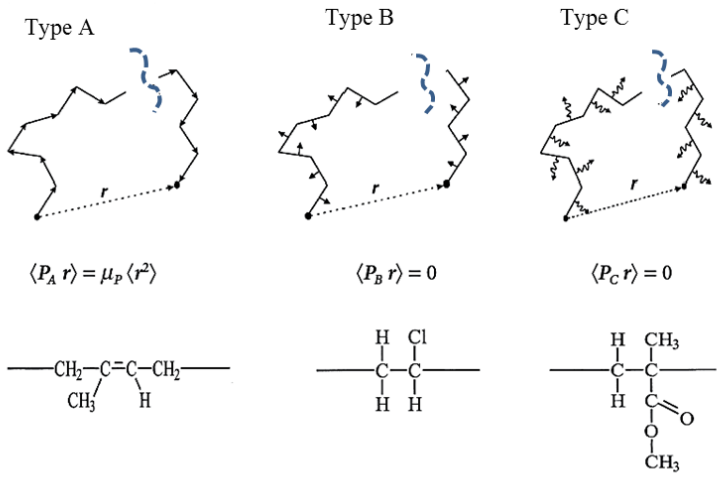

Figure 3.1 The different geometric possibilities for the location of molecular dipoles with respect to the polymer chain. Examples: Type A poly(cis-1,4-isoprene), type B poly(vinyl chloride), type C poly(methyl methacrylate). The figure was adapted from Ref. [130].

3.1.3. Time-dependent dielectric processes

The dielectric relaxation can be described in the framework of linear response theory (131), supposing that the electric field strength is small. The relevant materials equation which connects time dependent polarization *P(t)* and the time-dependent electric field *E(t)* is expressed by

$$P(t) = P_\infty + \varepsilon_0 \int_{-\infty}^{t} \varepsilon(t-t') \frac{dE(t')}{dt} dt' \tag{3.13}$$

$\varepsilon(t)$ is the time-dependent dielectric function. $\varepsilon(t)$ can be directly measured as response of the system caused by a step-like change of the external electric field as it is represented in Figure 3.2.

If the time dependence of the outer electric field is periodically $E^*(\omega) = E_0 \exp(-i\omega t)$, where ($\omega=2\pi f$) is the angular frequency, Eq.3.13 becomes

$$P(\omega) = \varepsilon_0 (\varepsilon^*(\omega) - 1) E^*(\omega) \tag{3.14}$$

Further, the relationship of the complex dielectric function $\varepsilon^*(\omega)$ and the time-dependent dielectric function $\varepsilon(t)$ is given by

$$\varepsilon^*(\omega) = \varepsilon'(\omega) - i\varepsilon''(\omega) = \varepsilon_\infty - \int_0^\infty \frac{d\varepsilon(t)}{dt}\exp(-i\omega t)dt \tag{3.15}$$

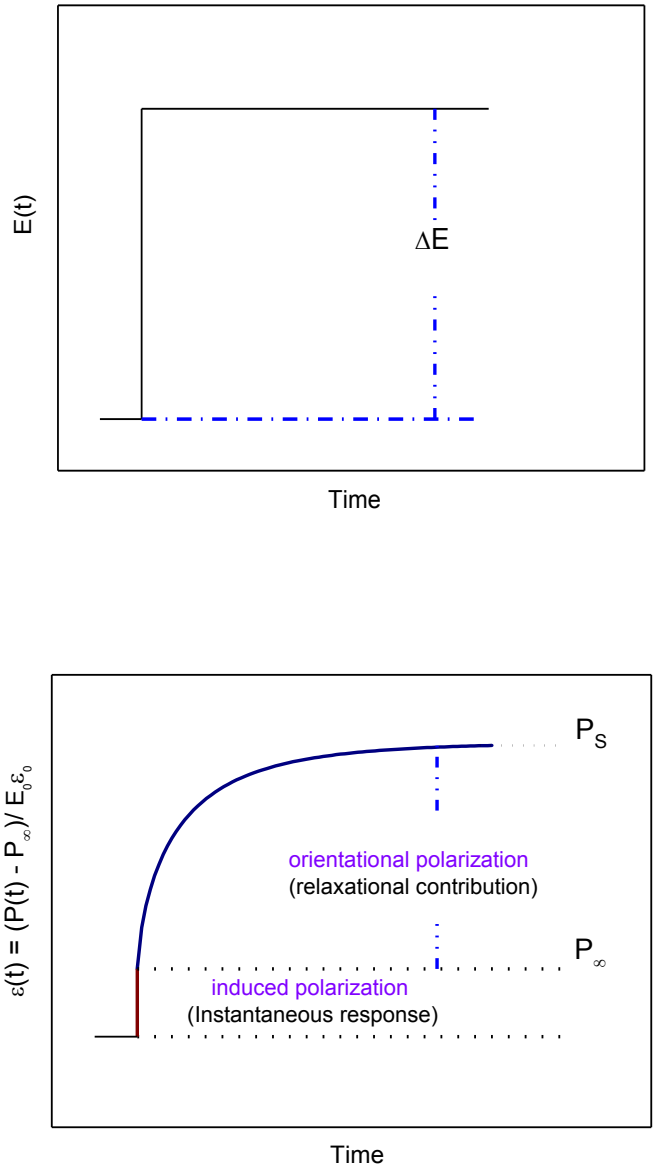

Figure 3.2: Schematic relationship between the time dependence of the electric field ΔE (upper panel), the polarization P(t), and the time-dependent dielectric relaxation function $\varepsilon(t)$ (lower panel). The figure was adapted from Ref. (132).

Figure 3.3 shows the relationship between P (t) and E (t) on the one side and ε' and ε'' on the other side. ε* is drawn a simple vector diagram. The tangent of the phase angle δ (dissipation factor) is given by

$$\tan \delta = \frac{\varepsilon''}{\varepsilon'} \tag{3.16}$$

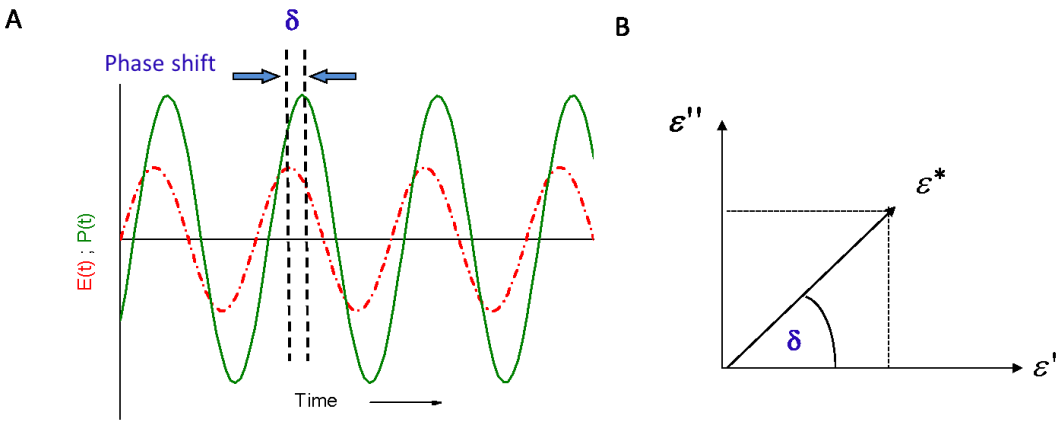

Figure 3.3 (A) Phase shift between the electric field and the polarization. (B) Relation between the complex dielectric function, its real part ε' and imaginary part ε'' as well as the phase angle (δ). Figure was adapted from Ref. (24).

3.1.4. Analysis of dielectric relaxation spectra

Debye relaxation process: The dynamic function for dielectric relaxation was introduced by Debye [128]. The Debye relaxation corresponds to a single relaxation time response of an ideal, non-interacting population of dipoles to an alternating external electric field. From a macroscopic point of view, the simplest approach to determine the time dependence of the dielectric behavior is the assumption that the change of polarization P is related to its actual value [128,133]

$$\frac{dP(t)}{dt} = -\frac{1}{\tau_D} P(t) \tag{3.18}$$

here, τ_D stands for the characteristic time of Debye relaxation. The solution of this first order differential equation leads to an exponential decay

$$P(t) \sim \varepsilon(t) \sim exp(-\frac{t}{\tau_D}) \tag{3.19}$$

Referring to Eq. 3.15 of the complex dielectric permittivity $\varepsilon^*(\omega)$, the Debye equation is given by

$$\varepsilon^*(\omega) = \varepsilon_\infty + \frac{\Delta\varepsilon}{1 + i\omega\tau_D} \tag{3.20}$$

where $\Delta\varepsilon = \varepsilon_s - \varepsilon_\infty$ is the dielectric strength, ε_s represents the static permittivity, and ε_∞ is the unrelaxed permittivity, which contains only contributions coming from induced polarization. The Debye relaxation time τ_D is related to the frequency of loss peak by $\tau_D = 1/2\pi f_P = 1/\omega_p$. The separation of $\varepsilon^*(\omega)$ into the real part and imaginary part is given as follow;

$$\varepsilon'(\omega) = \varepsilon_\infty + \frac{\Delta\varepsilon}{1+\omega^2\tau_D^2}; \qquad \varepsilon''(\omega) = \Delta\varepsilon\frac{\omega\tau_D}{1+\omega^2\tau_D^2} \tag{3.21}$$

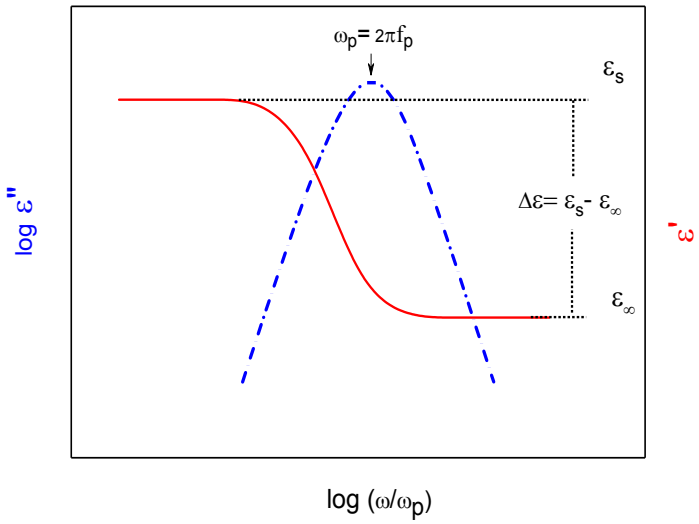

Figure 3.4: Frequency dependence of the real part ε' and imaginary part ε" of complex dielectric function ε according to the Debye function. Figure was adapted from Ref (24).*

Figure 3.4 shows the frequency dependence of the real and imaginary part of the Debye function. In general, the real part of the complex dielectric function ε' gives a stepwise decrease, where the imaginary part of the complex dielectric function ε'' shows a symmetric peak.

Non-Debye relaxation behavior: In practice, it was found that most polymers do not show a Debye behavior. The relaxation processes are much broader than the Debye spectrum and are usually asymmetric. Therefore, several models have been developed to generalize the Debye relaxation [128]. The Cole/Cole (CC) describes a symmetric broadening of the relaxation function given by

$$\varepsilon^*(\omega) = \varepsilon_\infty + \frac{\Delta\varepsilon}{1 + (i\omega\tau_{CC})^\beta} \tag{3.22}$$

where the β value describes a symmetric broadening of the peak (0<β≤1) and τ_{CC} is the characteristic time. Further, an asymmetric broadening of the relaxation function can be described by the Cole/Davidson (CD) function written as

$$\varepsilon^*(\omega) = \varepsilon_\infty + \frac{\Delta\varepsilon}{(1 + i\omega\tau_{CD})^\gamma} \tag{3.23}$$

where γ $(0< \gamma \leq 1)$ characterizes an asymmetric broadening of the relaxation function for frequencies ω >$1/\tau_{CD}$ where τ_{CD} is the Cole/Davidson-relaxation time.

The model function introduced by Havriliak and Negami (HN-function) (134) is the combination of the CC and CD models, which describes symmetric and asymmetric broadening of the dielectric function. It is read as

$$\varepsilon^*(\omega) = \varepsilon_\infty + \frac{\Delta\varepsilon}{(1+(i\omega\tau_{HN})^\beta)^\gamma}, \tag{3.24}$$

β and γ are the fractional shape parameters, which describe the symmetric and asymmetric broadening of the complex dielectric function $0 < \beta \leq 1$ and $0 < \beta\gamma \leq 1$ holds. The HN relaxation time τ_{HN} is related to the position of the maximal loss ω_p as follows [134].

$$\omega_p = \frac{1}{\tau_{HN}}\left[\sin\frac{\beta\pi}{2+2\gamma}\right]^{1/\beta}\left[\sin\frac{\beta\gamma\pi}{2+2\gamma}\right]^{-1/\beta} \quad (3.25)$$

Real and imaginary parts of HN-function are given as follows

$$\varepsilon'(\omega) = \varepsilon_\infty + \Delta\varepsilon\, r(\omega)cos[\gamma\psi(\omega)]\ ; \qquad \varepsilon''(\omega) = \Delta\varepsilon\, r(\omega)sin[\gamma\psi(\omega)] \quad (3.26)$$

with

$$r(\omega) = \left[1 + 2(\omega\tau_{HN})^{\beta}cos\left(\frac{\beta\pi}{2}\right) + (\omega\tau_{HN})^{2\beta}\right]^{-\gamma/2} \quad (3.27a)$$

and

$$\psi(\omega) = arctan\left[\frac{sin(\beta\pi/2)}{(\omega\tau_{HN})^{-\beta} + cos(\beta\pi/2)}\right] \quad (3.27b)$$

3.1.5. Conductivity contribution

The relationship between the complex dielectric function and the complex conductivity is given in Eq. 3.5. For semiconducting disordered materials like conducting polymers, the frequency dependence of the real part of the complex conductivity $\sigma'(\omega)$ is characterized by the following features. (1) $\sigma'(\omega)$ decreases with decreasing temperature and frequency with a power law ($\sigma'(\omega) \sim \omega^s$, with $0.5 \leq s \leq 1$) down to a given critical frequency ω_c. The parameter s increases with decreasing temperature. (2) For frequencies $\omega < \omega_c$, $\sigma'(\omega)$ has a plateau at temperatures where charge transport is enabled. (3) In a good approximation, a time-temperature superposition can be supposed by scaling the normalized conductivity $\sigma'(\omega)/\sigma_{dc}$ with respect to a normalized frequency ω/ω_c. (4) Between σ_{dc} and ω_c the Barton-Nakajima-Namikawa (BNN) - relationship holds ($\sigma_{dc} \sim \omega_c$) [135-137].

Different models exist to explain these observations on a microscopic level. One of them is the random free-energy barrier model proposed by Dyre [138], which characterizes the frequency-dependent conductivity over a wide range of frequencies at constant temperature. Within the framework of this model, it assumed

that charge carriers are non-interacting and remain at sites with minimum energy. Under some conditions charge carriers obtain sufficient energy, from their environment, to overcome the energy barrier and to hop to the nearest-neighbor site. Thus, hopping is assumed to be a basic mechanism for the conduction. Dyre derived the analytical equation for describing conductivity in the disordered solids:

$$\sigma^*(\omega) = \sigma_{dc}\left[\frac{i\omega\tau_e}{\ln(1+i\omega\tau_e)}\right] \tag{3.28}$$

where $1/\tau_e = \omega_e$ is the attempt rate of charge carriers to overcome the highest energy barrier (determine the onset of the dc conductivity). Eq. 3.28 can be deviated in real and imaginary part, more details for the random free-energy barrier model can be found elsewhere [138].

The frequency dependence of the real part of complex conductivity function can also be approximated by the well-known Jonscher power law [139].

$$\sigma'(\omega) = \sigma_{dc}[1 + (\omega/\omega_c)^s]. \tag{3.29}$$

The critical frequency ω_c emphasizes the onset of the dispersion and is related to the dc conductivity by the empirical BNN ($\sigma_{dc} \sim \omega_c$). By fitting the Jonscher equation to the data, both σ_{dc} and ω_c can be obtained.

The dc conductivity is defined as product of the charge carrier density n and its mobility $\mu_{mob.}$. The latter can be related to a diffusion coefficient $D_{diff.}$, and further to a characteristic diffusion jump rate ω_c, according the Einstein and Einstein-Smoluchowski equation [140]

$$\sigma_{dc} = nq\mu_{mob.} = \frac{nq^2}{k_B T} D_{diff.} = \frac{nq^2}{kT}\frac{\lambda^2\omega_c}{2} \tag{3.30}$$

where n denotes the effective number density, q is the elementary electric charge, k_B the Boltzmann constant, and λ denotes the hopping length.

Figure 3.5 gives a scheme of change in temperature dependence of the conductivity relaxation time, τ_σ, from a VFT dependence at temperatures above the glass

transition temperature measured by DSC, T_g, to an Arrhenius-like temperature dependence at temperatures below T_g. This could be observed if the motion of charge carriers becomes faster than the segmental dynamics as the T_g is approached signifies *decoupling phenomenon*.

It was Angell [141,142] who first defined decoupling index is that the ratio of the structural relaxation time, τ_α, to the conductivity relaxation time, τ_σ. It is read as

$$R_\tau(T) = log[\tau_\alpha\,(T)\,/\tau_\sigma\;\;(T)] \tag{3.31}$$

The degree of the decoupling R_τ is estimated by assuming that the thermal glass transition temperature is related to a structural relaxation time of τ_α =100 s.

Recently, a further empirically definition of a decoupling index has been represented [143].

$$log\;(R_1) = 14.3 + log\sigma_0(T_g) \tag{3.32}$$

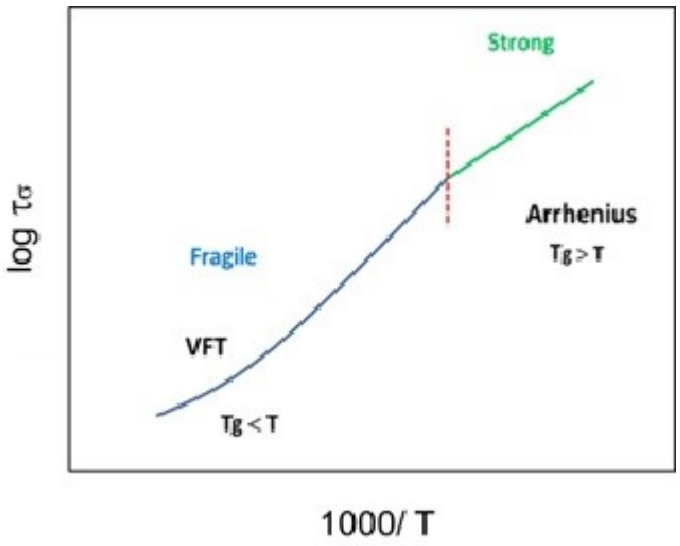

Figure 3.5: Schematic displays temperature dependence of the conductivity relaxation times τ_σ plotted as a function of 1000/T. The green line represents strong behavior and can be fitted by the Arrhenius equation. The blue curve represents fragile behavior and can be described by VFT function.

3.1.6. Maxwell Wagner Sillars (MWS) polarization

A Further contribution to the dielectric response is interfacial polarization or Maxwell/Wagner/Sillars (MWS) polarization [144,145], where charge carriers are

accumulated at internal interfaces (phase boundaries). Thus, the precondition for the observation of a MWS polarization is that the different phases have different dielectric properties. Interfacial polarization contributions are wildly observed for heterogeneous systems, e.g. polymer blends, semi-crystalline polymers, liquid crystalline materials or colloids. More details about dielectric behavior of heterogeneous materials can be found in literature [146-149]. It is worth mentioning that all properties of the process related to MWS polarization such as its position, its shape, and its strength depend on the geometry and conductivity of the dispersed phase, the complex permittivity as well as the dielectric properties of the matrix.

Moreover, charge carriers can be blocked at electrode surfaces cause an electrode polarization [24]. Under influence of outer electric field, the free charge carriers can move through the sample results in conductivity contributions. In both MWS and electrode polarization give rise to a separation of charges, which produces an additional contribution to the polarization. The charges may be separated over a significant distance. Thus, the contribution to the dielectric loss can be by orders of magnitude larger than the dielectric response owing to dipole relaxations.

3.1.7. Dielectric measurements

Here, the dielectric measurements were carried out in the frequency domain. Usually the results of dielectric measurements are presented as spectr of the real and imaginary part of the complex dielectric permittivity. In principle, the polarization is measured as a response of the system caused by a step-like change of the outer electric field as mentioned (see section 3.1.3). For a capacitor C^* filled with a material under study, the complex dielectric function $\varepsilon^*(\omega)$ is given as

$$\varepsilon^*(\omega) = \frac{C^*(\omega)}{C_o} = \frac{1}{i\,\omega\,Z^*(\omega)\,C_o} \tag{3.33}$$

where C_0 ($C_0 \sim A/d$, the plates of a capacitor are separated by distance *d* and have an area A) is the capacitance of the unfilled capacitor. According to Eq. 3.34, the complex dielectric function $\varepsilon^*(\omega)$ [24] can be determined by measuring the complex impedance $Z^*(\omega)$ of the sample.

In present work, the complex dielectric function was measured by a high resolution Alpha analyzer with an active sample head (Novocontrol GmbH, Germany) in the frequency range from 10^{-2} -10^{7} Hz and in the temperature interval from 173 to 423 K. It is important to note that, for two sets of HPAE and HPAMAM, the highest temperature range of the measurements was limited to 323 K. However, for Hybrane samples, the temperature interval from 173 to 423 K was used. The measurements were done isothermally where the temperature is controlled by a Quatro Novocontrol cryo-system with a stability of 0.1 K. For more details (see Ref. [24]). The samples were prepared between two gold-plated stainless-steel electrodes of 20 mm in diameter in parallel plate geometry. Figure 3.6 illustrates the schematic set up cell of samples and the image of the two measuring electrodes. Fused silica fibers with a diameter of 50 µm were used as spacer.

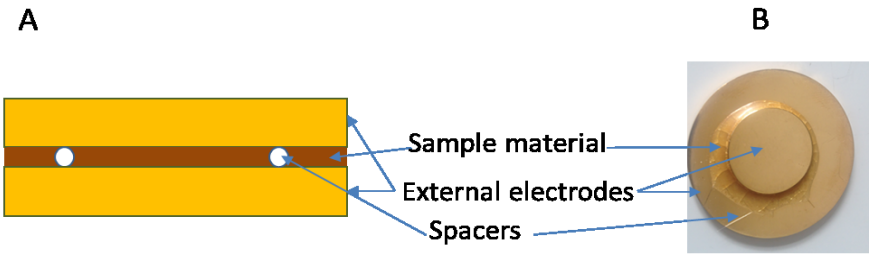

Figure 3.6: (A) Schematic set up cell. B) Image of a sample between two gold measuring electrodes.

3.1.8. Fitting HN-function to the experimental results

To analyze the results of dielectric measurements the model functions were fitted to the dielectric data. If multiple relaxation processes are observed in the frequency range, the fit of more than one HN-function can be used to describe and furthermore to separate the different processes. The spectrum is then analyzed on the basis of a sum of different relaxation functions. For example, if two relaxation processes are observed within the experimental frequency window, a sum of two HN-functions is fitted to the experimental data.

By fitting the HN-function to the data, the essential quantities such as the frequency of maximal loss f_P, the dielectric strength, and the shape parameters can be obtained. These quantities characterize of a dielectric relaxation process.

Further, various relaxation processes like conduction effects contribute to the dielectric spectra of a complex system. This effect can be treated by adding a contribution $\sigma/[(2\pi f_P)^s \varepsilon_o]$ to the dielectric loss, where σ is related to the specific dc conductivity of the sample. The parameter s ($0 < s \leq 1$) describes for s=1 Ohmic and for s < 1 non-Ohmic effect in the conductivity [24].

3.2. Specific heat spectroscopy (SHS)

For most HBPs, the segmental relaxation (α-relaxation) cannot or only hardly be detected by BDS, due to the overlapping conductivity contributions [33-31]. Thus, in the current work, specific heat spectroscopy (SHS) was used as a complementary method to study the segmental dynamics (α-relaxation). Practically, broadband dielectric and specific heat spectroscopy provide different windows to look at the glassy dynamics phenomena. Schawe [150] first formulated the specific heat spectroscopy in the framework of the linear response theory. In this case, a modulation of temperature is applied, as disturbance, which results in a modulated heat flow. This result is a change in the entropy (or enthalpy) of the sample investigated. The heat flow is phase-shifted if a time-dependent process is taking place within the sample. The corresponding material function is the complex specific heat capacity

$$c_p^*(\omega) = c_p'(\omega) - ic_p''(\omega) \tag{3.34}$$

where $c_p'(\omega)$ and $c_p''(\omega)$ represent the real and imaginary part of complex heat capacity, respectively.

In this work, SHS measurements were carried out by employing differential AC-chip calorimetry. The measurements are performed in a broad frequency range, combined with a high sensitivity of pJ/K.

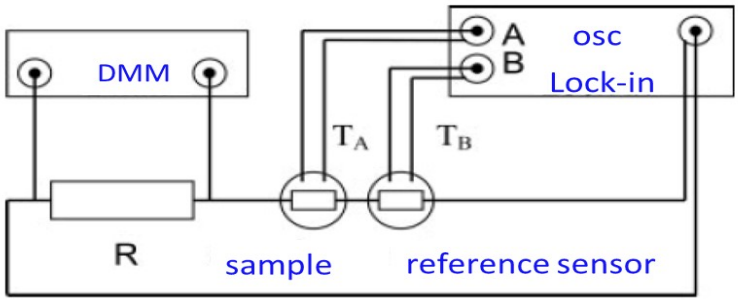

Figure 3.7: Scheme of the machine setup. Using the internal generator of the lock-in amplifier results in better phase stability. The differential signal A–B of the thermopiles is analyzed and further processed. The voltage over the known resistor R is measured with a digital multimeter to evaluate heater power. A computer controls all components. Figure was adapted from Ref. [36].

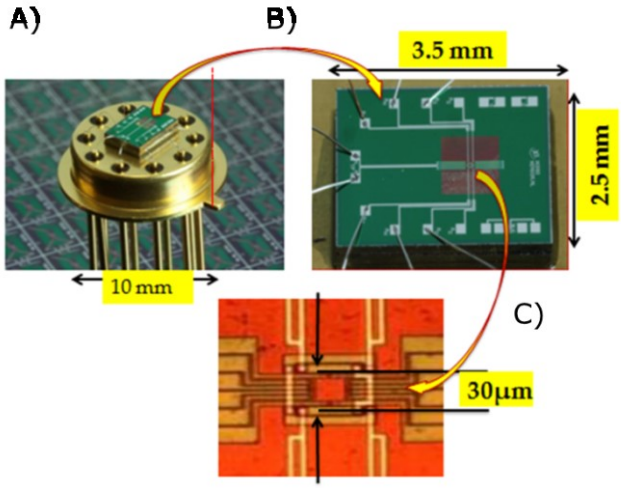

Figure 3.8: Chip sensor for the AC calorimeter (A) Photograph of the thermal conductive pressure gauge from Xensor Integration NL. (B) Silicon nitride membrane fixed at 3.3×2.5 mm rectangular frame. (C) Magnified center area of the membrane with the heater indicated by the two vertical arrows and thermopile hot junctions placed around it. Figure was adapted from Ref. [36].

Principally, the chip itself will contribute to the measured heat capacity. In the differential approach to AC-chip calorimetry, the contribution of the heat capacity of the empty sensor (without a sample) to the measured signal is minimized. In the approximation of thin films (submicron), the heat capacity of the sample C_S is then given

$$C_S = i\omega\overline{C}^2(\Delta U - \Delta U_0)/SP_0 \tag{3.35}$$

where ($C \equiv \overline{C}_0 + G/i\omega$) denotes the effective heat capacity of an empty sensor hence, G/iω is the heat loss through the surrounding atmosphere, S is the sensitivity of the thermopile and P_0 is the applied heating power. ΔU is the complex differential thermopile signal for an empty reference sensor and a chip with a sample, where ΔU_0 is the complex differential voltage measured for two empty sensors. The amplitude and the phase angle of the complex differential voltage are considered as measure for the complex heat capacity.

A schematic of the experimental setup is shown in Figure 3.7. The differential AC-chip calorimeter is based on a commercially available chip sensor, XEN 39390 (Xensor Integration, NL). The heater is fixed in the center of a freely standing thin silicon nitride membrane (thickness 1 µm) supported by a Si-frame with a window. This nanocalorimeter chip has a theoretical heated hot spot area of about 30 x 30 μm^2 with integrated 6-couple thermopiles and two-four-wire heaters (bias and guard heater), as shown in Figure 3.8 [151]. It is worth to note that besides the 30 x 30 μm^2 hot spot, the heater strips also contribute to the heated area. Further, the heaters and thermopiles are protected by a SiO_2 layer with a thickness of 0.5 - 1 µm.

During the measurements, the frequency was preserved constant with a rate of 1-2.0 K/min depending on the programmed frequency to ensure a stationary state. After each heating/cooling run, the frequency was changed stepwise in the range of 1 Hz – 10^4 Hz. The heating power for the modulation is kept constant at about 25 µW, which ensures that the amplitude of the temperature modulation is less than 0.25 K and thus, a linear regime.

To carry out the measurements, the empty sensors were first annealed for two hours at 473 K in vacuum, to completely cure the epoxy resin, which was used to glue the chip to the housing. Furthermore, sensors were then fixed on a sample holder and placed under an optical microscope. For HPAE and HPAMA and the corresponding nanocomposites, which were all in a viscous liquid-like form, at room temperature, a small drop was precisely placed on the heater area of the sensor, under the microscope.

3.3. Small angle X-ray scattering (SAXS)

SAXS is an analytical method to study the structure of materials. This technique provides not just information on the sizes and shapes of particles but also on the internal structure of disordered and partially ordered systems (intercalated /exfoliated nanocomposites). Further, it is an appropriate method to determine the interlayer spacing of the silicate layers. The basic concept and a detailed description of the methods can be found elsewhere [152-154]. Figure 3.9 shows the geometry of a typical scattering experiment. Where $\mathbf{k_f}$ is the scattered and $\mathbf{k_i}$ is the incident vector of the radiation. The scattering vector is defined in terms the scattering angle θ and the wavelength λ of the radiation (λ = 0.154 nm), thus $\boldsymbol{q}= (4\pi/\lambda) \sin\theta$. The overall SAXS scattering profile is calculated by subtracting the scattering profile of the empty capillary from the profile of the sample.

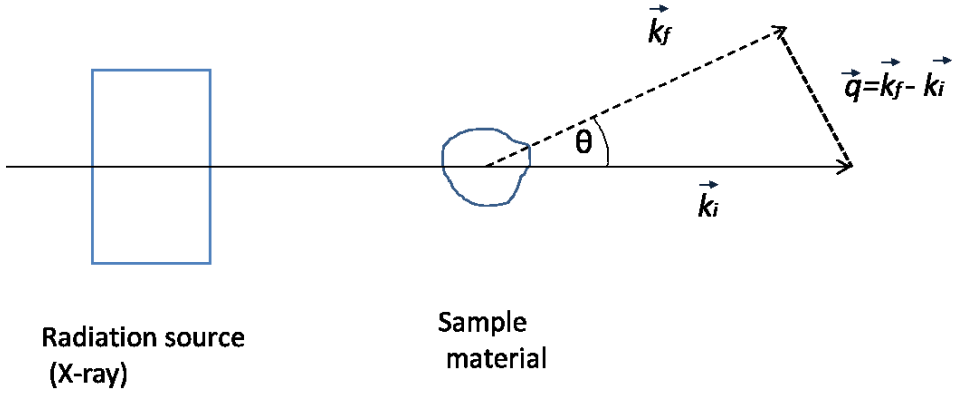

Figure 3.9: Scheme of the scattering process shows the interaction of radiation with the sample.

The measurements were carried out in a capillary with a Kratky-type instrument (SAXSess from Anton Paar, Austria) at 298 $\pm$ 1 K. The SAXSess has a low sample-to-detector distance (0.309 m), which is appropriate for the investigation of samples with low scattering intensities. Each sample was measured for 180 × 10 s. The measured intensity was corrected by subtracting the intensity of the empty capillary. Deconvolution (slit length desmearing) of the SAXS curves performed was with the SAXS-Quant software (Anton Paar, Austria).

3.4. Differential scanning calorimetry (DSC)

DSC is used to investigate the thermal transition, e.g. melting crystallization, and glass transition in polymers and their composites. The DSC instrument consists of two pans of the same material; one is called sample and the other reference pan. It important to notice, the sample pan has the material investigated and the reference pan is kept empty or contains a standard material such as Sapphire. To keep the same heating rate between two pans, the sample pan requires more heat than the reference pan. In DSC, the difference in heat flow to the sample and a reference at the same temperature is recorded as a function of temperature. The quantity that indicates how much heat Q a sample has to take for it to increase temperature by one degree is called heat capacity $c_p = Q/\Delta T$, in which ΔT is the change of temperature.

Thermal analysis was carried out by DSC, Seiko Instruments DSC 220C. The samples (~10 mg) were measured in appropriate temperature ranges (from173 to 373 K) with a heating and cooling rate of 10 K min^{-1}. Nitrogen was used as the protection gas. The T_g was taken as the inflection point of the heat flow of the second heating run.

3.5. Fourier transform infrared spectroscopy (FTIR)

FTIR spectroscopy is widely applied for the identification of the functional groups. This technique is sensitive to variations in the polymer structure, and thus it is used to understand structure and reactions of organic molecules. Basically, infrared spectroscopy is a technique based on the vibrations of the atoms of a molecule. The absorption spectrum is detected by passing infrared radiation through a sample and determining what amount of the incident radiation is absorbed at a particular energy. Further, the adsorption occurs in specific frequencies or wave numbers, which corresponds to the energy differences between vibration energy levels ($\Delta E = h\nu$, where h is the Planck constant (h = 6.626 × 10−34 J s) and ν is equivalent to the classical frequency). Thus, this absorption is characteristic to the bonds present in the molecule. In this work, FTIR was used to emphasize the reaction between the polymer and the nanofiller.

The infrared spectra of the samples were measured in the wave number range from 550 to 4000 cm^{-1} accumulating 64 scans at a resolution of 4 cm^{-1} using a Nicolet Nexus 8700 FTIR spectrometer (Nicolet, USA) using the ATR mode (Diamond Golden Gate, Nicolet, USA). All spectra were subjected to the ATR-correction for diamond, smoothed, and baseline corrected.

3.6. Transmission electron microscopy (TEM)

The structural analysis of nanocomposites is often done with TEM, where extensive imaging is wanted to confirm a representative visualized at the nanoscale of the material. The sample is thin enough for high energy electrons to transmit through it. To examine the morphology of prepared samples, a JEOL JEM-1230 transmission electron microscopy with an acceleration voltage of 80 keV was used. The samples were prepared as dilute suspensions of the corresponding nanocomposites in water. The probes of the nanocomposites were prepared by adding a small drop of the water dispersions onto a lacey carbon film-coated copper grid. The so samples investigated were dried to constant weight, in air and further in high vacuum.

4. MATERIALS AND PREPARATION

4.1. Materials

The natural Ka was supplied by Sinai Manganese Co., Egypt. Its chemical composition is [$Al_2Si_2O_5(OH)_4$]. Dimethyl sulfoxide (DMSO) [$(CH_3)_2SO$], methanol (MeOH), diethanolamine (DEA) [$HN(CH_2CH_2OH)_2$], dodecylamine (DCA) [$CH_3(CH_2)_{11}NH_2$], ethylenediamine (EDA) [$(C_2H_4(NH_2)_2$], and methyl acrylate (MA) [$CH_2CHCO_2CH_3$] were purchased from Aldrich Chemicals.

These materials were used for the preparation of hyperbranched polymamine ester (HPAE) and hyperbranched poly(amidoamine) (HPAMAM), and for the modification of the Ka. However, the third group, Hybrane S 1200, a hyperbranched polyester amide with a number-average molecular weight Mn = 1200 g/mol, was supplied by Polymer Factory, Sweden. Hybrane is amorphous with a T_g, of 306 K (Hybrane Safety Data).

4.2. Intercalation of kaolinite (Ka)

In this work, two different methods were applied to prepare three different series of HBP/ Ka nanocomposites. One approach was the solution “ex situ” approach and the other was “in situ” technique, a polymerization-based method.

For the ex situ approach, Ka was modified by dodecylamine (DCA). An ex situ blend processing route was applied to prepare (1) hyperbranched polyamine ester/ kaolinite (HPAE/Ka-DCA), (2) hyperbranched poly(amidoamine)/ kaolinite (HPAMAM/Ka-DCA), and (3) hyperbranched polyester amide/ kaolinite (Hybrane/Ka-DCA) nanocomposites. Here, the HBPs were firstly prepared and then mixed with the modified Ka (Ka-DCA).

For in situ polymerization approach, Ka was first modified by two different monomers: (1) Diethanolamine (DEA) to prepare hyperbranched polyamine ester/ kaolinite (HPAE/Ka-DEA), or (2) ethylenediamine (EDA) to prepare hyperbranched poly(amidoamine)/ kaolinite (HPAMAM/Ka-EDA). This method includes two steps; the first was the insertion of monomers (DEA or EDA) between the Ka interlayers to increase the interlayer space. The second step was then the polymerization of

monomers with methyl acrylate between layered of the modified Ka (Ka-DEA or Ka-EDA), to obtain HPAE/Ka-DEA or HPAMAM/Ka–EDA nanocomposites, respectively. A schematic modification of the Ka is shown in Figure 4.1. The modification process of the Ka will discuss, in details, in the following part.

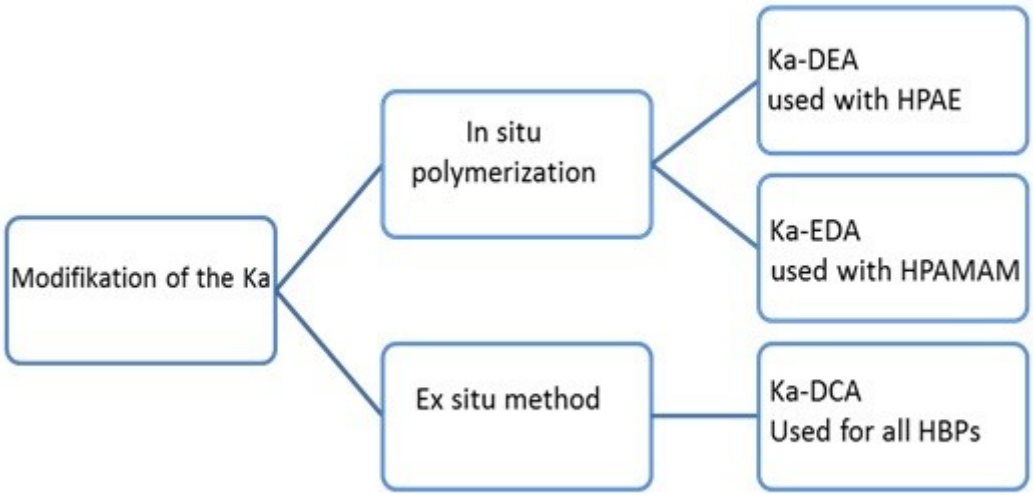

Figure 4.1: Scheme shows the different routes of the modified kaolinite used for different types of HBPs/nanocomposites.

Intercalation of DMSO into Ka: DMSO was grafted to the interlayer aluminol groups of Ka by dispersing 1 g of Ka in 10 ml of DMSO. The mixture was kept under continuous stirring (500 rpm), for 3 days at room temperature. Afterwards, the solution was filtered and washed with the same solvent before drying at 323 K for 24 h.

Intercalation of DEA into Ka-DMSO: The intercalation of DEA into Ka was performed by applying a melt-intercalation method, using the Ka-DMSO as preintercalated precursor. 1 g of Ka-DMSO was dissolved in 6 g of the amino alcohol (DEA). The temperature of the mixture was then slowly increased from room temperature to 353 K and kept at 353 K for 48 h. The resulting nanohybrid material was recovered after three times of centrifugation and washing in 50 ml isopropyl alcohol. Finally, the solid sample was dried at 333 K for 24 h.

Intercalation of DCA into Ka: Ka-DCA was prepared by the indirect intercalation method. DCA was intercalated into the interlayer space of Ka by utilizing the Ka-DMSO intercalation complex as an intermediate [33]. The intercalation was performed through of two steps: The first step is the replacement of DMSO from the dried powder of Ka-DMSO. To replace the DMSO efficiently, the Ka-DMSO product was dissolved in methanol (MeOH). The mixture was stirred at room temperature for 3 days, where the methanol was interchanged daily. The wet sample was then centrifuged, and a yellowish powder was obtained as Ka–MeOH. Second is the intercalation of DCA was prepared by adding 1 g of prepared Ka–MeOH to 10 mL of DCA solution and continuously shaken in a closed flask for 5 days. Afterward, the suspension was separated by centrifugation. The product was dried at room temperature for 24 h and then at 323 K for 24 h, to confirm that the MeOH would be fully removed. Finally, a fine powder was obtained.

Intercalation of EDA into Ka-DMSO: 5 g of Ka-DMSO, as a starting material, was dispersed into 30 g of EDA. The temperature of the mixture was increased slowly from temperature 293 K to 343 K and maintained stable for 48 h at this temperature. The resulting nanohybrid material was dried under vacuum at 333 K for 24 h. Finally, a fine powder was obtained.

The above-mentioned intercalation processes of the Ka yielded to increase the Ka-interlayer space, as revealed by SAXS measurements. Further, the modification of Ka was confirmed by FTIR, as will discuss in the following.

4.3. Characterization of the modified Ka

***SAXS*:** Figure 4.2A gives a wide-angle X-ray scattering pattern for pure Ka. The characteristic interlayer spacing for Ka d=0.717 nm (q_{max}=8.75 nm^{-1}) corresponding to a laminar stack of Ka layers was observed in agreement with literature data [155]. By fitting a Gaussian to the data, the width w of the main peak can be estimated. The correlation length in direction perpendicular to the lamella normal is $I_C=2\pi/\omega$ = 72.6 nm and the effective number of layers I_C/d=101. Figure 4.2B depicts the SAXS data of

Ka, Ka-DCA, Ka-DEA, and Ka-EDA. For neat Ka, no further reflections are detected in the SAXS range. For the modified Ka samples, the reflections are shifted to lower q values compared to the unmodified filler. The intercalation of DEA into Ka layers shows a reflection at q_{max} = 5.71 nm^{-1}, this value gives the effective interlayer distance of d=1.12 nm. This means that the intercalation of DEA increases the effective interlayer distance compared to the pure Ka. The correlation length was estimated to be 20.3 nm, hence I_C/d=18.

The intercalation of the larger molecule of DCA increases the effective interlayer distance to 3.6 nm, also in agreement with literature data [156]. The correlation length was estimated to be 354 nm and hence I_C/d=98. For intercalation of EDA, the width of the main peak determined by fitting a Gaussian to the data is w=0.105 nm^{-1}. The correlation lengths in direction perpendicular to the lamella normal are $I_C=2\pi/w$=60 nm. The intercalation of the EDA into the Ka layers gives a reflection at q_{max}=5.23 nm^{-1}. Thus, the intercalation of EDA led to increasing the effective interlayer distance to be d=1.2 nm. Further, the effective number of layers displays I_C/d=50 [157,158]. The data estimated from SAXS analysis for modified Ka and unmodified Ka was given in Table 4.1.

Table 4.1: Interlayer distance $d=2\pi/q_{max}$, the correlation length in direction perpendicular to the lamella $I_c=2\pi/w$, and the effective number of layers N.

Sample	d *(nm)*	I_c *(nm)*	N
Ka	0.717	72.2	101
Ka-DCA	3.60	354	98
Ka-DEA	1.12	20.3	18
Ka-EDA	1.20	60.0	50

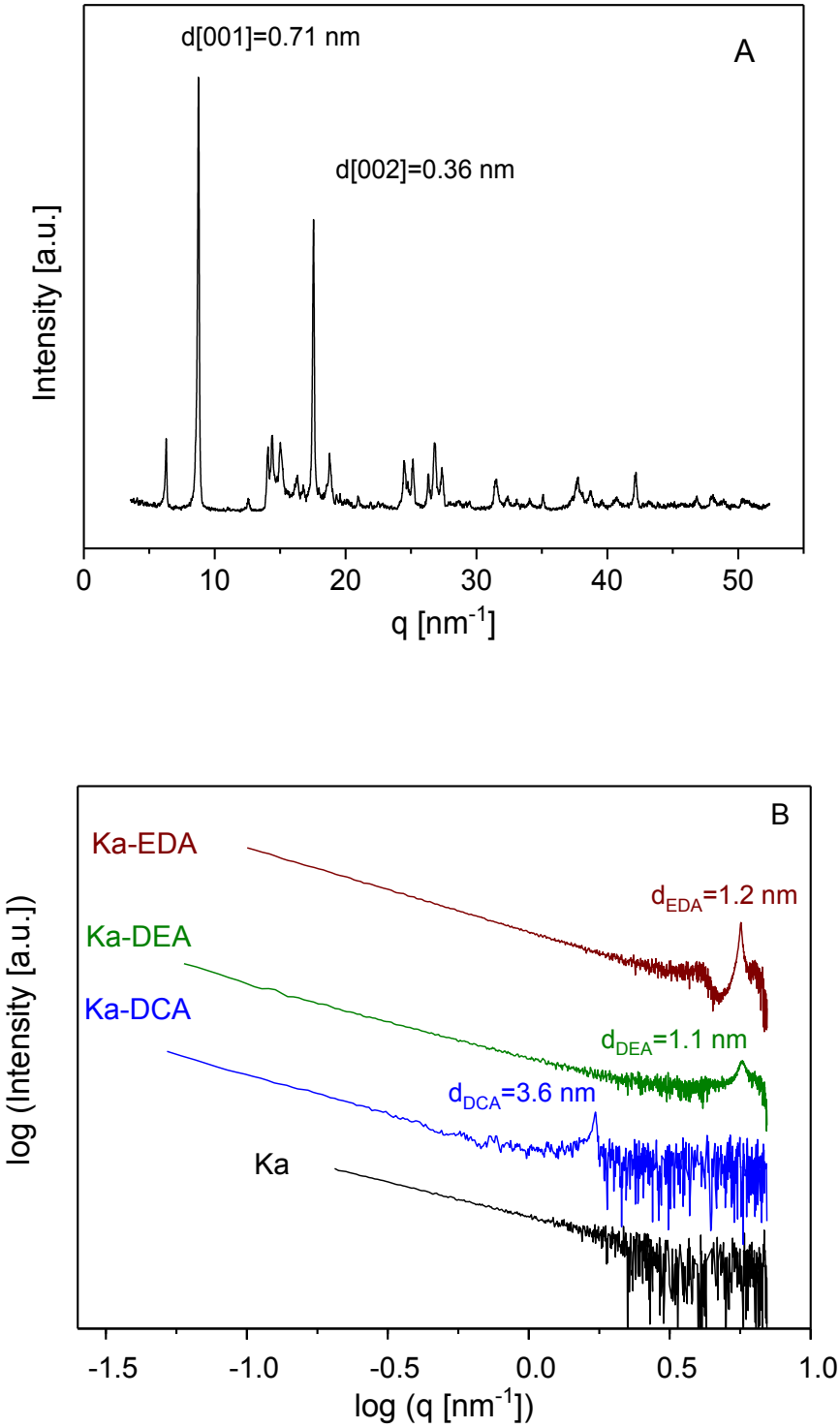

Figure 4.2: (A) Wide Angle X-ray data for pure Ka. The data were collected employing a computer controlled X-ray diffractometer at ambient conditions (National research center NRC Cairo, Egypt). (B) SAXS pattern of unmodified Ka, Ka-DCA, Ka-DEA, and Ka-EDA as indicated.

FTIR: The FTIR spectra of Ka, Ka-DCA, and Ka-DEA were given in Figure 4.3. The spectra for the unmodified clay shows the characteristic vibrations expected for Ka: the OH stretching peaks (3620, 3650, 3668, and 3689 cm^{-1}) and the vibrations to the Si-O and Si-O-Si groups in the wave number range of ca. 1000 cm^{-1}. The spectra are normalized by the intensity of the strongest peak. Figure 4.3B magnifies the spectra in the wave number range of the OH stretching vibrations. The peak at 3620 cm^{-1} is allocated to the inner OH groups were the other three peaks are related to the outer OH groups vibrations, at the surface of a Ka layer [159]. When DEA is intercalated into Ka the characteristic peaks for OH groups shifted to higher wave numbers (3658 and 3696 cm^{-1}). This is related to the host-guest interaction by the hydrogen bonding. Moreover, the strong peak for Si-O-Si stretching vibration of pure Ka at 1041 cm^{-1} is shifted to higher frequency of 1051 cm^{-1} in Ka-DEA [160]. The additional peak at 3545 cm^{-1} is specified to the NH stretching. This result also confirms the intercalating of DEA into Ka.

In the case of Ka-DCA, the splitting of the C-H stretching modes in the region of 2921 and 2853 cm^{-1} verifies that there is an interaction between the long alkyl chain of DCA and the Ka, in agreement with references [161,162]. Moreover, the vibrations of the OH groups are shifted to higher wave number as the case of Ka-DEA (see Figure 4.3B), which evidences grafting of DCA to the Ka layers. Further, a slight shift in the peak of DCA at 1593 cm^{-1} to 1580 cm^{-1}, which is allocated to NH_2 bending mode, was observed. The splitting in the stretching vibration of CH_2 groups of DCA at 1466 cm^{-1} [163] to two peaks 1488 and 1468 cm^{-1} after intercalation confirms the formation of hydrogen bonding between DCA and the silica tetrahedron (see Figure 4.3A).

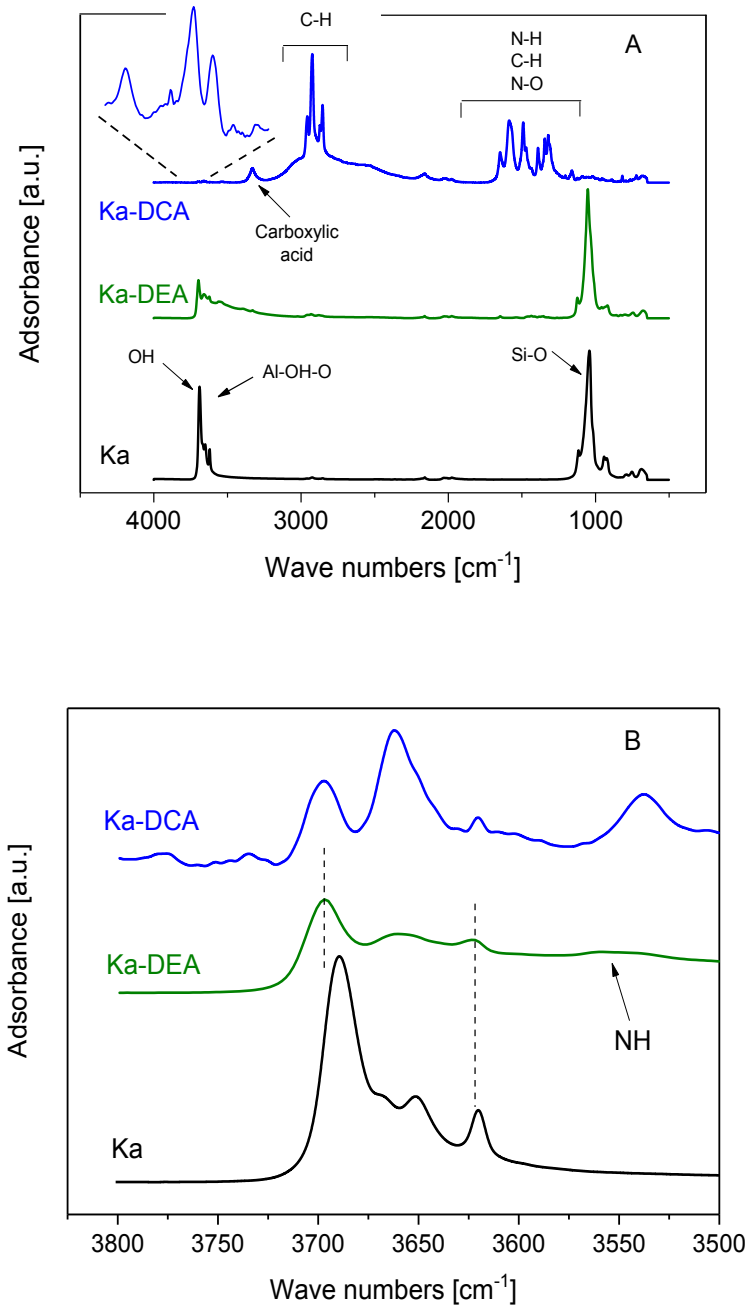

Figure 4.3: (A) FTIR spectra for Ka, Ka-DEA and Ka-DCA. (B) FTIR spectra for Ka, Ka-DEA and Ka-DCA in the wave number range from 3800 cm^{-1} to 3500 cm^{-1}.

Figure 4.4 shows IR spectra of the Ka-EDA. As previously mentioned (section 2.4), there are two types of hydroxyl groups exist in unmodified Ka: the inner-surface hydroxyl and the inner hydroxyl groups. The inner hydroxyl groups at 3620 cm^{-1} are usually not influenced significantly by the intercalation of an organic molecule into Ka. This different from the peak for the inner-surface hydroxyl at 3689 and 3651 cm^{-1}, which is shifted to 3696 and 3658 cm^{-1}. This shift reflects the intercalation reaction between EDA and Ka. The appearance of a new peak at 1656 cm^{-1} confirms the intercalation of the amino groups into Ka surface. Further, the specific peaks of pure Ka at 1041 and 941 cm^{-1}, which allocated to Si-O-Si stretching vibrations, are shifted to a lower frequency of 997 and 900 cm^{-1}. Further, the characteristic vibration of O-Al-OH at 750 cm^{-1} is shifted to lower wave number at 740 cm^{-1}, due to a formations of hydrogen bonding. This result is a further proof for the intercalation reaction. In other words, the change in the characteristic peaks of pure Ka (see Figure 4.3) and further the observation of the additional peaks at 3533 cm^{-1} assigned to the NH stretching, confirm the intercalating of EDA into Ka.

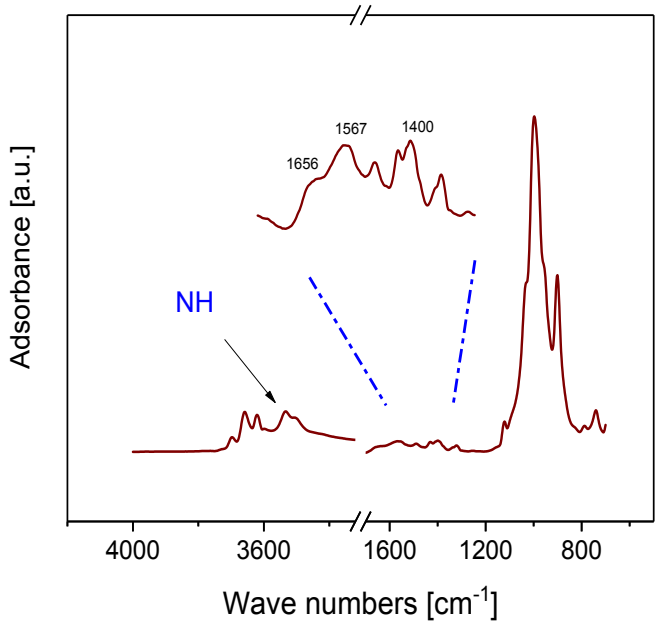

Figure 4.4: FTIR spectra for the Ka-EDA.

4.4. Preparation of HPAE/Ka nanocomposites

Preparation of pure HPAE: Multihydroxy HPAE was prepared by polymerization of DEA and MA with ratio of 1:1.2, using MeOH as a solvent. The mixture was stirred continuously at room temperature for 48 h. The solvent was then removed under reduced pressure on a rotary evaporator. The reaction was completed by keeping the mixture at 333 K for 1 h, at 373 K for 2 h, at 393 K for 2 h, and finally at 408-423 K for 2-4 h. After this temperature program, a yellow sticky polymer with a good solubility in water and methanol was obtained [4]. Figure 4.5 shows the structure of HPAE. The molecular weight of the formed polymer was estimated using size exclusion chromatography [Agilent 1100 series with RI detection, using linear polystyrene as a calibration standard, and N,N-dimethyl formamide (DMF) as eluent]. The weight average molecular weight (M_w), the number-average molecular weight (M_n), and the polydispersity index (PDI) $=M_w/M_n$ of the prepared HBP were estimated to 17300 g mol^{-1}, 10500 g mol^{-1} and 1.6, respectively.

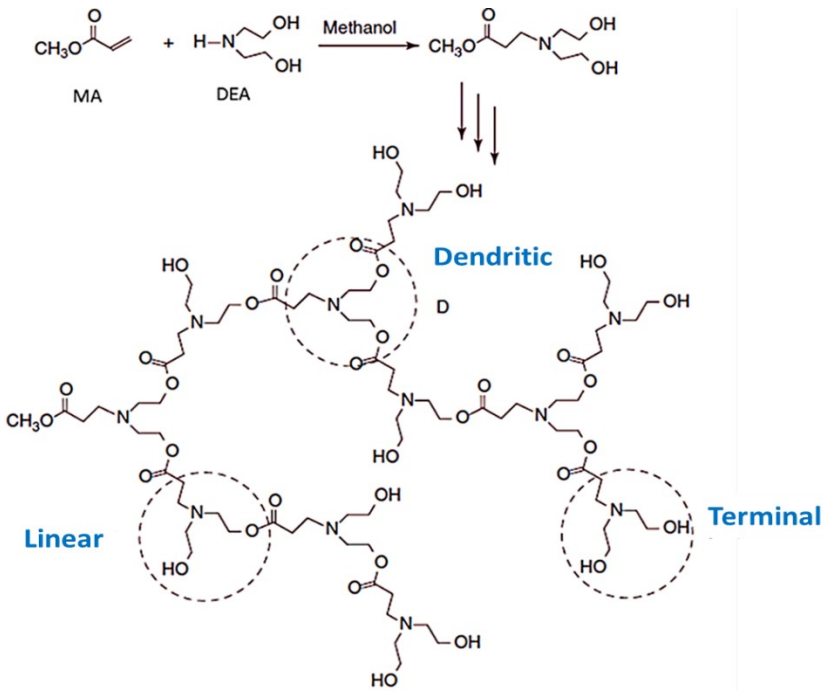

Figure 4.5: Structure of HPAE prepared by polymerization of methyl acrylate (MA) and diethanol amine (DEA) via the CMM method. The Scheme was adapted from Ref. [4].

The structure of HPAE was examined by ^{1}H NMR (see Figure.4.6). The polymer contains the expected three different kinds of OH groups: linear groups (N-CH_2-OH, δ=3.5 ppm; N-CH_2-CH_2-OH), δ=2.7 ppm), dendritic groups (CH_2-OCO, δ=4.05 ppm; CH_2-N, δ=3.4 ppm) and terminal groups (OH, δ=4.48 ppm).

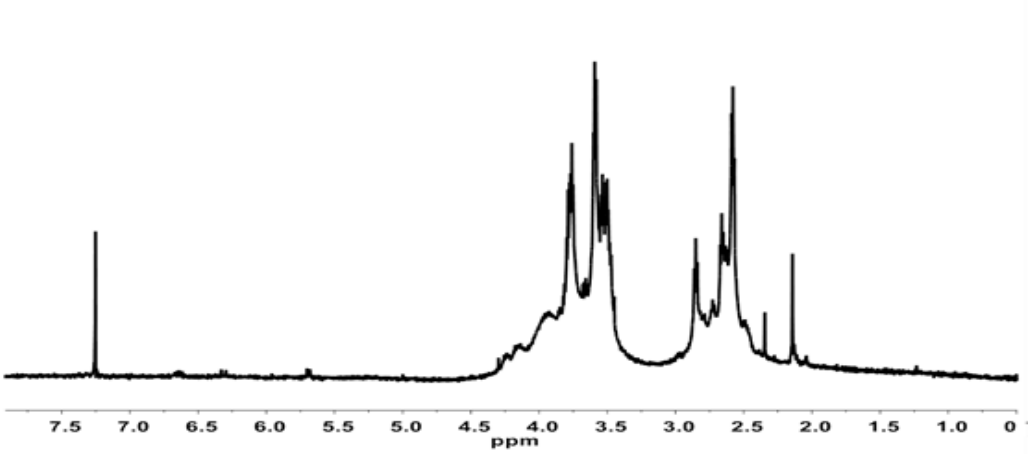

Figure 4.6: ^{1}H-NMR spectra for the hyperbranched polyamine ester (HPAE). The spectra were collected employing NMR spectrometer Varian Mercury- Oxford 500 MHz (National research center NRC Cairo, Egypt), using DMSO d_6 as the main solvent.

Preparation of HPAE/Ka by in situ polymerization: Ka-DEA was dispersed in methanol with different ratios by ultrasonicfiation for 24 h and added to DEA. The MA dissolved in methanol was added to the previously prepared mixture in the ratio of 1:1.2. The obtained mixture was continuously stirred at room temperature for 48 h. The solvent was then removed from the reaction system under reduced pressure using a rotary evaporator. The reaction temperature is increased to 333 K for 1 h and further followed by a temperature ramping: 373 K for 2 h, 393 K for 2 h and finally 408-423 K for 2-4 h. After the completion of the reaction, a yellow sticky nanocomposite was obtained.

Preparation of HPAE/Ka-DCA by ex situ method: 0.5 and 1 g of Ka–DCA were dispersed in two different flasks containing water. 10 g of HPAE, dissolved in 100 ml of distilled H_2O were added to the solutions of Ka-DCA and kept under continuous stirring at 323 K for 2 days. In the last step, the solvent was removed from the system

under reduced pressure using a rotary evaporator. Figure 4.7 shows a scheme of the in situ and ex situ method, to prepare different types of HPAE/Ka nanocomposites.

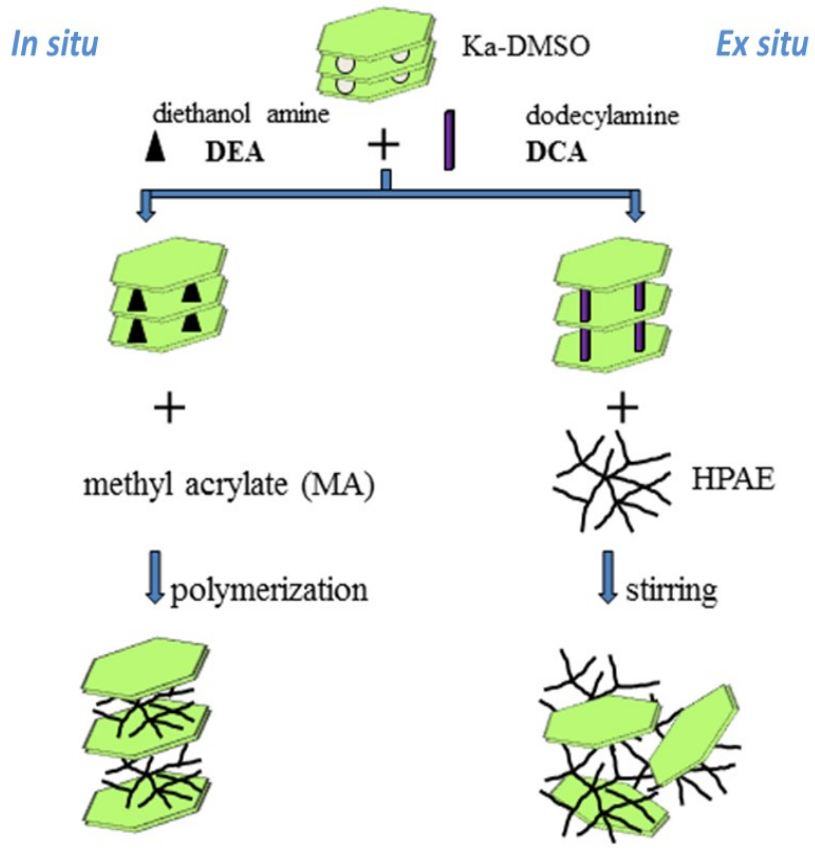

Figure 4.7: Scheme for the preparation of two different types of HPAE/Ka nanocomposites. The figure is taken from own publication [33].

4.5. Preparation of HPAMAM/Ka nanocomposites

Preparation of pure HPAMAM: The synthesis of HPAMAM was carried out as described by Yan et al. [4] based on ethylene diamine (EDA). In brief, a solution of methyl acrylate (MA) in methanol was added dropwise to an amine/methanol solution (feed ratio 1:1.2). The reaction mixture was kept at room temperature for 48 h. Methanol was removed from the reaction system under reduced pressure at 333 K by a rotary evaporator. Under vigorous stirring and vacuum distillation, the

mixture was kept at 333 K for 1 h, at 373 K for 2 h, at 393 K for 2 h, and finally at 408-423 K for 2 to 4 h. After this temperature program, a yellow sticky polymer with a good solubility in water and methanol was obtained.

Molecular weight measurements of the resulting polymer were carried out using size exclusion chromatography (SEC) [Agilent 1100 series with an RI detector, using polystyrene as a standard for calibration, and N,N-dimethyl formamide (DMF) as the eluent]. The weight average molecular weight (M_w) and the polydispersity index (PDI $=M_w/M_n$) of the prepared HPAMAM were found to be ca. 12500 g mol^{-1}, and 1.84 respectively. The prepared polymer has amido and amino groups in the backbone and many of primary amino units at the periphery. The chemical structure of HPAMAM (see Figure 4.8) was characterized by ^{1}H NMR [NMR spectrometer Varian Mercury- Oxford 500 MHz, using DMSO $_{d6}$ as the main solvent]. The ^{1}H-NMR (DMSO)-d_6 spectrum for HPAMAM is shown in Figure 4.8. The chemical shift (δ) from 1.75 to 2.34 ppm account for the hydrogen in NH or NH_2 which is not linked with a carbonyl group. The peaks at 8.01-7.92 ppm are related to the hydrogen of the amide group. The other observed peaks are assigned in agreement with literature [164,165] as follows: δ =2.30~2.49 ppm to $COCH_2$, δ=2.52~2.57 ppm to $COCH_2CH_2$, δ =2.63~2.7 ppm to $CH_2CH_2NH_2$, δ =3~3.12 ppm to NCH_2, and δ=3.4-4.0 to $COCH_3$.

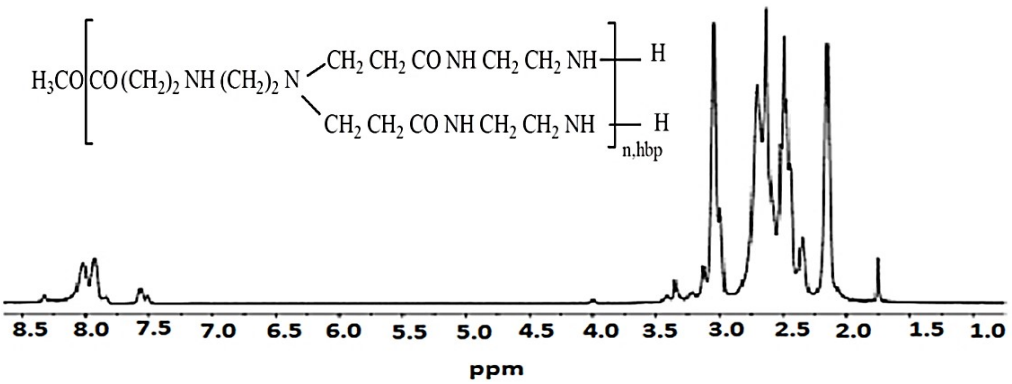

Figure 4.8: ^{1}H-NMR spectra for the hyperbranched poly(amidoamine) (HPAMAM). The spectra were collected employing NMR spectrometer Varian Mercury- Oxford 500 MHz (National research center NRC Cairo, Egypt), using DMSO d_6 as the main solvent. The inset gives a scheme of the chemical structure of HPAMAM.

Preparation of HPAMAM/Ka-EDA nanocomposites by in situ polymerization: During the in situ polymerization, the polymer is prepared between the interlayers of the clay. First, two rations from the Ka-EDA nanofiller were dispersed in methanol, by ultrasonicfiation for 24 h, and then added to EDA/ methanol solution. Second, MA/methanol solution was added dropwise to the formerly prepared mixture in the ratio 1:1.2. The obtained mixture was continuously stirred for 48 h at room temperature. Then the MeOH was removed from the reaction system under reduced pressure by a rotary evaporator. To complete the polymerization, a range of degrees of high temperature is applied as follow: the temperature of the reaction is increased to 333 K for 1 h, 373K for 2 h, 393K for 2 h and lastly 408-423 K for 2-4 h. After completion of the reaction, a yellow sticky nanocomposite was obtained.

Preparation of HPAMAM/Ka-DCA by ex situ method: An amount of 0.5, 1, and 2 g of the Ka–DCA were dispersed in three different flasks containing water. Further, 10 g of HPAMAM, dissolved in 100 ml of distilled water were added to the solutions of Ka–DCA and kept under continuous stirring at 323 K for 2 days. As a final step, the solvent was removed from the system under reduced pressure using a rotary evaporator.

4.6. Preparation of Hybrane /Ka-DCA nanocomposites

Figure 4.9 shows the chemical structure of Hybrane. The nanocomposites were prepared using the ex situ, solution intercalation, method. Hybrane was first dissolved in the water, which is a good solvent for this polymer. The Ka-DCA was dispersed in water and kept under continuous stirring for 24 h, to confirm that the clay would be fully dispersed in the water. Afterwards, the suspension was added to the polymer solution and kept under continuous stirring for 24 h. The solvent was removed from the system under reduced pressure using a rotary evaporator. Finally, all samples were annealed for 24 h at 373 K then for 24 h at 423 K under vacuum. Samples with different clay concentrations (10, 20, 30, 50, and 70 wt-%) were prepared.

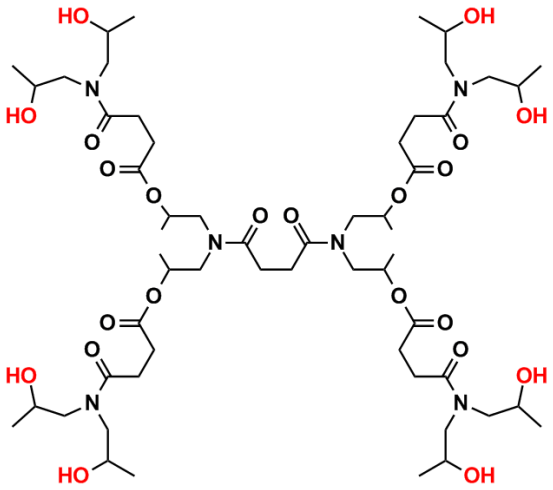

Figure 4.9: Chemical structure of hyperbranched polyester amide (Hybrane).

5. STRUCTURE-PROPERTY RELATIONSHIPS OF HPAE/KA NANOCOMPOSITES*

ABSTRACT: In situ polymerization and ex situ (a solution-based technique approach) methods were employed to prepare hyperbranched polyamine ester /kaolinite (HPAE/Ka) nanocomposites. The two methods resulted in different morphologies of the nanocomposites; Frist, an exfoliated structure for HPAE/Ka-DCA nanocomposites, which were prepared by in ex situ. In this method, the prepared HPAE was mixed with Ka, which was previously modified by dodecylamine (DCA). Second, an intercalated structure was observed for HPAE/Ka-DEA nanocomposites prepared by in situ polymerization. For this method, diethanolamine (DEA) was inserted as a monomer between the Ka layers and then polymerized with methyl acrylate. The structure-property relationship of bulk HPAE, and both types of nanocomposites were investigated by a combination of DSC, SAXS, FTIR, TEM, BDS, and AC-chip calorimetry.

5.1. Characterization of HPAE nanocomposites

Figure 5.1 indicates FTIR spectra for pure HPAE and HPAE/Ka-DEA nanocomposites. The peaks of pure polymer are identified as follows. The broad peak for O-H stretching vibration, around 3380 cm^{-1}, proves the existence of many terminal hydroxyl groups in HPAE. The peaks at 2948 and 2883 cm^{-1} are due to the symmetric $-CH_3$ and asymmetric stretching $-CH_2$ vibrations. The absorption peaks at 1051 $cm^{-1}$is due to C-O stretching vibrations. The band at 1477 cm^{-1} corresponds to the bending vibration of $-CH_2-$ groups. The sharp peak at 1620 cm^{-1} is related to N-H groups. It overlaps with the vibrations of the C=O groups, which were confirmed by NMR investigations for the bulk. This behavior was found for all ex situ and in situ samples and is consistent with the literature [166]. For the samples with 2 and 10 wt-% Ka-DEA, there are no major changes in the chemical structural of the polymer polymerized in the presence of the nanofillers.

* Similar content was presented in: Omara, S. S.; Abdel Rehim, M. H.; Ghoneim, A.; Madkour, S.; Thünemann, A. F.; Turky, G.; Schönhals, A.: Macromolecules.48, 6562-6573, (2015)

It was noticed that the characteristic absorption peaks of the hydroxyl groups in the Ka-DEA at 3696 cm^{-1} disappeared in the spectra of HPAE/Ka-DEA. The location of this peak is usually sensitive to intercalation of organic molecules. Similar results were found in Ref [167].

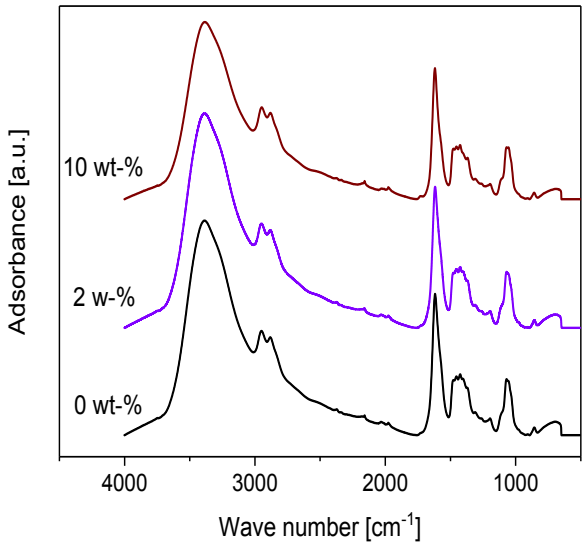

Figure 5.1: FTIR pattern for pure HPAE and HPAE/Ka-DEA nanocomposites (in situ) for 2 and 10 wt-% of the filler. For sake of clearness, the curves were shifted along the y-scale.

Figure 5.2 depicts the SAXS patterns for HPAE /Ka-DEA (in situ preparation). No Bragg peak is noticed for the composites, compared to the modified filler. Firstly, in the low q range the data follows the Porod law ($I \sim q^4$), which indicates the existence of well-defined surfaces within the systems due to the presence of the nanoparticles (see the curve for 10 wt-%). Secondly, for higher q values the q dependence of the scattered intensity is completely flat which is due only to background contributions (see the curve for 2 wt-%). There is no scattering intensity, which could be assigned to exfoliated objects like plates or discs, etc. This means the objects of the nanofiller in the sample must be larger than the scale defined by the q values of the SAXS experiment. The acceptable explanation that fits with these experimental results are stacks. The question arises why no Bragg peak is observed? To answer this question, one should keep in mind that already for modified Ka-DEA the observed Bragg peak is rather broad, much broader than for pure Ka and for Ka-DCA. This indicates that already for Ka-DEA the layered structure is highly disturbed with strong lattice

distortions. Furthermore, it is experimentally known that lattice distortions above 20 % will lead to a disappearance of the corresponding Bragg peaks. From these results, it is concluded that in the case of in situ polymerization, the nanofiller is organized in stacks. Because of the fact that no Bragg reflections are observed, which are characteristic for the filler, it must be further concluded that these stacks have a highly disturbed structure with no long-range correlation. These findings are consistent with the TEM investigations given in Figure 5.3A. Thus, for the in situ prepared nanocomposites, it can be concluded that they have partly intercalated structure.

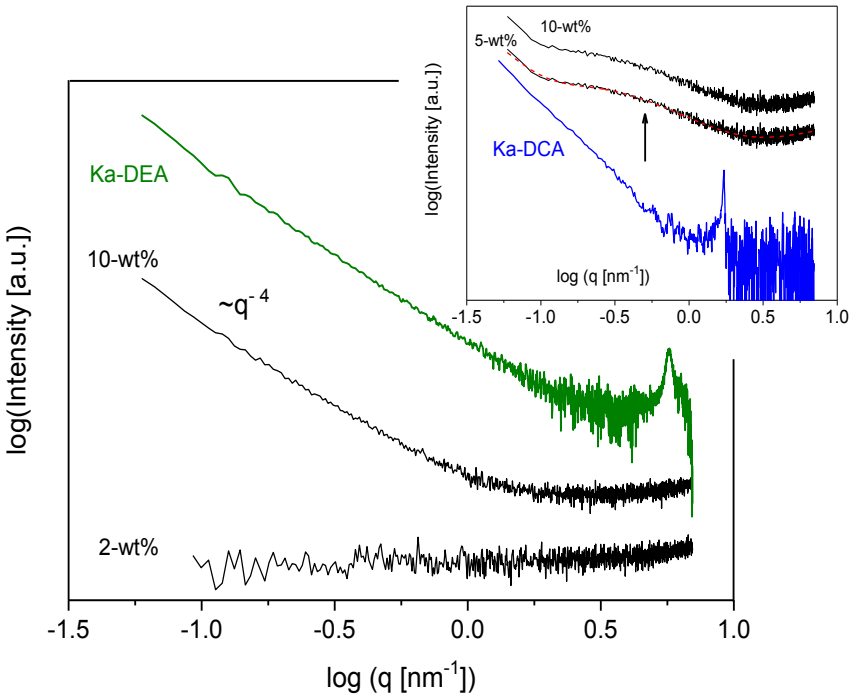

Figure 5.2: SAXS pattern for HPAE/Ka-DEA nanocomposites (in situ) for 2 and 10 wt-%. The inset gives the SAXS pattern for HPAE/Ka-DCA nanocomposites (ex situ) for 5 and 10 wt-% of the nanofiller.

The inset of Figure 5.3 displays the SAXS patterns for HPAE /Ka-DCA ex situ preparation. Here, also no Bragg reflection is detected, which is characteristic for the modified filler. In the q-range around 0.5 nm^{-1}, a broad scattering peak is detected for both concentrations of Ka-DCA. This pattern is related to the scattering of small

aggregates consisting of rod-like structures. This is also in agreement with TEM investigations (see Figure 5.3B). Unfortunately, no structure factor could be found in the literature to describe the scattering data exactly. Thus, a Lorentzian distribution is fitted to the data together with a Porod law and a background contribution. From the estimated position parameter of the distribution (5wt-%: 0.54 nm^{-1}; 10 wt-%: 0.13 nm^{-1}) an average size of the objects can be estimated to 11.6 nm and 48.3 nm. The size is larger for 10 wt-% of the nanofiller. Probably, the higher concentration of the nanofiller leads to larger aggregates. From the SAXS and the TEM results: one has to conclude that the HPAE/Ka-DCA nanocomposites ex situ preparation have a predominated exfoliated structure in agreement with Ref. [156].

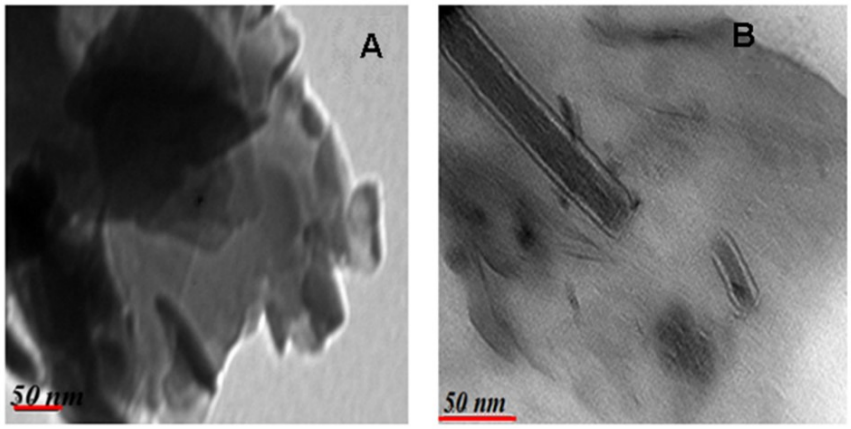

Figure 5.3: TEM pictures of the prepared nanocomposites for 10 wt-% of the filler. A - HPAE/Ka-DEA (in situ); B - HPAE/Ka-DCA (ex situ). This size bar represents 50 nm.

Figure 5.4 shows the DSC thermograms, in the temperature range of the thermal glass transition T_g, for HPAE/Ka-DEA. The T_g is obtained from the midpoint of the second heating run and given in Table 5.1. For in situ samples, the absence of any other endothermic or exothermic peaks confirms that these nanocomposites are amorphous [168] the T_g values for the samples with 2 and 10 wt-% Ka-DEA are similar to that of pure HPAE.

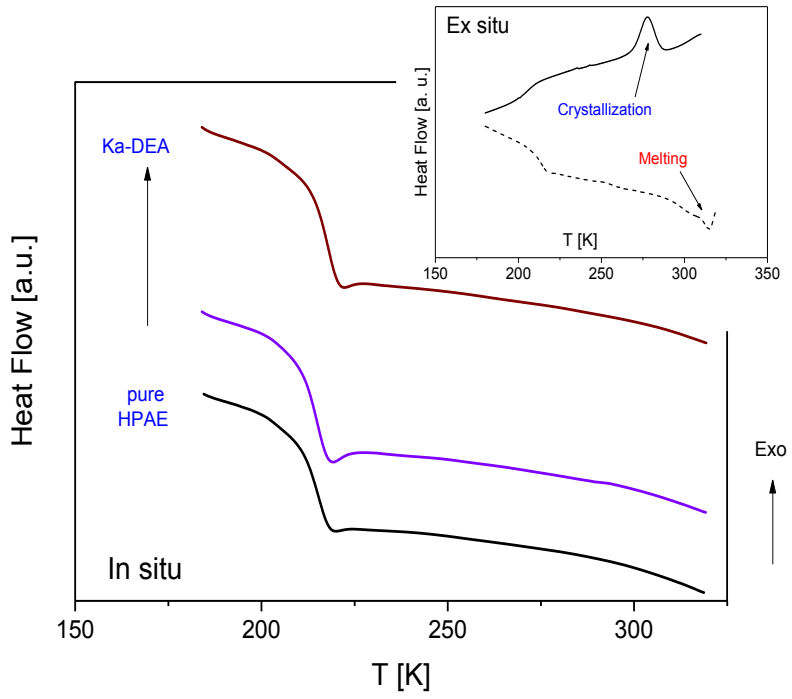

Figure .5.4: DSC thermograms for HPAE/ Ka-DEA nanocomposites prepared by the in situ method (10 K/min, second heating run): solid line – pure HPAE; dashed line – 2 wt-% KA-DEA; dotted line – 10 wt-% Ka-DEA. The inset shows the DSC thermograms of HPAE/Ka-DCA obtained by the ex situ approach, with 5 wt-% of the filler. Solid line – cooling run after heating; dashed line – second heating (rate 10 K/min).

Table 5.1: Glass transition temperature T_g (second heating), VFT parameters estimated from Specific Heat Spectroscopy, and fragility parameter D for the α-relaxation for pure HPAE and its nanocomposites. In addition, the activation parameters for the γ-relaxation are given.

	Sample	α-relaxation (Specific heat spectroscopy)					γ-relaxation	
		T_g [K]	log (f_∞ [Hz])	A [K]	T_0 [K]	D	log (f_∞ [Hz])	$E_{A,\gamma}$ [kJ/mol]
HPAE	0 wt-%	220	12	497.6	198.9	2.5	12.2	31
In situ	2 wt-%	219	12	608.7	176.8	3.4	11.3	28
	10 wt-%	222	12	756.6	160.1	4.7	13.1	33
Ex situ	5 wt-%	213	12	843.4	155.5	5.4	10.2	24
	10 wt-%	216	12	917.6	148.3	6.2	11.2	26

The inset of Figure 5.4 depicts the DSC thermograms of HPAE/Ka-DCA for 5 wt-% of the nanofiller for heating and cooling. There is a slight decrease of T_g for both

concentrations (see also Table 5.1). In addition to the glass transition, crystallization and melting peaks can be observed. Because of the fact that the pure HPAE do not show phase transitions (see Figure 5.4), the melting and crystallization must be attributed to the DCA. Probably, the long alkyl chains of DCA can and/or stimuli order like in alkenes. A similar behavior is found for 10 wt-% of Ka-DCA. To avoid any influence of these crystallization phenomena on the specific heat and dielectric spectroscopy investigations the highest temperatures of these measurements were limited to 323 K (5 wt-% Ka-DCA), or 333 K (10 wt-% Ka-DCA).

Specific heat spectroscopy is applied using AC-chip calorimetry, to investigate the glass transition behavior in more detail. According to Eq. (3.35), AC-chip calorimetry gives a complex differential voltage, which is related to the complex heat capacity, as a function of temperature and frequency. Here, the real part of the complex differential voltage U_R and the phase angle ϕ, are taken as measures of complex heat capacity. At the dynamic glass transition, U_R increases stepwise with increasing temperature (see Figure 5.5A), and the phase angle shows a peak (see Figure 5.5B). A dynamic glass transition temperature can be calculated as the half step temperature of U_R or as maximum temperature of the peak. In the raw data of the phase angle, there is an underlying step in the signal, which is proportional to the real part. Hence, the phase angle must be corrected by subtracting this contribution [34]. This subtraction is in some way arbitrary. Therefore, here a different method is employed to estimate the dynamic glass transition temperature. The real part of U_R is differentiated with respect to temperature. This procedure also leads to a peak (see Figure 5.5C). A Gaussian is fitted to these data and T_g is taken as the maximum temperature. Together with the frequency, the relaxation map can be constructed (see Figure 5.6) [169].

For pure HPAE, the temperature dependence of the relaxation rate $f_{p,\alpha}$ is curved when plotted versus 1/T as expected for the dynamic glass transition (Figure 5.6). The data can be described by Vogel-Fulcher-Tammann (VFT) expression (Eq. 2.3) [120-122].

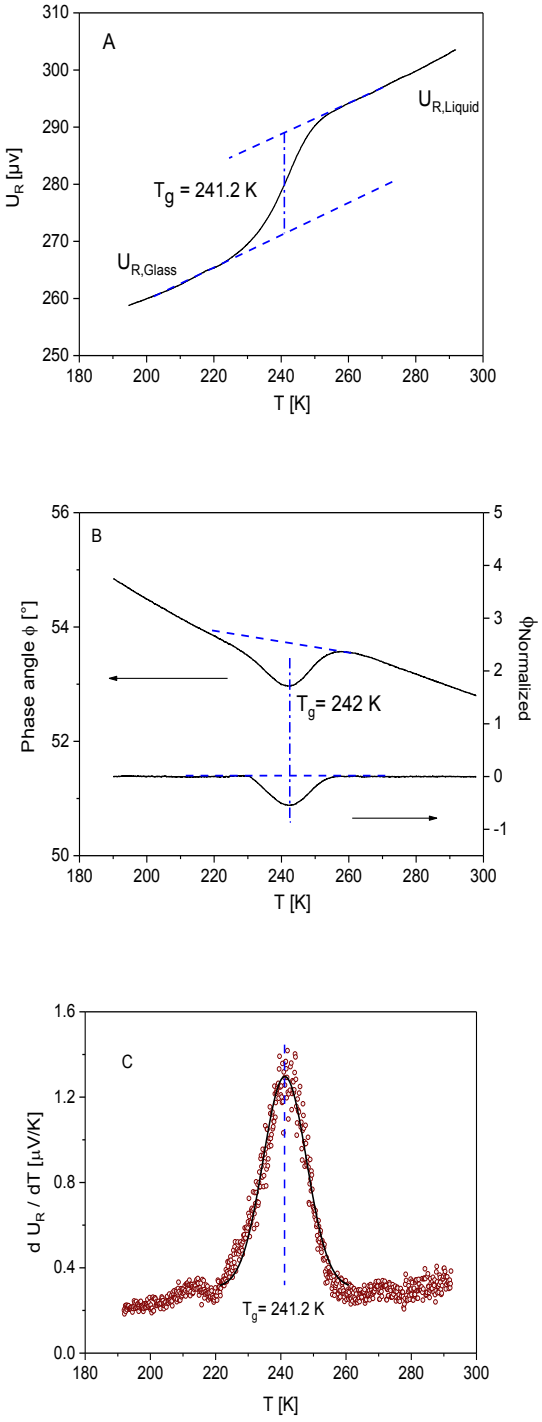

Figure 5.5: Example for an AC-chip calorimetry measurement for pure HPAE at a frequency of 160 Hz. (A): Real part of the complex differential voltage versus temperature. (B): Phase angle and corrected phase angle versus temperature. (C): Derivative of the real part of the complex differential voltage versus temperature. The line is a fit of a Gaussian to the data.

Here, it should be noted that the experimental error of an AC-chip calorimetry measurement is 2 to 3 K. In the case of the HPAE/Ka-DEA (in situ) nanocomposites with 2 and 10 wt-% nanofiller, the temperature dependence of $f_{p,\alpha}$ is in the same temperature region as that of pure HPAE. However, a closer inspection of the data reveals that there are systematic deviations of the temperature dependence of $f_{p,\alpha}$ for the Ka-DEA nanocomposites from that of pure HPAE. For the lowest measuring frequency, the observed differences are significantly larger than the error of AC-chip calorimetry. Also, the whole temperature dependence changes from fragile to stronger behavior. This is also observed from the calculated fragility parameter (see Table 5.1). The observed relaxation map is expected for a confined material [170].

The inset for Figure 5.6 gives the data for the HPAE/Ka-DCA nanocomposites. Also for this set of samples the data for the nanocomposite deviate substantially from that of pure HPAE. The VFT-dependence for the nanocomposites show a much stronger behavior than that of pure HPAE.

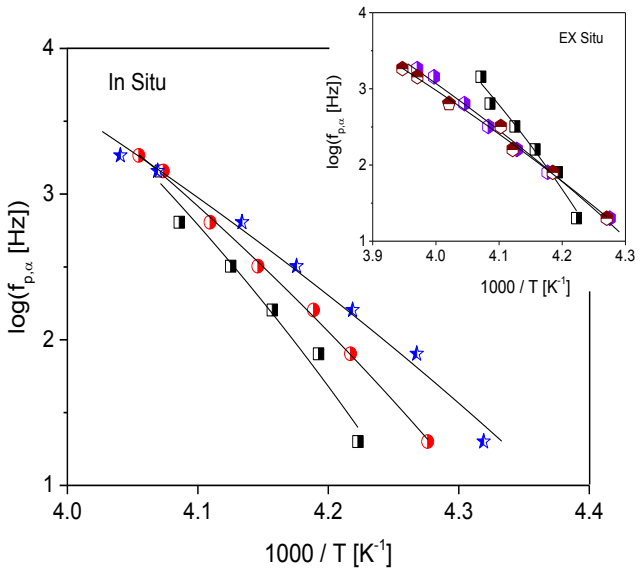

Figure 5.6: Relaxation rate versus inverse temperature (relaxation map) as obtained from the AC-chip calorimetry measurements for the HPAE/Ka-DEA samples (in situ) squares – pure HPAE; circles – 2 wt-% Ka-DEA and stars – 10 wt-% Ka-DEA. The solid lines are fits of the VFT equation to the data. The inset shows the relaxation map the AC-chip calorimetry measurements for the HPAE/Ka-DCA samples (ex situ): squares – pure HPAE; pentagons – 5 wt-% Ka-DCA; diamonds – 10 wt-% Ka-DCA. Lines are fits of the VFT equation to the data.

5.2. Dielectric spectroscopy

Practically, the dielectric behavior of HBPs is characterized by high conductivity contributions, close and above the thermal glass transition. Therefore, the segmental motion related to the glass transition (α-relaxation) is difficult to be detected by dielectric spectroscopy. In these cases, it is useful to present the dielectric spectra by the complex electric modulus M*(Eq.3.6) or/and complex conductivity σ*(Eq. 3.5).

The electric loss modulus M′′of pure HPAE versus frequency and temperature (3D representation) is shown in Figure 5.7. In the modulus representation, a conductivity contribution is converted into a peak [24]. Several dielectric active processes can be observed as peaks in the modulus representation. At low temperatures (high frequencies) a γ-relaxation is observed. The γ-relaxation is followed by the β-relaxation with increasing temperature. At even higher temperatures (lower frequencies) the conductivity contribution is observed as a peak. This conductivity peak broadens for higher temperatures due to the underlying α-relaxation. The β-relaxation cannot be analyzed unambiguously, because it is strongly covered by the γ-relaxation and the conductivity. In the following: first, the γ-relaxation is analyzed in the permittivity presentation and then the conductivity is discussed in detail.

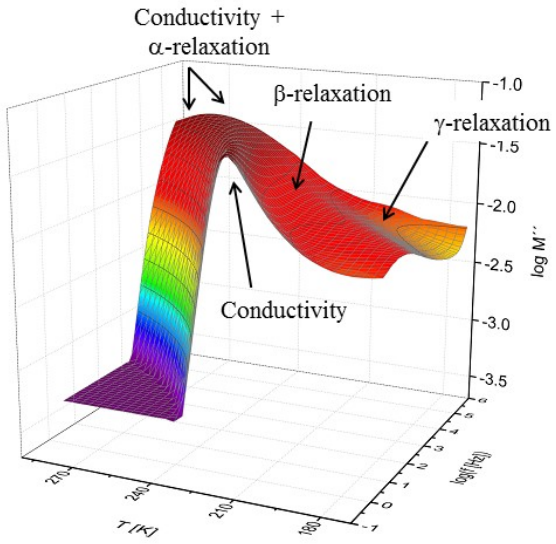

Figure 5.7: Imaginary part of the complex electric modulus of pure HPAE versus frequency and temperature in a 3D representation.

γ-relaxation: Figure 5.8 gives the dielectric loss for pure HPAE and its nanocomposites with Ka-DEA (in situ) at T=173 K. The γ-relaxation is characterized by a broad peak in the dielectric loss. From a molecular point of view, the γ-relaxation is attributed to localized fluctuations of methyl and/or hydroxyl group rotation. These fluctuations could be coupled and/or also affected by both intra- and intermolecular hydrogen bonding, which are formed in these hyperbranched systems. For HPAE nanocomposites with 2 and 10 wt-% of Ka-DEA, the γ-relaxation broadens (see Figure 5.8). Assuming that the spectral shape of the γ-relaxation can be described by relaxation time spectra, one may conclude that the underlying molecular fluctuations become more heterogeneous in the nanocomposites. This is due to the polymer groups, which are in interaction with the nanoparticles and the segments, which have no interaction with the filler.

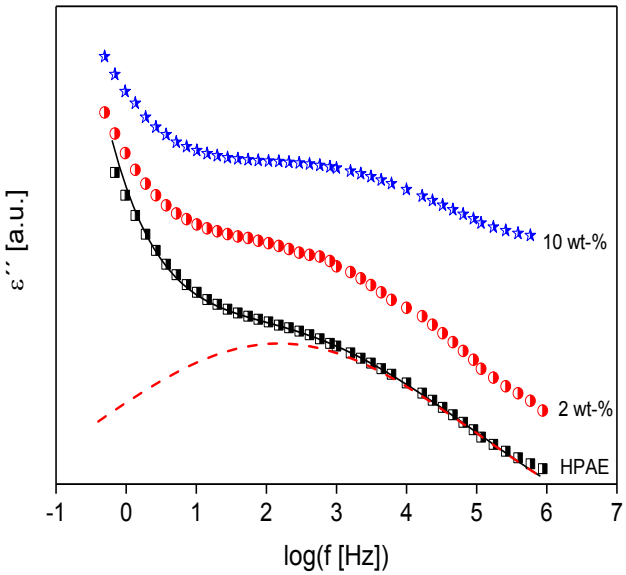

Figure 5.8: Dielectric loss ε´´ versus frequency for the HPAE/Ka-DEA samples (in situ) at T=173 K: squares – pure HPAE; circles – 2 wt-% Ka-DEA; stars – 10 wt-% Ka-DEA. The solid line is a fit of the HN-function to the data of pure HPAE including a conductivity contribution. The dashed line indicates the contribution of the relaxation process.

To analyze this relaxation process, the empirical Havriliak–Negami (HN) function [134] (Eq 3.25) was fitted to the data. From the fit of the HN-function the relaxation rate f_p, is obtained [24]. Figure 5.9 represents the temperature dependence of the

relaxation rate $f_{p,\gamma}$, for γ-relaxation in the relaxation map for the HPAE/Ka-DEA nanocomposites (in situ). Its temperature dependence can be described by an Arrhenius relation (see section 2.5).

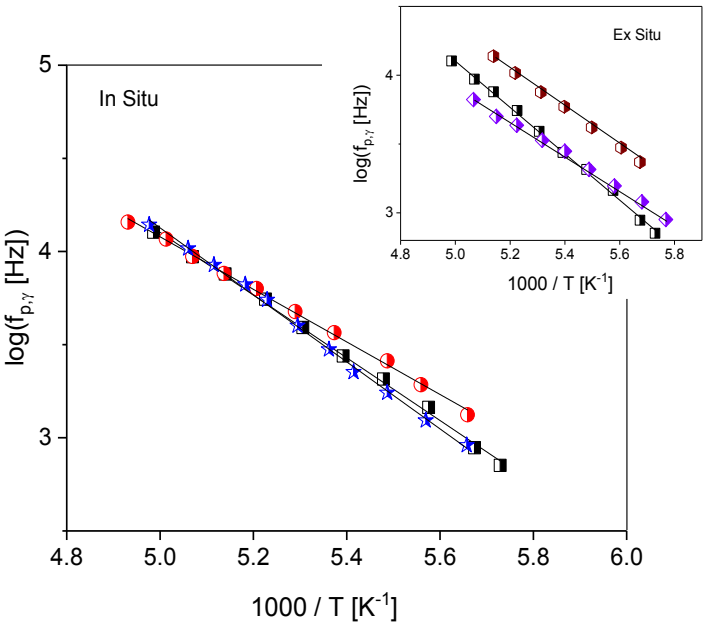

Figure 5.9: Relaxation map obtained from dielectric spectroscopy for the HPAE/Ka-DEA samples (in situ) squares – pure HPAE; circles – 2 wt-% Ka-DEA and stars – 10 wt-% Ka-DEA. The solid lines are fits of the Arrhenius equation to the data. The inset shows the relaxation map obtained from dielectric spectroscopy for the HPAE/Ka-DCA samples (ex situ): squares – pure HPAE; pentagons – 5 wt-% Ka-DCA; diamonds – 10 wt-% Ka-DCA. Lines are fits of the Arrhenius equation to the data.

The estimated activation energies, the HPAE/Ka-DEA samples, are more or less similar to that of pure HPAE. This is in agreement with some literature results. According to recent studies on linear polymers, for instance poly(ethylene oxide), confined within the galleries of layered silicates, the γ-relaxation was not affected by the confinement [171]. Moreover, quasielastic neutron scattering measurements on the hyperbranched poly(ester − amide) Hybrane® showed that the γ-relaxation exhibited similar behavior in the pure polymer and under confinement [31].

Recently, the confinement effect of layered MMT on the dynamics of three different generations of hyperbranched polyesters has been investigated by the BDS

[172]. The results showed that the γ-relaxation is significantly faster and with a lower activation energy than those of the pure polymer. This effect was identical for the three generations. Here a similar behavior was observed for the samples prepared by the ex situ method (HPAE/Ka-DCA) (see the inset Figure 5.9). In difference to the HPAE/Ka-DEA (in situ) nanocomposites, for the ex situ materials the activation energy decreases in confinement from 30 kJ/mol to 25 kJ/mol. On a molecular level, this could be understood by assuming that the system of hydrogen bonding, due to the hydroxyl groups [30,33,172, 173], is changed or partly disrupted for the HPAE/Ka-DCA samples due to the confinement and/or the presence of the nanoparticles. The differences in the structures of both kind of different materials observed by the structural data (SAXS, TEM) is also reflected in its molecular dynamics as revealed by both the γ and the α-relaxation (see Figures 5.6 and 5.9).

Conductivity contribution: The dielectric spectra are dominated conductivity contributions, at temperatures above T_g. Thus, the conductivity formalism (see Eq. 3.5) should be employed to discuss the data. The frequency dependence of real and imaginary part of the complex conductivity σ* for pure HPAE and the nanocomposites is given in Figure 5.10 A,B above T_g at T=257 K. The conductivity spectra show the typical behavior expected for semi-conducting polymeric materials. The real part σ´ decreases with decreasing frequency with a power law down to a characteristic frequency f_c where a plateau value is reached. The plateau value corresponds to the dc conductivity [174-178]. The decrease in the real part of the complex conductivity at even lower frequencies is related to the electrode and/or MWS polarization [24].

To distinguish between conduction and interfacial polarization effects the imaginary part σ´´(f) of the complex conductivity is useful (see Ref. [179] and Figure 5.10B). The frequency corresponding to the minimum in σ''(f) reflects the onset of interfacial polarization. The maximum in the σ''(f) at a lower frequency is related to a fully developed interfacial polarization [179]. For the nanocomposites filled with Ka-DEA (in situ samples), the value of the dc conductivity is more or less similar to unfilled HPAE (see Figure 5.10A). For the samples prepared by the ex situ method,

the dc conductivity is higher than that for neat HPAE. This is related to the changed (enhanced close to T_g) segmental mobility revealed by specific heat spectroscopy measurements (see inset Figure 5.6) induced by the nanofillers.

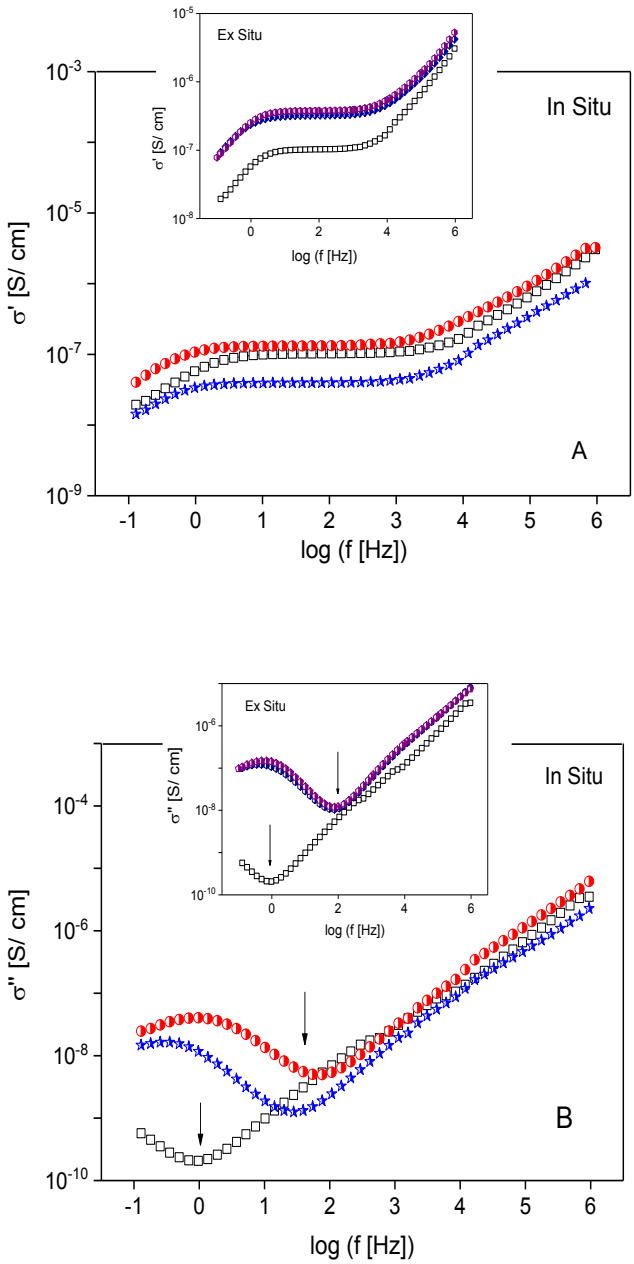

Figure 5.10: Real (A) and imaginary (B) part of the complex conductivity plotted versus frequency at T=257 K, squares – pure HPAE; circles – 2 wt-% Ka-DEA and stars – 10 wt-% Ka-DEA. The insets show the same data for the HPAE/Ka-DCA samples (ex situ): squares – pure HPAE; pentagons – 5 wt-% Ka-DCA; diamonds – 10 wt-% Ka-DCA.

Figure 5.10B provides further that for all nanocomposites the onset of interfacial takes place at higher frequencies. This fact is indicated by the shift of the minimum in the imaginary part σ´´ of the complex conductivity to higher frequencies (see Figure 5.10B). This enhanced interfacial polarization is related to MWS processes where the charge carriers were blocked at the nanofillers.

To describe the frequency dependence of the real part of the complex conductivity, several models were introduced like Dyre model. With this concept, the conductivity is considered in the frame of hopping processes in a random free energy approach [138]. In a simplified way, the real part of complex conductivity function can be approximated by the well-known Jonscher power law (see Eq. 3.29) [139].

Figure 5.11A gives the dc conductivity σ_{dc} as a function of inverse temperature for the different nanocomposites. At first glance, the non-Arrhenius temperature dependency of the dc conductivity relaxation reflects a certain coupling between the motion of the charge carriers and the fluctuations of the polymer segments yielding to glassy dynamics [180]. Like the relaxation rate of glassy dynamics, it can also be described by the VFT equation [120-122]

$$log\sigma_{dc} = log\sigma_{\infty} - \left(\frac{A}{T - T_0}\right) \tag{5.1}$$

where σ_{∞} is the conductivity at infinite temperatures. It is obvious that, for both the HPAE/Ka-DEA and the HPAE-DCA nanocomposites, the temperature dependence of σ_{dc} varies in a similar manner as the relaxation rates estimated from specific heat spectroscopy (compare Figure 5.6 and 5.11A).

For a further detailed analysis of the temperature dependence of the dc conductivity, a derivative method is applied [24]. This method is sensitive to the functional form of $\sigma_{dc}(T)$ irrespective of the prefactor. For a dependency, according to the VFT-equation one gets

$$\left[\frac{d\,(log\sigma_{dc})}{dT}\right]^{-1/2} = A^{-1/2}(T - T_0). \tag{5.2}$$

Therefore in a plot [d (log σ_{dc})/dT]$^{-1/2}$ versus T a VFT-behavior shows up as a straight line (see Figure 5.11B). All experimental data can be well described by straight lines, which proofs that the temperature dependence of the relaxation rates of both processes is VFT-like. A Vogel temperature T_0 for the conductivity can be estimated from both fits of the VFT equation to the corresponding data and by the derivative technique (see Table 5.2). The estimated T_0 values for dc conductivity estimated by the direct fit of the VFT-equation to the data and by the derivative technique are similar in the frame of the experimental error.

Table 5.2: VFT parameters, fragility parameter D_f estimated from the conductivity and decoupling index log (R_τ) estimated from the conductivity of pure HPAE and its nanocomposites.

	Sample	log (σ_∞ [S/cm])	A [K]	T_0 [K]	$T_{0(div)}$ [K]	D_f	log (R_τ)
HPAE	0 wt-%	1.93	1130	137	136	8.2	2.6
In situ	2 wt-%	1.4	1004	143	149	7.1	2.5
	10 wt-%	-0.33	736	163	154	4.5	2.1
Ex situ	5 wt-%	2.67	1185	143	141	8.5	2.1
	10 wt-%	1.26	975	148	143	6.6	3.5

By the comparison between Table 5.1 and 5.2; for pure HPAE, the T_0 estimated from the dc conductivity is significantly lower than the value obtained from the SHS. This is also reflected by quite different values of the fragility parameters (D_f=A/T_0, see section 3.1.5). This result emphasizes a certain decoupling of the temperature dependence of the segmental dynamics and the conductivity. A corresponding behavior was also reported for other HBPs [26,30] and more general for polyelectrolytes [181,182].

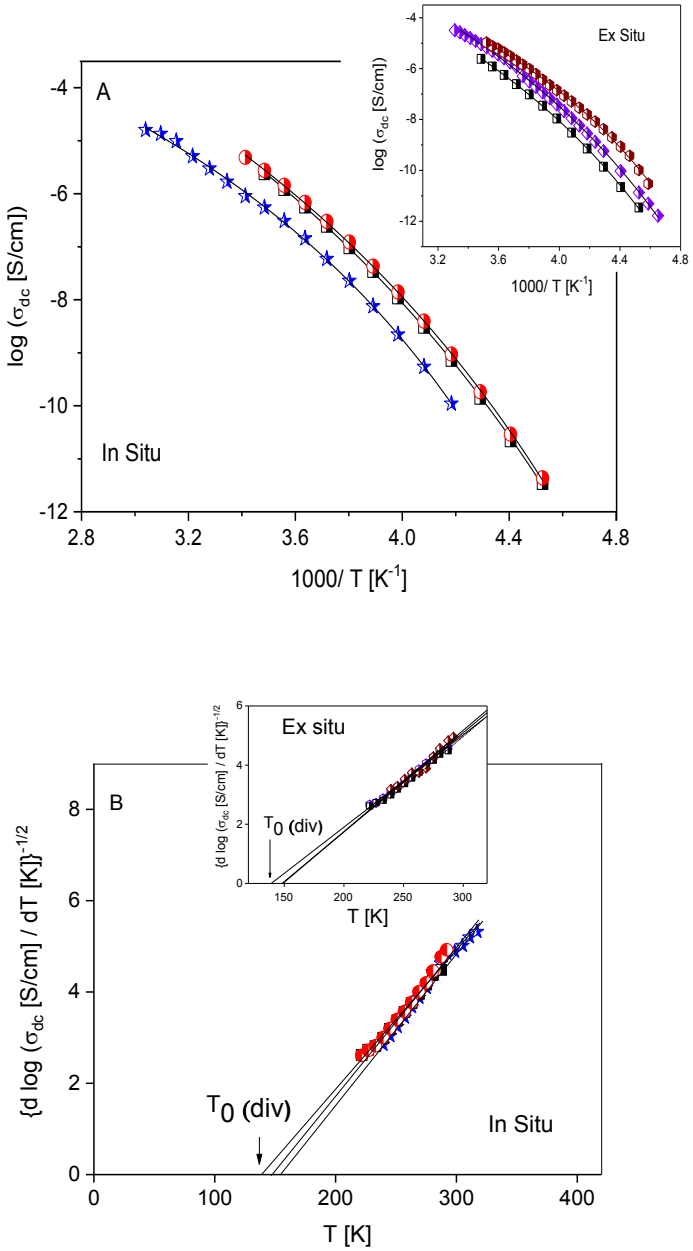

Figure 5.11: (A): dc conductivity σ_{dc} plotted versus 1000/T for the HPAE/Ka-DEA samples (in situ): squares – pure HPAE; circles – 2 wt-% Ka-DEA and stars – 10 wt-% Ka-DEA. Lines are fits of the VFT equation to the data. The inset shows the temperature dependence of σ_{dc} for the HPAE/Ka-DCA samples (ex situ): squares – pure HPAE; pentagons – 5 wt-% Ka-DCA; diamonds – 10 wt-% Ka-DCA. Lines are fits of the VFT equation to the data. (B): $[d(\log \sigma_{dc})/dT]^{-1/2}$ versus temperature for the HPAE/Ka-DEA samples (in situ). The inset shows $[d(\log \sigma_{dc})/dT]^{-1/2}$ versus temperature for the HPAE/Ka-DCA samples (ex situ). The symbols are similar than in part A Lines are linear regressions to the corresponding data.

There are two assumptions to explain the differences in the Vogel temperatures found for segmental and conductivity. First, it is known since a long time that the temperature dependence of the relaxation time of segmental and chain dynamics follow different VFT laws although theoretical treatments predict the same temperature dependence with an identical Vogel temperature [183 - 187]. Such behavior can be understood within the frame work of the coupling model of Ngai [188]. Recently, Sokolov and Schweitzer [189] discussed a decoupling index, where it is defined and related to fragility of segmental dynamics. From a general point of view, this decoupling seems to be related to the heterogeneity of glassy dynamics. The above considerations also apply for conductivity which is like chain dynamics a large-scale motion.

Second, concerning the conductivity its self, Angel [141,142,190] introduced a decoupling index R_τ. It is defined as the ratio of the structural (segmental) relaxation time to the conductivity relaxation time. The decoupling index expresses how much faster the motion of the charge carriers is as expected from the segmental dynamics (α-relaxation). Empirically it is given by $\log (R_\tau)=14.3 + \log(\sigma_{dc}(T_g))$. The estimated VFT parameters for conductivity are used to extrapolate σ_{dc} at the measured glass transition temperatures by DSC. Decoupling indices between 2 and 3.5 are estimated for pure HPAE and the different composites (see Table 5.2). This means that for the systems considered here the charge carriers are 2 to 3.5 orders of magnitude more mobile than expected from the segmental dynamics. Such high values of the decoupling index might be due to proton conduction. In the existence of traces of water the carboxyl group is able to abstract a proton [191], which will lead to protonic conduction in these systems. A similar conduction mechanism was discussed for a different set of HBPs [26,30,38].

It is worth to note that with increasing concentration of the nanofiller, the difference between the Vogel temperatures of segmental dynamics and conductivity becomes smaller. This observation is in agreement with experimental results found for polyelectrolytes where this decoupling also becomes weaker with decreasing fragility of the segmental dynamics (see Table 5.1). The decoupling phenomenon and the influence of the nanofiller will be further studied and verified in the following chapter but for the second set of the HPAMAM.

The Barton-Nakajima-Namikawa (BNN) relationship [135-137] gives the relation between the critical frequency f_c and the dc conductivity by $\sigma_{dc} \sim f_c$ (see section 3.1.5). In Figure 5.12, the dc conductivity σ_{dc} is plotted versus the critical frequency f_c (see Eq. 3.29), which characterizes the onset of the dispersion at the charge transport. The data for pure HPAE as well as for all the composites follows a linear dependence and collapse into one chart. This is an expression of the empirical BNN relationship, which is also fulfilled for the samples studied here independently of the structure of the prepared nanocomposite.

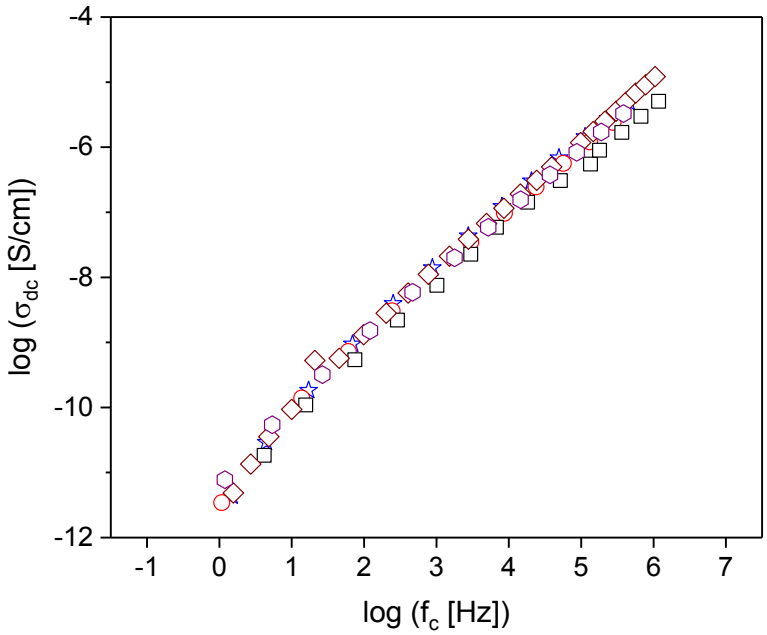

Figure 5.12: Polt of dc conductivity σ_{dc} versus the characteristic frequency f_C for pure HPAE and all nanocomposites: squares – pure HPAE; circles – 2 wt-% Ka-DEA and stars – 10 wt-% Ka-DEA; pentagons – 5 wt-% Ka-DCA; diamonds – 10 wt-% Ka-DCA. The solid line is a linear regression using all data points.

6. HPAMAM/KA NANOCOMPOSITES: STRUCTURE AND CHARGE CARRIER DYNAMICS

ABSTRACT: Hyperbranched poly(amidoamine)/ kaolinite (HPAMAM/Ka) nanocomposites were prepared via an ex-situ approach. During this method, the Ka-DCA was used as a nanofiller. The structure of the polymer and the corresponding nanocomposites were investigated by DSC, FTIR, SAXS and TEM. DSC revealed a decrease in glass transition temperature with increasing Ka-DCA content. A partly exfoliated structure of the nanocomposites was indicated by SAXS and confirmed by the disappearance of the rod-like structure of pure Ka-DCA observed by TEM. The molecular dynamics was studied in a wide frequency and temperature range by means of broadband dielectric spectroscopy (BDS). The dielectric spectra were dominated by the conductivity contribution at higher temperatures (overlapping the α-relaxation process), for all samples investigated. Specific heat spectroscopy (SHS) was used to detect the segmental dynamics. The obtained results further indicated that dc conductivity is increased by 4 orders of magnitude with increasing concentration of the Ka-DCA. Further, a significant separation between the conductivity relaxation time τ_σ and that of segmental dynamics τ_α was observed. The decoupling phenomenon, fragility as well as the conductivity mechanism were discussed in detail. For deeply understanding of the relationships between structure, morphology, and charge transport properties of nanocomposites based on HBPs, two different concentrations of the HPAMAM/Ka-EDA nanocomposites were prepared via an in situ polymerization. For sake of clarity, the in situ prepared samples will be discussed in the second part of this Chapter.

6.1. Ex situ prepared samples*

6.1.1. Characterization of HPAMAM/Ka nanocomposites

Figure 6.1 represents the SAXS measurements of the prepared nanocomposites. The diffraction peaks for 5, 10 and 20 wt-% of HPAMAM/Ka-DCA nanocomposites were observed at quite similar positions than the Bragg pattern characteristic for Ka-

* Similar content was presented in: Omara, S. S.; Turky, G.; Ghoneim, A.; Thünemann, A. F.; Rehim, M. H. A.; Schönhals, A.: Polymer. 121, 64-74, (2017).

DCA (d=3.6 nm). This results points to partly exfoliated objects together with ordered or stack-like structures of the nanofiller in the matrices. By fitting a Gaussian to the data, the width w of the peak is estimated. For Ka-DCA, the peak width *w* is to 0.0178 nm^{-1} and the correlation length was calculated to $I_C=2\pi/w$=354 nm. From the correlation length, the number of layers in stack is calculated to I_C/d=98. For prepared nanocomposites, the effective numbers of layers are 88, 86 and 93 for 5, 10 and 20 wt-% of Ka-DCA. The number of layers in nanocomposites is slightly smaller than that of Ka-DCA. This result confirms a partly exfoliated structure with mixed nano-stacks of the filler. These findings are in agreement with the TEM investigations (see Figure 6.2) where all nanocomposites show a partly exfoliated structure. Further, small stacks or layers of the nanofillers are dispersed in the matrix and the characteristic rod-like structure of pure Ka-DCA disappeared for the nanocomposites due to the interaction of the filler with the polymer (Figure 4.2A). Similar TEM pictures were reported for poly(vinyl chloride) (PVC)/ kaolinite nanocomposites, which have been prepared by a solution intercalation method. In that case, a homogeneous dispersion of the fully exfoliated Ka layers in the PVC matrix, was confirmed by the disappearance of a characteristic peak of the Ka, as revealed by X-ray diffraction [110].

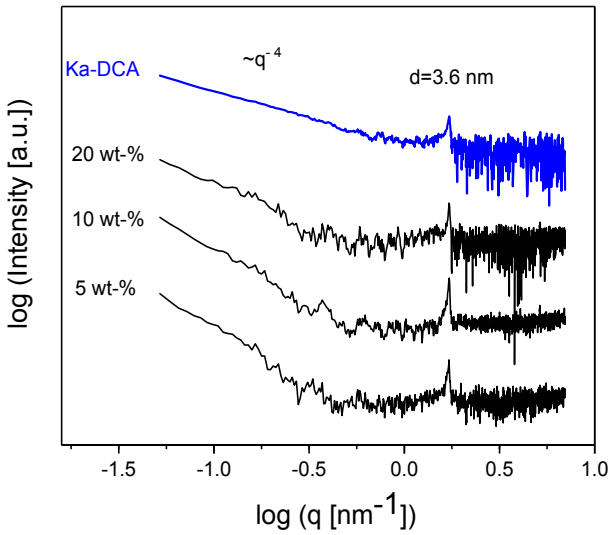

Figure 6.1: SAXS pattern of HPAMAM/Ka-DCA nanocomposites for Ka-DCA, 5, 10, and 20 wt-% of the nanofillers.

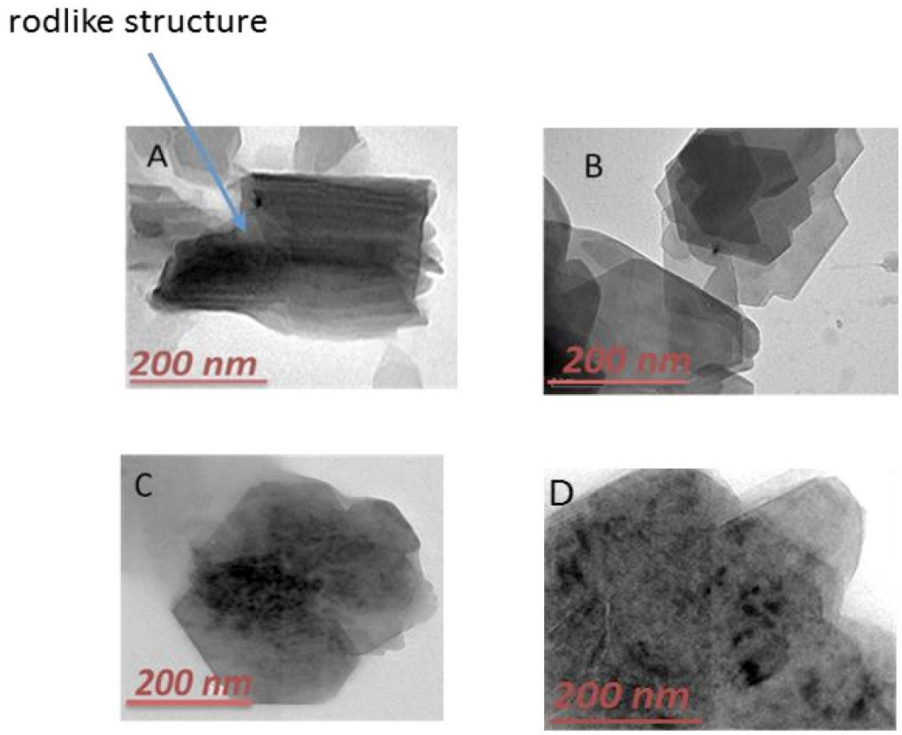

Figure 6.2: TEM pictures for modified kaolinite and the nanocomposites (HPAMAM/Ka–DCA): (A) pure Ka-DCA, (B) 5 wt-%, (C) 10 wt-% and (D) 20 wt-% of the nanofillers. The size bar represents 200 nm.

Figure 6.3A provides the FTIR spectra of pure HPAMAM and its nanocomposites. For the pure polymer, the bands in the range of 3498 to 3335 cm^{-1} corresponds to the asymmetric and symmetric of N-H stretching vibrations of the amide group and amine group. For the amide group, the absorption peak of the carbonyl group is observed at 1653 cm^{-1}. The strong absorption peak at 1569 cm^{-1} corresponds to N-H bending vibration of the amine group [156]. For the nanocomposites, the bands corresponding to the asymmetric and symmetric of N-H stretching vibrations of the amide group are shifted to lower wave numbers in the range of 3396 to 3291 cm^{-1} as result of the interaction of the polymer with Ka-DCA. Additionally, for the HPAMAM/Ka-DCA nanocomposites, the strong characteristic peak for carbonyl group at 1653 cm^{-1} observed for pure HPAMAM is shifted to 1646 cm^{-1}. Moreover, the observation of two weak peaks at 1114 and 728 cm^{-1} assigned to the Si-O and the Al-OH vibrations, respectively are referred to the existence of pure Ka and/or Ka-CA. However, it can be inferred that some DCA molecules are desorbed from the Ka surface and extend into the layer [192], due to the interaction between polymer and

nanofiller. Further, this interaction can be confirmed by disappearance of rod-like structure of pure Ka-DCA seen in the TEM images. This can be better understood according to a recent study of morphological features of the Ka [193] where it was reported that, in general, an intercalation or exfoliation process leads to change of the Ka morphology. Thus, the natural platy Ka could be changed from nano-plates into nano-rods by intercalation, like in the case of Ka-DCA, and further this regular structure could be deformed by the interaction between the polymer and the nanofiller.

For a more detailed analysis, Gaussians are fitted to the data in the wave number range from 1800 to 1500 cm^{-1}. In detail, the peak of the carbonyl group at 1653 cm^{-1} and the amine at 1569 cm^{-1} are considered. If the contribution of the DCA adsorbed at the kaolinite is neglected, these peaks can be taken as characteristic of the pure polymer. After subtraction of the baseline, the areas of these peaks I_{1653} and I_{1569} at 1653 and 1569 cm^{-1}, is estimated by fitting of two Gaussian simultaneously to the data. The ratio I_{1653}/I_{1569} is plotted versus the concentration of the Ka-DCA nanofiller in Figure 6.3B. The ratio increases linearly with the concentration and can be described by

$$\left(\frac{I_{1653}}{I_{1569}}\right) = 0.04\, x_{conc.\%} + 1.47 \tag{6.1}$$

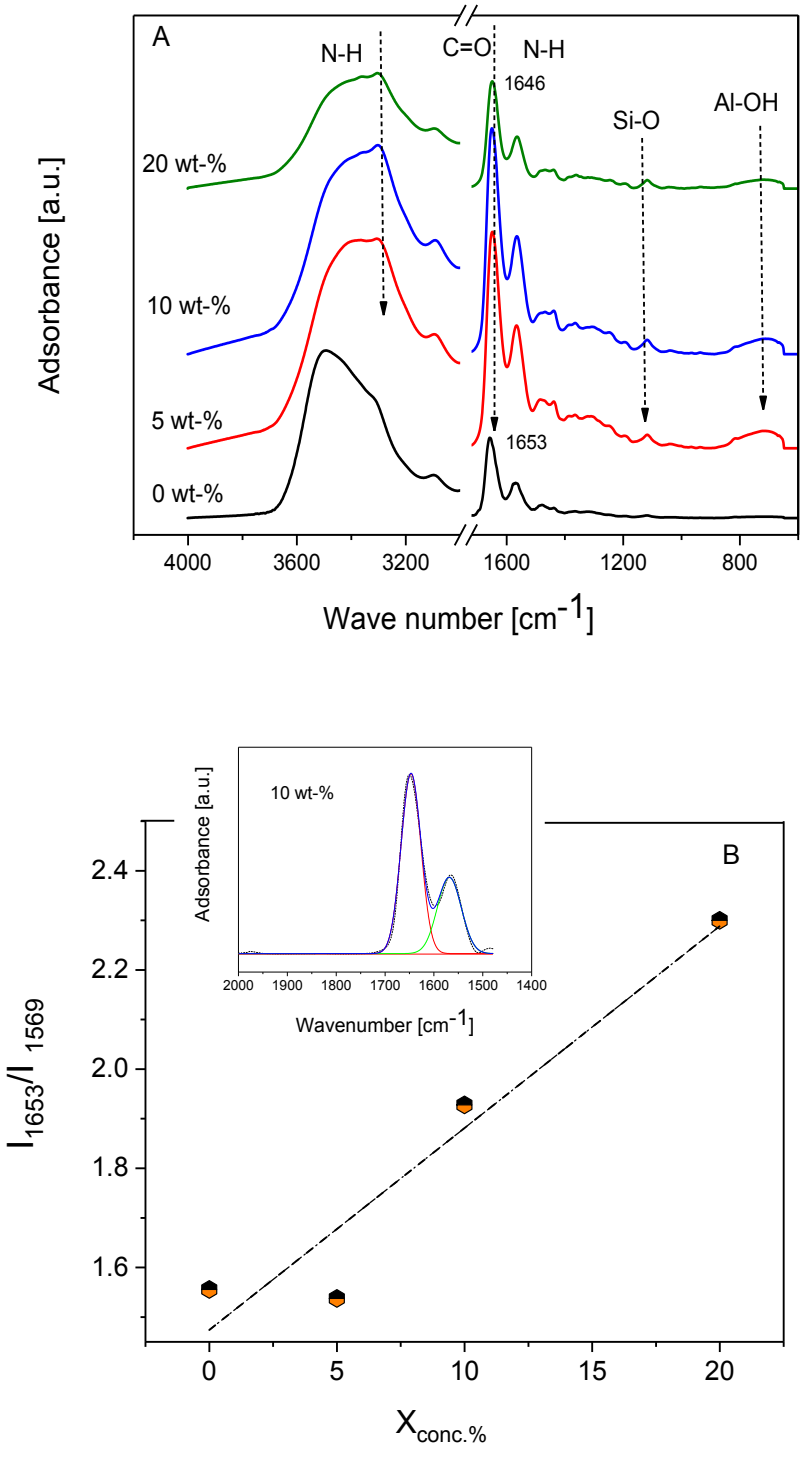

Figure 6.3: (A) FTIR spectra for pure HPAMAM and HPAMAM/Ka-DCA nanocomposites for 5, 10 and 20 wt-% of the nanofiller. For sake of clearness, the curves were shifted along the y-scale. (B) Ratio of the FTIR intensities I_{1653}/I_{1569} vs. the concentration of the nanofiller. The line is a linear regression to the data. The inset is an example for a Gaussian fitting to 10 wt-% of Ka-DCA.

The number of free carbonyl groups increases with regard to the amine units, as it is indicated by the linear relationship. Keeping in mind that the chemical structure of HPAMAM is fixed thus the apparent increase in the number of carbonyl groups with the filler content, must be filler induced due to a change of the hydrogen bonding network. This can be explained as follows: in neat HBP, a part of the carbonyl groups is involved in an inter- und intramolecular hydrogen bonding network. In the case of the nanocomposites, this hydrogen bonding network is partly disrupted by the filler particles. Moreover, the carbonyl groups can also interact with the filler particles instead to be incorporated in the inter- and intramolecular hydrogen bonding network, which would probably lead to more free carbonyl groups compared to the unfilled state. With increasing filler concentration, the interaction possibilities between the polymer and the nanofiller increases. Hence, the linear increase of the ratio I_{1653}/I_{1569} evidences also the interaction between the polymer and Ka-DCA.

Table 6.1: Glass transition temperature T_g (second heating), decoupling indices R_τ and $log(R_1)$, VFT parameters, the fragility parameter (D_f) estimated from the temperature dependence of the rate of the conductivity and the apparent activation energy for the conductivity relaxation for pure HPAMAM and the nanocomposites at temperatures below T_g.

Sample HPAMAM	T_g [K]	log (σ_∞ [S/cm])	A [K]	T_0 [K]	D_f	R_τ	log(R_1)	Ea [kJ/mol]
0 wt-%	241.3	0.27	655.6	187.1	3.5	3.0	2.0	104
5 wt-%	238.7	0.41	745.5	176.8	4.2	2.8	1.8	90.0
10 wt-%	241.1	0.04	667.9	173.4	3.9	2.4	0.9	86.2
20 wt-%	228.3	0.95	860.8	154.2	5.6	2.2	1.0	95.7

Figure 6.4 displays the DSC thermograms in the temperature range of the thermal glass transition of HPAMAM of for the different samples. The estimated T_g values for 5 and 10 wt-% of Ka-DCA seems to be more or less similar to pure HPAMAM. However, a pronounced decrease is observed for 20 wt-% of the nanofiller content (see Table 6.1).

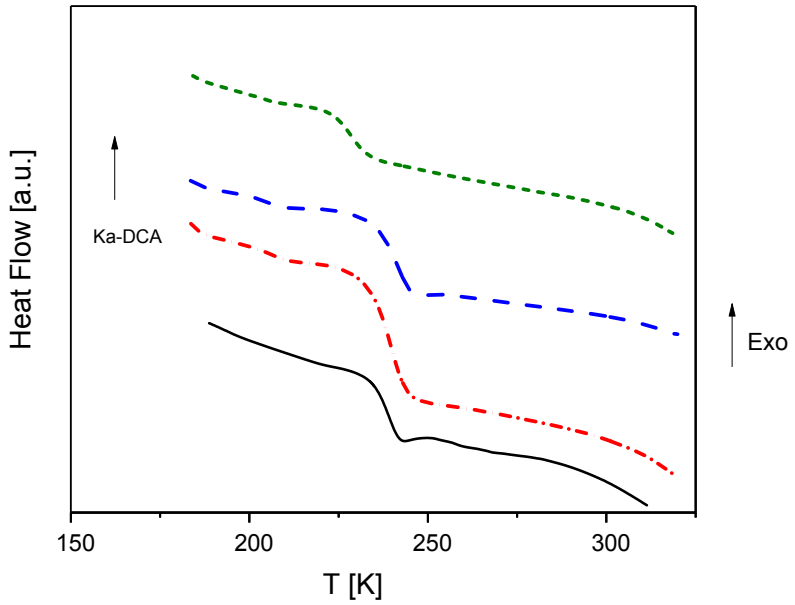

Figure 6.4: DSC thermograms for HPAMAM/ Ka-DCA nanocomposites: solid line – pure HPAMAM, dotted line – 5 wt-%, dashed line – 10 wt-% and short dashed line – 20 wt-% of Ka-DCA. The curves are shifted along the y-scale for sake of clearness.

6.1.2. Dielectric spectroscopy

The molecular dynamics of the samples was investigated by BDS. Figure 6.5 displays the electric loss modulus of pure HPAMAM versus frequency and temperature in a 3D representation, where the complex electric modulus M^* was previously defined (see Eq.3.6) [24].

In the modulus representation, a conductivity contribution to the dielectric spectra appears as a peak [24]. Several dielectric active processes can be detected as peaks. At low temperatures (high frequencies) a γ-relaxation is observed. The γ-relaxation is followed by the β-relaxation with increasing temperature. At even higher temperatures (lower frequencies) the conductivity contribution is observed as a peak. An α-relaxation cannot be detected unambiguously because it is masked by conductivity.

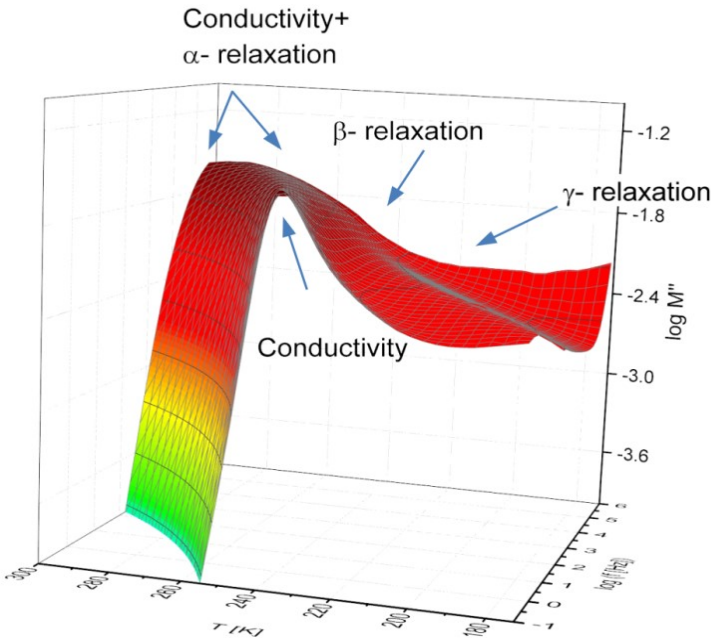

Figure 6.5: Imaginary part of the electric modulus of pure HPAMAM versus frequency and temperature in a 3D representation.

Figure 6.6A depicts the frequency dependence of the real and imaginary part of the complex conductivity (see Eq.3.21), for pure HPAMAM at different temperatures. The conductivity spectra show the typical frequency dependence expected for semiconducting disordered materials. With decreasing frequency, the real part of the complex conductivity σ′ decreases with a power law down to a characteristic frequency f_c where a plateau is attained. The dc conductivity, σ_{dc} can be directly estimated from this plateau [24,140,178]. At even lower frequencies and/or higher temperatures, a further decrease of σ´ with decreasing frequency is observed which is related to electrode and/or MWS polarization effects [24].

The interfacial or electrode polarization can be distinguished from dc conductivity by considering the imaginary part σ´´of the complex conductivity (see Figure 6.6B). The interfacial polarization sets in at the frequency corresponding to the minimum in and is fully developed at the maximum in σ´´ [179]. With increasing the temperature from 239 to 299 K (50 K), the dc conductivity increases by 6 orders of magnitude and the critical frequency f_c shifts to higher frequencies too. A similar

behavior was found for other HBPs [25-27], HBPs/ nanocomposites [31,33] as well as for glasses, and ion-conducting glass-forming liquids [174-177].

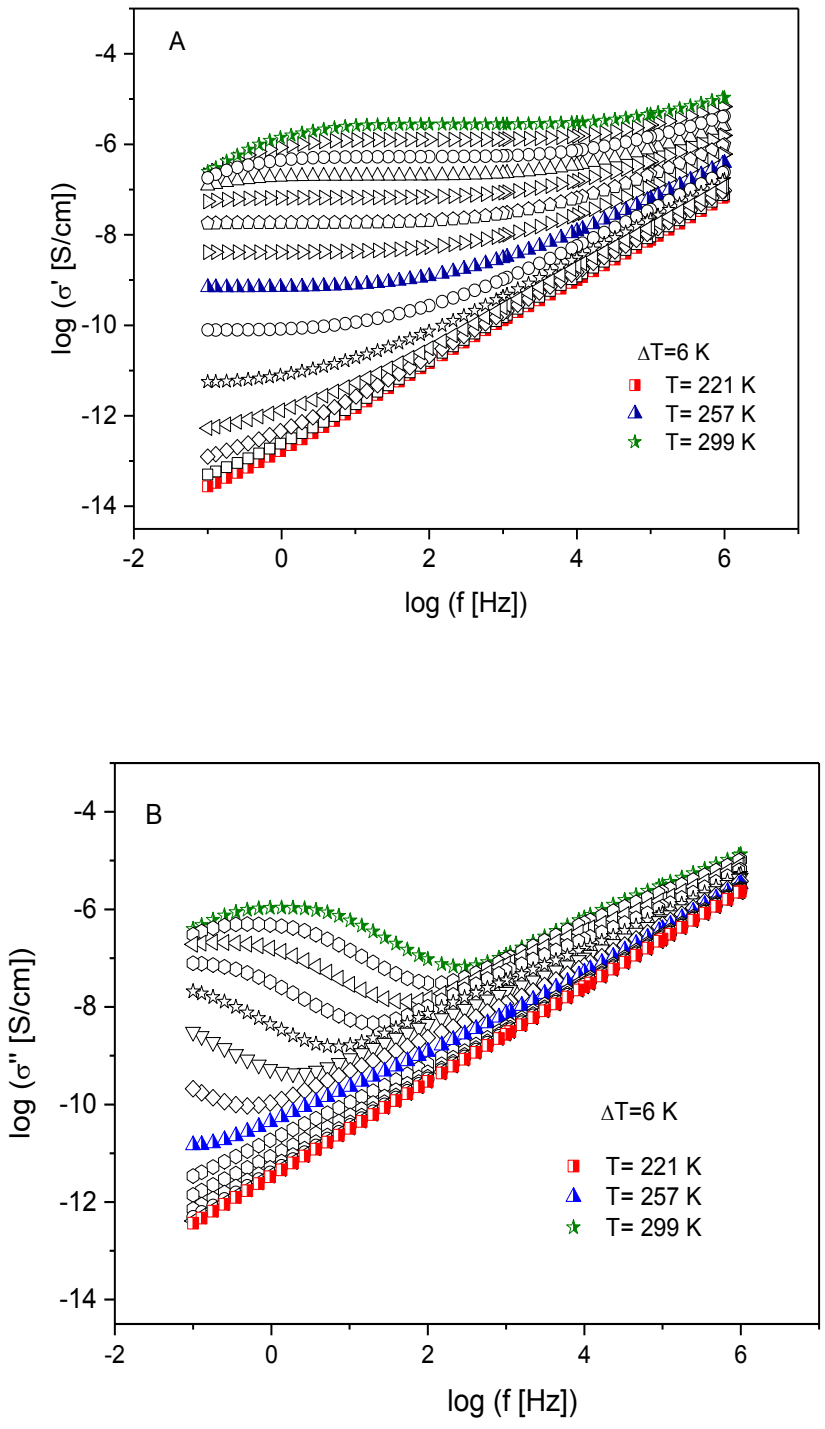

Figure 6.6: Real (A) and imaginary part (B) of the complex conductivity versus frequency at different temperatures for pure HPAMAM as indicated.

Figure 6.7A displays the real part of the complex conductivity σ´ at glass transition temperature for pure HPAMAM and all concentrations of the nanofiller. Obviously, with increasing concentration of the nanofiller, the dc conductivity σ_{dc} increases. The σ_{dc} and the critical frequency f_c can be obtained by fitting the Jonscher equation to the real part of complex conductivity function (see section 3.1 Eq.3.29) [139]. Figure 6.7B depicts the dc conductivity at T = 239 K versus the concentration of the nanofiller where an almost linear increase of σ_{dc} with the concentration is observed.

The dc conductivity for the nanocomposite with 20 wt-% of the nanaofiller is 4 orders of magnitude higher in comparison to that of the pure HPAMAM. This increase of dc conductivity can be discussed as follows: At the one hand, the interactions between the polymer and the basal oxygen plane of Ka is more favorable than that between Ka and DCA, DCA ions can be detached from the Ka sheets and replaced by polymer segments. Thus, the unbounded DCA molecules might contribute as ions to charge transport leading to a higher conductivity compared to the bulk as also discussed in literature [192]. At the other hand, as discussed above due to the interaction of the polymer with the nanofiller, an increased number of free carbonyl groups is present in nanocomposites, which are not involved in the hydrogen bonding network. In the presence of small traces of water, one proton can be abstracted from each carbonyl group. These additional available protons will increase the number density of charge carriers and hence the conductivity. Further, a decrease in T_g with increasing concentration of the nanofiller (see Table 6.1), which is related to accelerated segmental dynamics compared to pure HPAMAM, enhances in parallel the dc conductivity of the polymer. According to these considerations, the increase of the dc conductivity is due to an increase of the number density of charge carriers, related to exfoliated layers, and also to an increase in the segmental mobility.

It is worth mentioning that the dc conductivity is defined as the product of the charge carrier density n and its mobility μ (see Eq.3.30). However, here the temperature dependence of the number density of the charge carriers cannot be

estimated because of the fact that the mobility of the charge carriers cannot be measured independently as it was done in the literature [26].

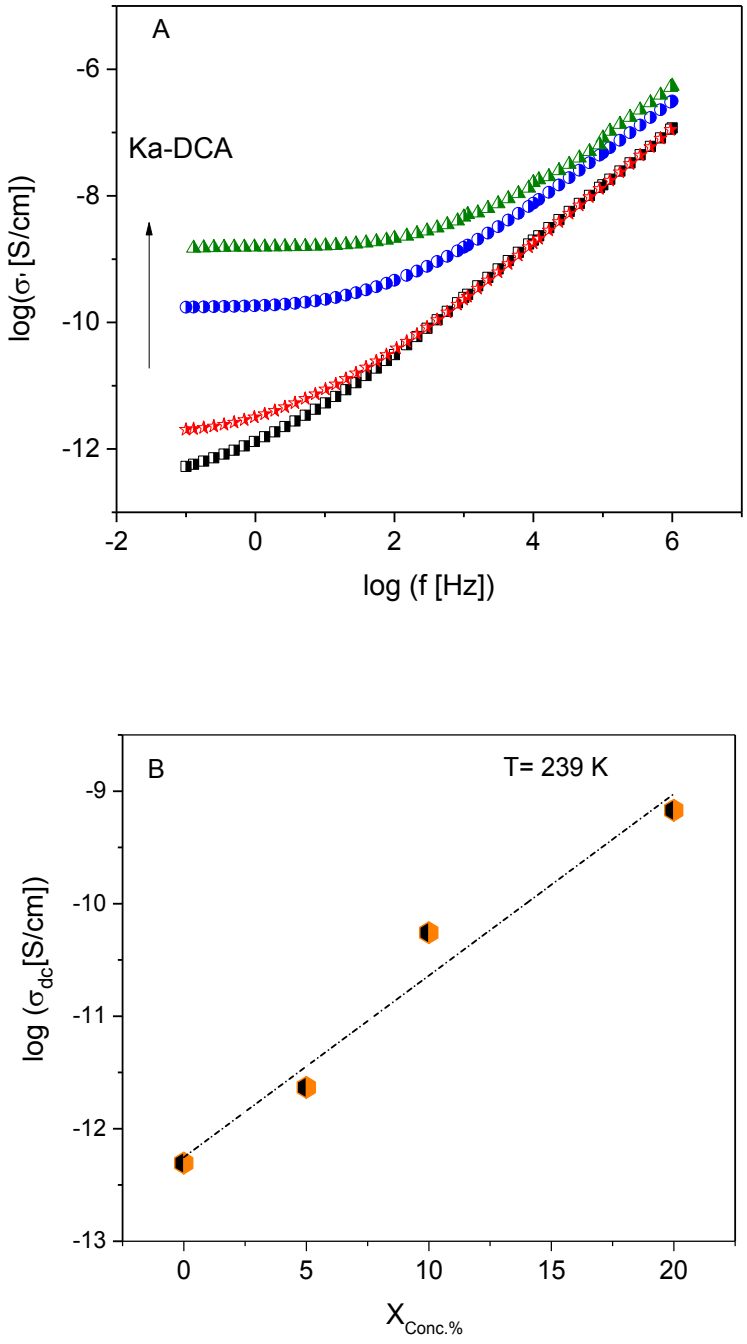

Figure 6.7: (A) Real part of the complex conductivity plotted versus frequency: squares pure HPAMAM; stars -5 wt-%; circles - 10% wt-% and triangles -20 wt-% of Ka–DCA at glass transition temperature for pure HPAMAM and all concentrations of the nanofiller (B) dc conductivity versus the concentration of the nanofiller at T=239 K.

BDS is applied to investigate the degree of decoupling between the segmental dynamics and the conductivity and to discuss the molecular mechanism of charge transport, in terms of ionic and non-ionic processes [194 - 196] in HBPs and HBPs/nanocomposites. Two types of charge transport mechanism have been discussed for these systems. The first one is a so-called vehicle type mechanism [197], where the charge transport (conductivity) is coupled to segmental dynamics (α-relaxation). The second mechanism is called Grotthuss conduction due to hopping of protons through a hydrogen bonding network, such as the proton conductivity of water [198]. This mechanism is not directly related to segmental motion and hence the proton transport decouples from the α-relaxation [199,200].

Figure 6.8 depicts the dc conductivity σ_{dc} as a function of inverse temperature for pure HPAMAM and the different nanocomposites. At high temperatures, above the glass transition temperature, the temperature dependence of the dc conductivity follows the VFT law (see Eq 5.1) [120-122]. The Vogel temperature T_0 for the conductivity and the fragility parameter ($D_f = A/T_0$) can be estimated from a fit of the VFT equation to the data (see Table 6.1). With decreasing temperature, both the segmental dynamics and the motion of charges carriers slow down. For pure HPAMAM in the temperature range around the glass transition temperature T_g the temperature dependence of the dc conductivity changes from a VFT dependence to an Arrhenius-like temperature dependence described by

$$\sigma_{dc} = \sigma_{\infty} \, exp\left(-\frac{E_A}{k_B \, T}\right) \tag{6.2}$$

where k_B is the Boltzmann constant, E_A the apparent activation energy and σ_0 is a pre-exponential factor. The same behavior is also found for the nanocomposites.

However, for the nanocomposites the transition from the VFT to the Arrhenius behavior was observed at temperatures lower than the glass transition temperatures measured by DSC. At temperatures below T_g, in the glassy state the segmental motion is expected to be frozen, but however the migration of charges carriers is still possible as observed as a relatively high conductivity. These results show the appearance of *a decoupling phenomenon* between the segmental dynamics and

charge transport. Further, it has been reported [141,142, 201] that the dc conductivity could be higher than 10^{-15} S/cm at the T_g, if decoupling between segmental dynamics and conductivity is observed. Thus, the point to notice is that for all samples investigated here around their T_gs, the conductivity is much higher than 10^{-15} S/cm (Figure 6.7), confirming that the decoupling phenomena are found in pure HPAMAM and its nanocomposites. A similar effect was also observed for the protonic ionic liquid CKN [202] as well as in the series of hyperbranched polyesters [38].

Although due to time reasons, the Arrhenius-like temperature dependence can be observed only in the narrow temperature range, the apparent activation energies of proton conductivity were estimated (Table 6.1). It is worth mentioning that the activation energies decrease with increasing the concentration of the nanofillers by trend. One explanation for this behavior might be that the system of hydrogen bonding, due to the hydroxyl groups [38,173,173], is changed or partly interrupted for nanocomposites. These distortions of the hydrogen bonding network might lower the energy barriers for proton conduction. With increasing concentration of the nanofiller, the disruption of the hydrogen bonding network becomes more pronounced. Thus, the apparent activation energy of charge transport decreases with increasing concentration of the nanofiller.

The inset of Figure 6.8 shows the dc conductivity σ_{dc} as a function of the critical frequency f_c (BNN relationship, see section 3.1.5) for all samples. The BNN relation [135-137] holds for pure HPAMAM as well as for all the nanocomposites. Moreover, all data collapse into one chart. This indicates that the mechanism of charge transport is similar for all considered nanocomposites.

Further, the crossover temperatures marked by the vertical dashed lines for nanocomposites (235.8, 227 and 220 K for 5, 10 and 20 wt-% respectively) are lower than the glass transition temperature measured by DSC and decreases with increasing filler concentration.

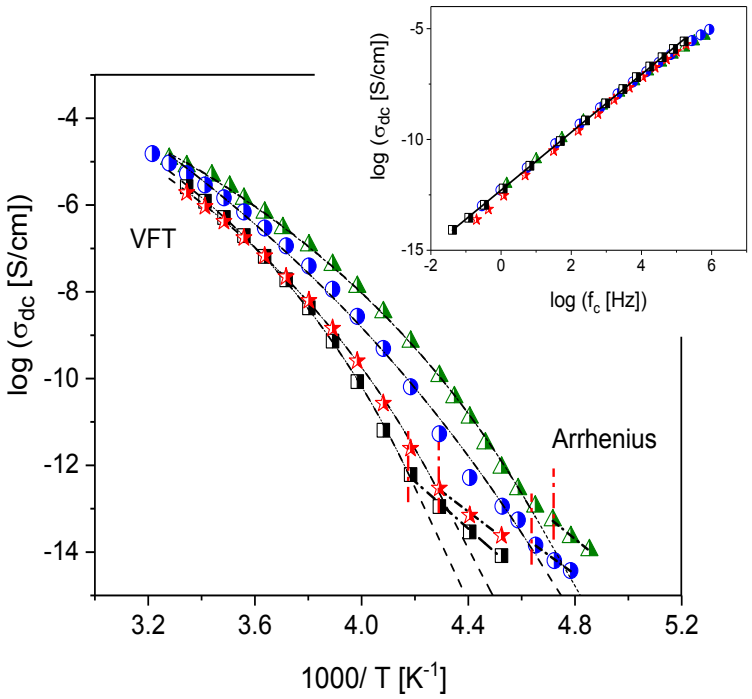

Figure 6.8: dc conductivity σ_{dc} versus 1000/T for the HPAMAM/Ka-DCA samples: squares - pure HPAMAM, stars - 5, circles– 10, and triangles – 20 wt-% of Ka-DCA nanofillers. Dashed lines are fits of the VFT equation to the data for temperatures above T_g. Dashed-dotted lines are fits of the Arrhenius equation at temperatures below T_g. The inset gives the dc conductivity versus the characteristic frequency, f_c (BNN plot) for pure HPAMAM and the nanocomposites. The symbols have the same meaning than in the main figure. The solid line is a linear regression using all data points.

The decoupling index R_τ was introduced to characterize the dominating mechanisms of charge transport in an amorphous material. It is defined as the ratio of the structural relaxation time τ_α to the relaxation time of the conductivity τ_σ (see section 3.1.5). The values of R_τ and $\log(R_1)$ are estimated using Eqs. 3.31and 3.32, and given in Table 6.1. The relaxation time of the conductivity ($\log \tau_\sigma$) was obtained by applying the Jonscher power law [139] to the real part of the complex conductivity, as indicated in Figure 6.9. Please note that, for nanocomposites, the decoupling indices were calculated at the crossover temperatures. The relaxation time of the conductivity for pure HPAMAM is ~ 0.11, 0.13, 0.41, and 0.67 s for 5, 10, and 20 wt-% of Ka-DCA nanofiller, respectively. By assuming that a structural relaxation time equals τ_α =100 s at T_g, the relaxation time of the conductivities for all

samples are much shorter than τ_α. This result signifies the existence of decoupling phenomenon in pure HPAMAM and nanocomposites. However, for the pure polymer the characteristic kink in the τ_σ dependence occurs at shorter relaxation times than for the nanocomposites, which increased slightly with increase the Ka-DCA content. This means that the decoupling between conductivity relaxation and structural dynamics depends on the concentration of the nanofiller.

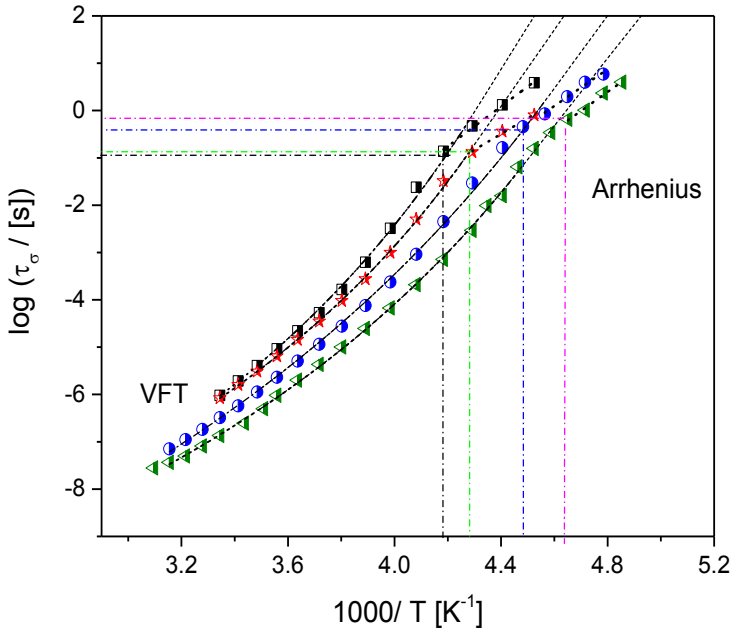

Figure 6.9: Temperature dependence of the relaxation time of conductivity (characteristic rate) τ_σ: squares - pure HPAMAM, stars - 5, circles– 10 and triangles – 20 wt-% of Ka-DCA nanofillers. The log τ_σ dependences are described by the VFT function (above T_g) and Arrhenius law (below T_g).

The values of R_τ and $\log(R_1)$ are given in Table 6.1. They have slightly different absolute values but both decrease with increasing concentration of the nanofiller. Figure 6.10 shows that the decoupling index R_τ decreases approximately linearly with increasing concentration of Ka-DCA. This could be attributed to the exfoliated structure of the nanocomposites, which results in an accelerated segmental dynamics, for higher concentration of Ka-DCA. Further, it is noteworthy to say, that

the decrease of decoupling index values points to the effect of nanofillers in the charge carrier dynamics. With increasing concentrations of the Ka-DCA nanofiller the charge carriers are partly coupled to the segmental dynamics. Nevertheless, the decoupling between segmental dynamics and conductivity is rather noticeable in the nanocomposites.

Moreover, the high value of the decoupling indices evidences a protonic origin of the conductivity. Protons are small particles, which do not require segmental dynamics to be transported. This means that charge transport occurs by hopping via a Grotthuss type mechanism [203] at temperatures below T_g. A similar mechanism of the conductivity was also found for the families of hyperbranched polyesters [38], hyperbranched polyamide amines [26] and hyperbranched polyamine ester [33]. However, there is still a lack of specific investigations on that issues, especially the effect of the nanofillers in decoupling phenomena.

The fragility parameter is employed to classify glass forming systems. In this work, it is used to illustrate the effect of the nanofiller in HBPs on the temperature dependence of the conductivity. In the inset of Figure 6.10, the decoupling index is plotted versus the fragility. The result shows that the sample with higher fragility exhibits a stronger decoupling of the conductivity from segmental dynamics. A similar correlation between the decoupling index and the fragility was also observed for the first set of the HPAE. As was mentioned in Chapter 5, a comparison between the temperature dependence of the dynamic glass transition and that of the dc conductivity displays a decoupling in their dynamic temperature dependencies. Further, this decoupling becomes weaker with decreasing fragility. A similar relation between the decoupling index and the fragility is also found, for some polyelectrolytes [182, 204]. In this regard, it can be concluded that the fragility parameter has an important role on the decoupling phenomena, which is in turn influenced by on the concentrations of the Ka-DCA nanofiller.

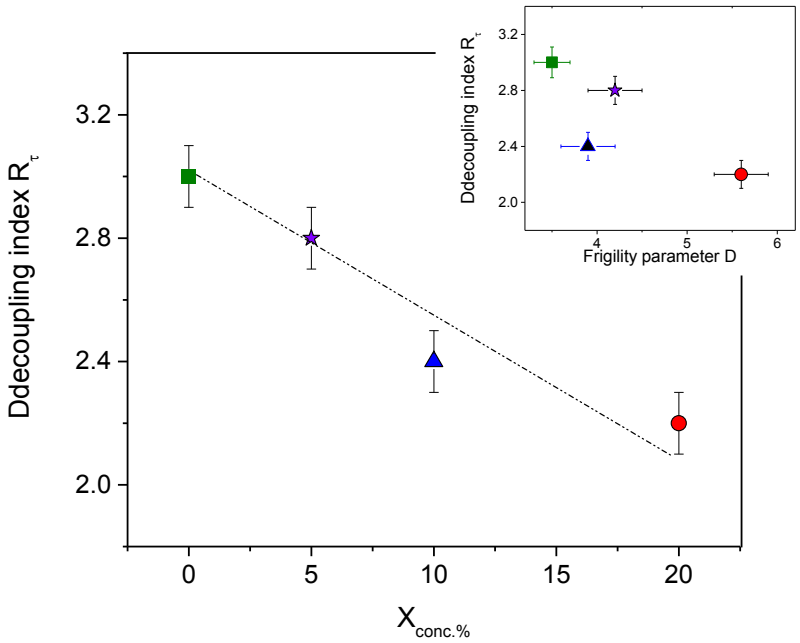

Figure 6.10: The correlation between the decoupling indices R_τ with the concentrations of Ka-DCA nanofillers. The inset shows the correlation between the fragility parameters with the concentrations of the nanofillers. The line is guide to the eyes.

6.2. In situ prepared samples

6.2.1. Characterization of HPAMAM/ Ka-EDA nanocomposites

The morphology of nanocomposites was characterized by SAXS and TEM. Figure 6.11 gives SAXS pattern of HPAMAM/Ka-EDA nanocomposites and the Ka-EDA. The characteristic basal space for for Ka-EDA is d=1.1 nm. Compared to the modified Ka-EDA, no Bragg peak is observed for the nanocomposites. Further, in the low q-range, no scattering intensity is observed, which could be assigned isolated layers (exfoliated morphology). The data follows the Porod law ($I \sim q^{-4}$), indicating the well-defined surfaces. For higher q values, the q -dependence of the scattered intensity is completely flat. Moreover, no Bragg reflections are observed, which are characteristic for the Ka-EDA. The result confirms an exfoliated structure, for HPAMAM/ Ka-EDA nanocomposites. Probably, the interaction between amine groups of the HPAMAM and hydroxyl groups in the Ka-EDA destroys the ordered of the layered structure, causing isolated layers. These findings are in agreement with the TEM investigations (see Figure 6.12).

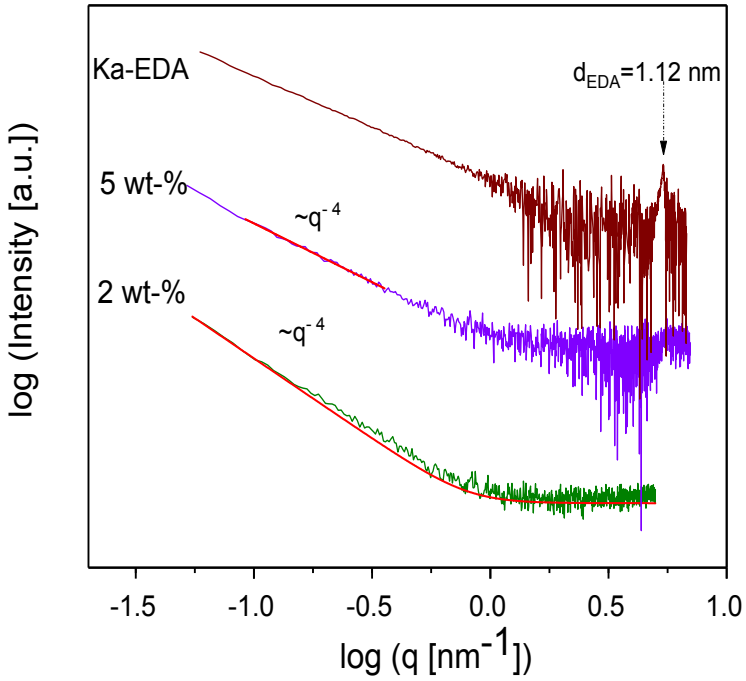

Figure 6.11: SAXS pattern of HPAMAM/Ka-EDA nanocomposites in situ for 2 and 5 wt-% of the nanofiller.

Figure 6.12A shows the morphology of Ka-EDA. It is obvious that hexagonal crystal structure of pure Ka is changed, after the modification by the EDA [110]. Moreover, a regular structure of nano-plates was observed, for the Ka-EDA (see the arrows). This morphological change further confirms the intercalation of EDA between the Ka interlayer spacing. TEM pictures of the nanocomposites (Figure 6.12B, C) show that the Ka-EDA layers are completely dispersed in the HPAMAM matrix. This could be understood by assuming that the polymer is formed between the sheets of Ka-EDA, leading to separate the Ka-EDA layers away from each other such that no Bragg peak can be observed in SAXS investigations (Figure 6.12). Thus, one should conclude that HPAMAM/Ka-EDA nanocomposites have an exfoliated structure.

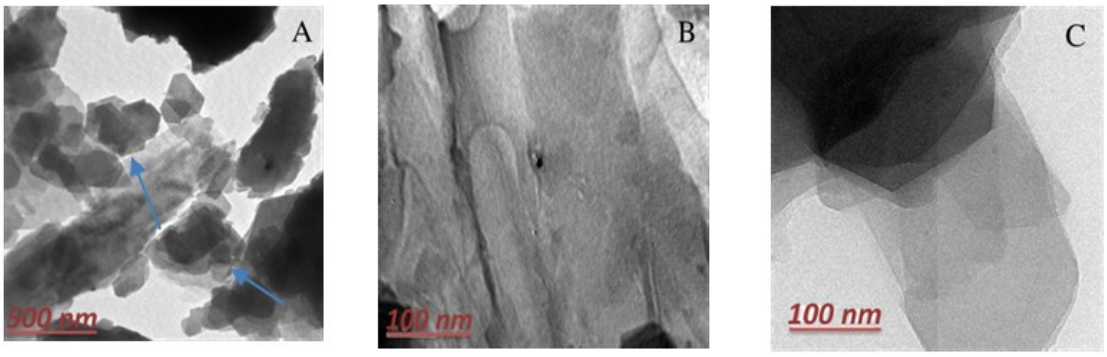

Figure 6.12: TEM pictures for modified kaolinite and the nanocomposites: (A) Ka-EDA, (B) 2 wt-% and (C) 5 wt-% of the filler HPAMAM/Ka–EDA. The size bar represents 100 nm for the nanocomposites and 500 nm for Ka-EDA. The arrows show Ka-EDA layers.

Figure 6.13 shows the FTIR spectra HPAMAM/Ka-EDA nanocomposites. On the one hand, compared to the pure Ka-EDA (see Figure 4.4), the strong absorption peaks at 1653 cm^{-1} and 1647 cm^{-1}, assigned to amide groups [91] in the nanocomposites with 2 and 5 wt-% of Ka-EDA, respectively, suggest that the HPAMAM could be successfully polymerized between the nanofiller layers. This is because of the absorption peaks of the amide groups do not be clearly observed in the FTIR spectrum of the pure Ka-EDA, supporting that the number of carbonyl groups are increased in the nanocomposites. It is worth pointing out that the peak at 1700 cm^{-1}, assigned to the ester groups of MA, is absent, which indicates a full amidation with the EDA [165].

On the other hand, as it was discussed in section 6.1.1, for the pure HPAMAM, the bands in the wave number range from 3498 to 3335 cm^{-1} characterizes the asymmetric and symmetric N-H stretching vibrations of the amide and amine group [156]. For the HPAMAM/Ka-EDA nanocomposites with 2 and 5 wt-% nanofiller, the bands corresponding to the asymmetric and symmetric of N-H stretching vibrations of the amide group are observed, in the wave number range from 3491 to 3348 cm^{-1} and from 3438 to 3288 cm^{-1}, respectively. Thus, compared to the pure HPAMAM, the shift of this characteristic bands to lower wave number refers to a change in hydrogen bonding network, which confirms the interaction between the nanoparticles and the amino groups of the HPAMAM. Moreover, the additional two peaks at 1114 cm^{-1} and 687 cm^{-1}, which are assigned to the Si-O groups and the Al-

OH vibrations, confirming the interaction between the Ka-EDA and HPAMAM. To better understand, referring to Figure 4.4 for the pure Ka-EDA, it is worth mentioning that after intercalation the two peaks at 997 cm^{-1} and 744 cm^{-1} are shifted to the higher wave number at 1114 cm^{-1} and to the lower wave number at 687 cm^{-1}, respectively. This shift further proved the interaction process.

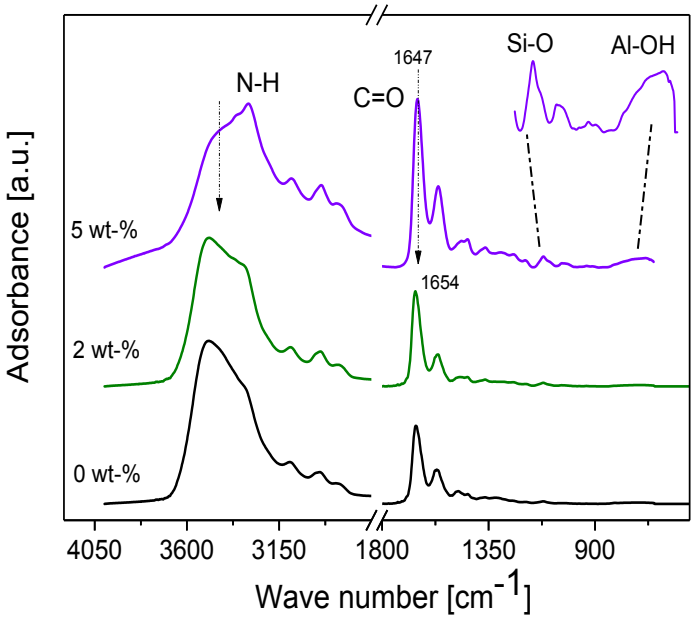

Figure 6.13: FTIR spectra for pure HPAMAM and HPAMAM/Ka-EDA nanocomposites as indicated. For sake of clearness the curves were shifted along the y-scale.

Table 6.2: Glass transition temperature T_g (second heating, 10 K/min.), VFT parameters estimated from SHS and the fragility parameter for the α-relaxation of pure HPAMAM and its nanocomposites. In addition, the activation parameters for the γ-relaxation are given.

Sample HPAMAM	α-relaxation (specific heat spectroscopy)					γ-relaxation	
	T_g [K]	log (f_∞ [Hz])	A [K]	T_0 [K]	D_f	log (f_∞ Hz])	$E_{A,\gamma}$ [kJ/mol]
0 wt-%	241.3	12	1289	146	8.8	13.7	46.6
2 wt-%	232.5	12	1175	153	7.7	9.40	29.0
5 wt-%	227.7	12	1689	106	15.8	8.90	28.0

Figure 6.14 gives the DSC thermograms in the temperature range of the thermal glass transition of HPAMAM/Ka-EDA. The glass transition temperature is determined from the midpoint of the second heating run and given in Table 6.2. Compared to the pure polymer, a pronounced decrease of T_g is observed, for 2 and 5 wt-% of the nanofiller.

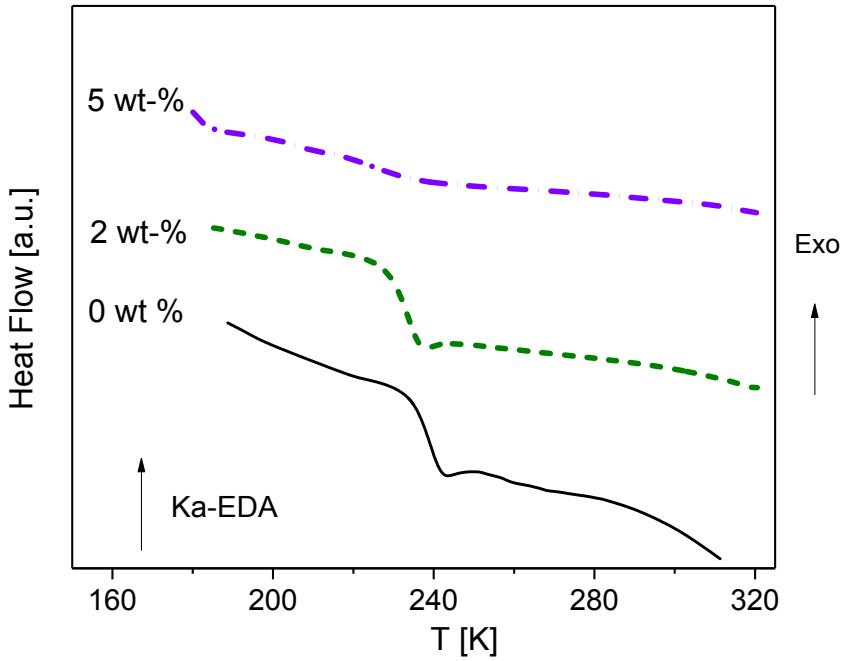

Figure 6.14: DSC thermograms for pure HPAMAM and HPAMAM/ Ka-EDA nanocomposites: solid line– pure HPAMAM, short dashed line – 2 wt-% Ka-EDA and short dashed dotted line– 5 wt-% Ka-EDA (second heating, 10 K/min.). The curves are shifted along the y-scale for sake of clearness.

The glass transition behavior is investigated in more detail by applying specific heat spectroscopy (using AC-chip calorimetry). Figure 6.15 gives the relaxation rate $f_{p,\alpha}$ versus 1/T of pure HPAMAM and nanocomposites. For all samples investigated, the calorimetric data are curved when plotted versus 1/T and can be described by the VFT expression (Eq. 2.3) [120-122]. The data for the HPAMAM/ Ka-EDA with 2 wt-% nanofiller is located in the same temperature region as that of pure HPAMAM. The VFT dependence for the nanocomposite with 5 wt-% nanofiller displays a much

stronger behavior than that of pure HPAMAM and nanocomposites with 2 wt-% Ka-EDA. This is also observed from the calculated fragility parameter (see Table 6.2).

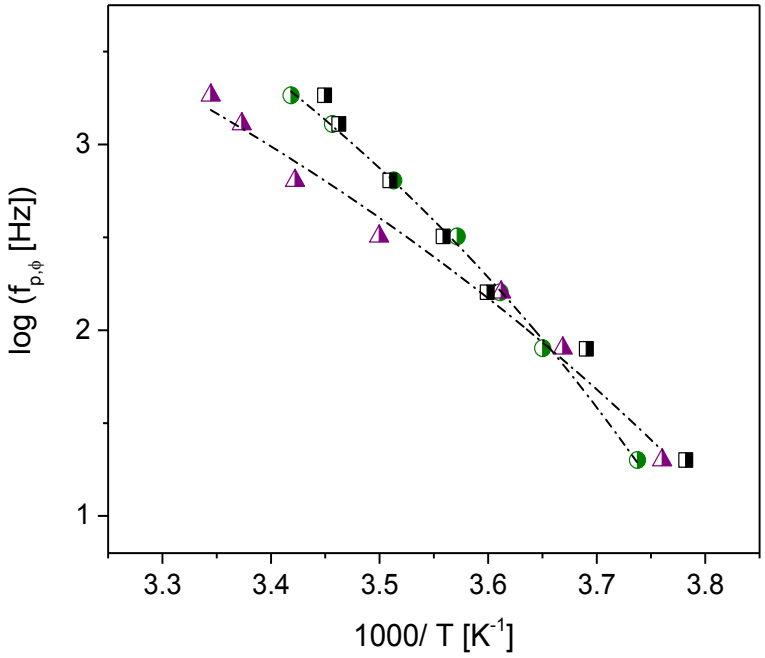

Figure 6.15: Relaxation rate versus inverse temperature as obtained from the AC-chip calorimetry measurements for the HPAMAM/Ka–EDA samples: squares-pure HPAMAM; circles- 2 wt-% Ka–DEA and triangles -5 wt-% Ka–DEA nanofillers. Dashed-dotted lines are fits of the VFT equation to the data.

6.2.2. Dielectric spectroscopy

Figure 6.16A gives the imaginary part of the complex dielectric function ε^* (Eq. 3.3) versus frequency for 2 wt-% Ka-EDA at different temperatures. The sharp increase in the dielectric loss ε'' with decreasing the frequency reflects the dc conductivity and/or the electrode polarization. The γ-relaxation can be observed at temperatures lower than the T_g. It is a broad peak with a broadness approximately 4 decades in the frequency range (see the inset Figure 6.16A), which shifts to higher frequencies as temperature increases. From a molecular point of view, this peak is attributed to localized fluctuations of the methoxy group [26]. These fluctuations could be coupled and/or also affected by both intra- and intermolecular hydrogen

bonding, which are formed in HBPs. A similar behavior was found for all samples investigated. To analyze this relaxation process, the empirical Havriliak–Negami (HN) function was fitted to the data (Eq 3. 25) [134]. From the fit of the HN-function the relaxation rate $f_{p,\gamma}$, is obtained [24].

Figure 6.16B represents the temperature dependence of the relaxation rate $f_{p,\gamma}$, for γ-relaxation in the relaxation map, for pure HPAMAM and nanocomposites. Its temperature dependence can be described by an Arrhenius relation (Eq. 2.4, section 2.5). The temperature dependence of the $f_{p,\gamma}$ for γ-relaxation has much weaker Arrhenius temperature dependence, for nanocomposites 2 and 5 wt-% Ka-EDA. The activation parameters for the γ-relaxation of the samples investigated are given in Table 6.2. For the HPAMAM/ Ka-EDA with 2 and 5 wt-% nanofiller, the γ-relaxation has a lower activation energy (see Table 6.2), compared to pure HPAMAM. On a molecular level, this decrease in the activation energies could be understood by assuming that the interaction between the Ka-EDA and the polymer groups leads to change or partly disrupt the system of hydrogen bonds. Thus, the easier reorientation of the methoxy groups is attributed to the less restricted motion in HPAMAM/ Ka-EDA nanocomposites.

Table 6.3: Decoupling indices R_τ and $\log(R_1)$, VFT parameters, the fragility parameter (D_f) estimated from the temperature dependence of the rate of the conductivity for pure HPAMAM and the nanocomposites.

Sample HPAMAM	log (σ_∞ [S/cm])	A [K]	T_0 [K]	D_f	R_τ	$\log(R_1)$
0 wt-%	0.2700	655	187.0	3.5	3	2.0
2 wt-%	-0.11284	701.5	177.5	4.0	2.5	1.7
5 wt-%	-0.35647	632.8	178.9	3.5	2.1	1.2

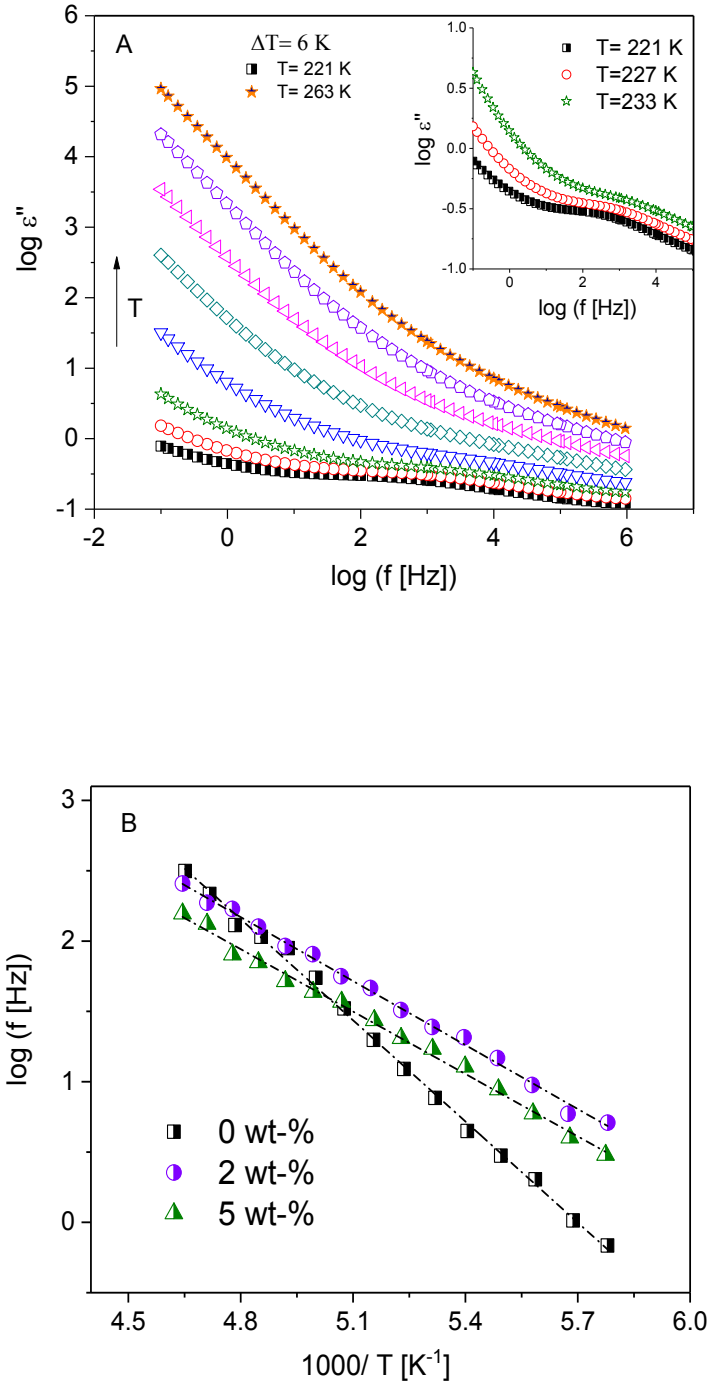

Figure 6.16: (A) Dielectric loss ε´´ plotted versus frequency for different temperatures as indicated, for the nanocomposites of 2 wt-% of Ka-EDA. The inset shows a magnified view of the dielectric loss ε´´ at the different temperatures as indicated. (B) The relaxation map obtained from dielectric spectroscopy for the HPAMAM/Ka-EDA samples: squares-pure HPAMAM; circles- 2 wt-% Ka–EDA and triangles- 5 wt-% Ka–EDA. The dashed lines are fits of the Arrhenius equation to the data.

Figure 6.17A shows the frequency dependence of the real part of the complex conductivity σ' (see Eq.3.5), for 5 wt-% Ka-EDA at different temperatures. As discussed earlier, σ' has a plateau on the low frequency side, which bends off at a characteristic frequency f_c and results for $f \gg f_c$ in a power law dependence of the type $\sigma' \sim f^s$ ($s \leq 1$). The dc conductivity σ_{dc} can be estimated from this plateau (see section 5.2) [24]. Figure 6.17B gives the dc conductivity σ_{dc} as a function of inverse temperature for pure HPAMAM and the nanocomposites. At high temperatures, above the glass transition temperature, the temperature dependence of the dc conductivity follows the VFT law (see Eq 5.1). The Vogel temperature T_0 for the conductivity and the fragility parameter ($D_f = A/T_0$) can be estimated from a fit of the VFT equation to the data (see Table 6.3). The inset of Figure 6.17B shows the dc conductivity σ_{dc} at T=239 K versus the concentration of the Ka-EDA. With increasing concentration of the Ka-EDA, the dc conductivity σ_{dc} increases. Obviously, σ_{dc} for the nanocomposite with 5 wt-% of the Ka-EDA is ~2 orders of magnitude higher compared to pure HAPAMAM. The increase in dc conductivity could be due to an increase in the segmental mobility. This is because of a decrease in the T_g value with increasing concentration of the Ka-EDA (see Table 6.2), which is related to an accelerated segmental dynamics compared to pure HPAMAM, enhances in parallel the dc conductivity of the polymer.

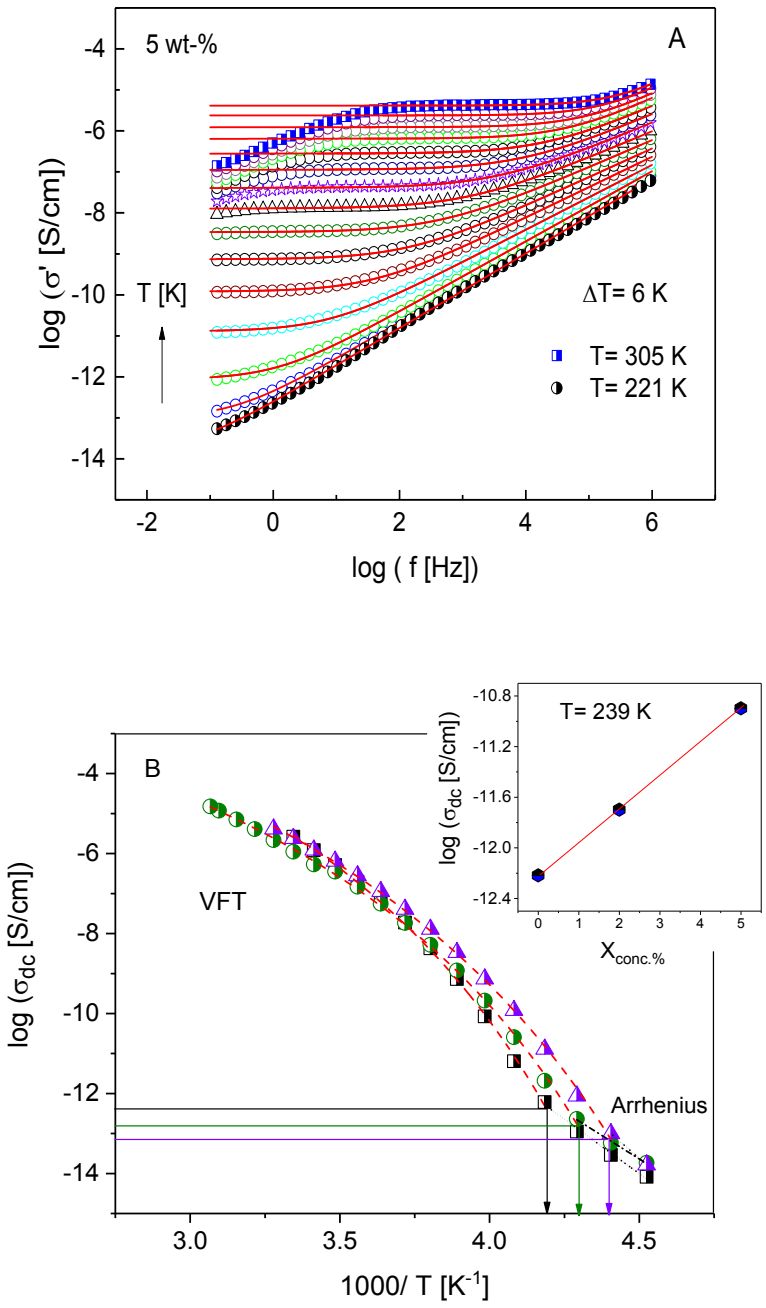

Figure 6.17: (A) Real part of the complex conductivity versus frequency for 5 wt-% of Ka-EDA at different temperatures as indicated. Solid lines are fits for a Jonscher power law to the data (B) dc conductivity plotted versus 1000/T for the HPAMAM/Ka-EDA: squares - pure HPAMAM, circles –2 wt-%, and triangles –5 wt-% of Ka-EDA. Dashed lines are fits of the VFT equation to the data for temperatures above T_g. Dashed-dotted lines are fits of the Arrhenius equation at temperatures below T_g. The inset gives dc conductivity versus the concentration of the nanofiller at T=239 K. The solid line is a linear regression using all data points.

With decreasing temperature, it is supposed that both the segmental dynamics and the motion of charges carriers slow down. The temperature dependence of the dc conductivity of HPAMAM/Ka-EDA nanocomposite changes from a VFT dependence to an Arrhenius behavior at temperatures below the glass transition temperatures, T_g, measured by DSC (decoupling phenomenon). In other words, at temperatures below T_g, the migration of charges carriers is still possible in nanocomposites having some isolated layers, even though the segmental relaxation is expected to be frozen. A decoupling of the temperature dependencies of the segmental dynamics and the conductivity is supported as well by specific heat spectroscopy measurements. Hence, it is worth noticing that for HPAMAM and nanocomposites, the T_0 estimated by specific heat spectroscopy is significantly lower than that is estimated form the dc conductivity. Also, the fragility parameters have different values (compare Tables 6.2 and 6.3). This result further supports that there is a definite decoupling between the segmental dynamics and the conductivity relaxation. To characterize the mechanisms of charge transport, a decoupling index R_τ can be employed (see Eqs. 3.31and 3.32). The decoupling indices are calculated and given in Table 6.3. The high values of the decoupling indices indicate that for system considered here the charge transport might be due to proton conduction via a Grotthuss-type mechanism in addition to the vehicle type mechanism.

7. DIELECTRIC STUDY OF MOLECULAR MOBILITY IN HYBRANE/ KAOLINITE NANOCOMPOSITES

ABSTRACT: Hyperbranched polyester amide (Hybrane S 1200®)/ kaolinite (Ka-DCA) nanocomposites were prepared, via an ex situ approach. The morphology of the nanocomposites was characterized by SAXS and TEM. The results revealed that an exfoliated structure was observed, for Hybrane/ Ka-DCA nanocomposites with 10 and 20 wt-% nanofiller. Whereas, the nanocomposites with 30, 50, and 70 wt-% Ka-DCA showed a partly intercalated morphology. A complementary combination of methods such as differential scanning calorimetry (DSC), and broadband dielectric relaxation (BDS) were used to investigate the structure-property relationship of Hybrane and nanocomposites. DSC revealed a decrease in glass transition temperature, T_g, with increasing Ka-DCA content. The dielectric spectra of the Hybrane and the nanocomposites showed two relaxation processes. Further, the conductivity contribution was observed at temperatures above the T_g, for all samples investigated. The influence of nanofiller on the molecular mobility (confinement effects), and dc conductivity in Hybrane/ Ka-DCA nanocomposites were discussed in detail.

7.1. Characterization of Hybrane/Ka-DCA nanocomposites

Figure 7.1A shows the SAXS patterns for Hybrane and Hybrane/Ka-DCA nanocomposites. Hybrane is amorphous and thus there is no Bragg peak is observed. For the nanocomposites, a scattering peak is observed in high q-range at q_{max}= 2.96 nm^{-1}, corresponds to an effective interlayer distance ($d=2\pi/q_{max}$) of d=2.1 nm. This reflection is related to the scattering of small aggregates consisting of alkyl chains of DCA. Probably, the alkyl chains of intercalated DCA are adopted a mixture of ordered and disordered structure in the interlayer space of Ka [161]. The effect of the DCA is also detected in DSC measurements, as it will be discussed later. It is worth pointing out that the intensity of the peak at q = 2.96 nm^{-1} in Hybrane/Ka-DCA with 10 wt-%

Ka-DCA is lower than that in the other nanocomposites, nevertheless it has the pattern at the same q-value, confirming the same its origin.

At a lower q-range, at first glance, there are two behaviors for the SAXS pattern, suggesting two different morphologies of nanocomposite. For Hybrane/ Ka-DCA nanocomposites with 10 and 20 wt-% nanofiller, no further Bragg peak is observed, compared to pure Ka-DCA. This result could be assigned to an exfoliated structure (see Figure 7.2A). With increasing concentration of the nanofiller to 30, 50, and 70 wt-% Ka-DCA, a reflection at q_{max} =1.56 nm^{-1} is detected. This value gives an effective interlayer distance of d=4 nm. The characteristic interlayer spacing of Ka-DCA is d=3.6 nm. Thus, the increase of the interlayer distance refers to a partly intercalated structure (see Figure 7.2B). From these results, one can conclude that the morphology of the Hybrane/ Ka-DCA nanocomposites depends on the concentration of the nanofiller, hence the degree of the exfoliation of the layered silicates in the polymer matrix decreased with increasing the filler concentration. These findings are in agreement with TEM investigations (see Figure 7.3), where the Hybrane/ Ka-DCA with 10 and 20 wt-% nanofiller have an exfoliated structure, however a partly intercalated morphology was observed, for the samples with higher concentration of the Ka-DCA

Table 7.1: Interlayer distance $d=2\pi/q_{max}$, width, w, of the peak estimated by fitting a Gaussian to the data, the correlation length in direction perpendicular to the lamella $I_c=2\pi/w$, and the effective number of layers, N.

Sample	*d (nm)*	*w (nm^{-1})*	*I_c (nm)*	*N*
30 wt-%	4.05	0.1176	53.4	13.2
50 wt-%	4.05	0.0728	86.2	21.3
70 wt-%	4.01	0.1676	37.5	9.32

The width (w) of the peak was estimated by fitting a Gaussian to the data. The results are summarized in Table 7.1. Compared to the effective number of layers in the Ka-DCA nanofiller (I_c/d=98), the effective number of layers for the Hybrane/Ka-DCA nanocomposites is smaller than that of Ka-DCA and further it varies with the concentration of the nanofiller. This result confirms a partly intercalated structure, where the Ka-DCA nanofillers are arranged in stacks, which are partly dispersed within the Hybrane matrix. Meanwhile, the order of the layered structure is

maintained. An important point to notice is that the effective number of layers, *N*, as well as the correlation length, I_c, have non-systematic change with the concentration of the Ka-DCA (see Table 7.1), where the highest value is found for the sample with 50 wt-% of Ka-DCA. Probably, the degree of exfoliation of the nanofiller in sample with 50 wt-% is lower than that in samples with 30, and 70 wt-% Ka-DCA.

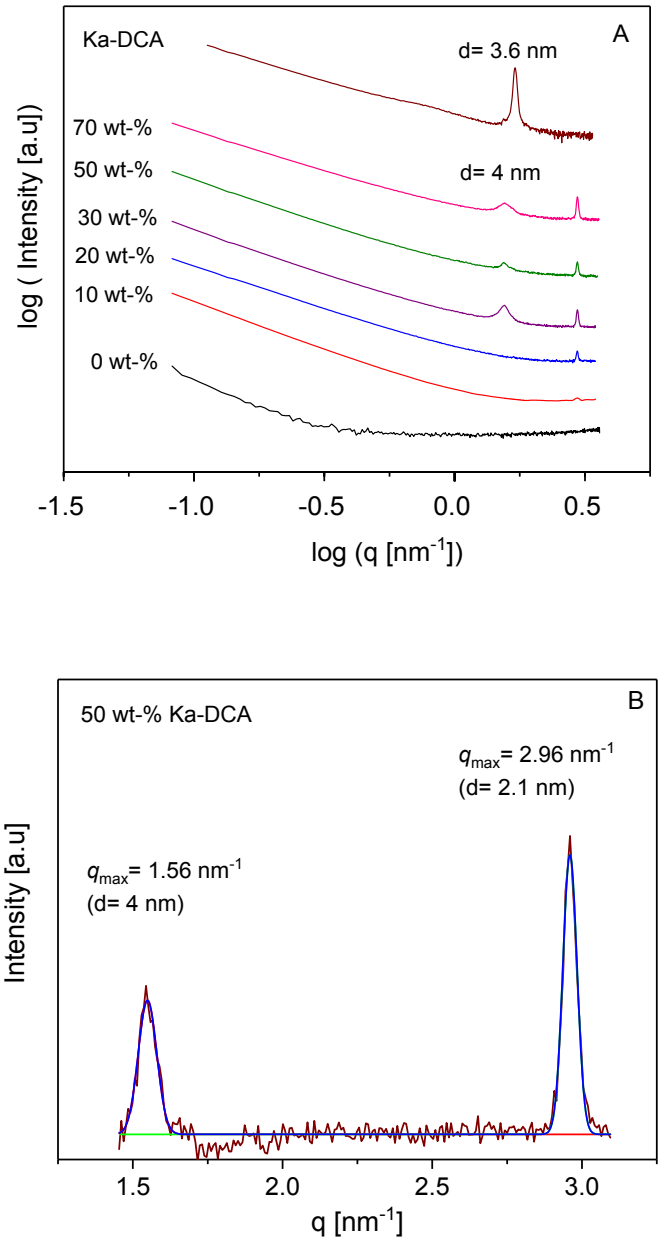

Figure 7.1: (A) X-ray diffraction pattern for Ka-DCA and Hybrane/Ka-DCA nanocomposites with different concentration of the nanofiller as indicated. (B) An example for the Gaussian fitting to the data for the nanocomposite with 50 wt-% Ka-DCA.

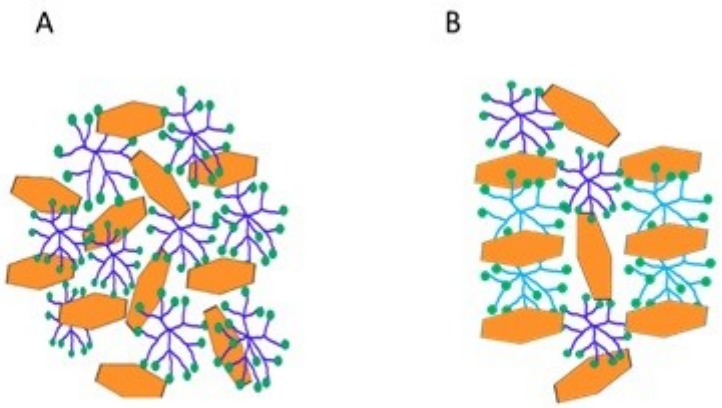

Figure 7.2: Schematic picture showing the structure of Hybrane/kaolinite nanocomposites. (A) Exfoliated nanocomposite observed for 10 and 20 wt-% of the Ka-DCA nanofiller, and (B) Mixed structure was detected for 30, 50, and 70 wt-% of the Ka-DCA nanofiller.

Figure 7.3 depicts some TEM pictures of Hybrane/Ka-DCA nanocomposites. The TEM image for Hybrane/ Ka-DCA with 10 wt-% nanofiller did not show any features indicative of crystalline phases inside the matrix (a completely exfoliated morphology) (Figure 7.3B). For the sample with 20 wt-% Ka-DCA, nevertheless the lower magnification was presented (500 nm), well dispersion of the nanofiller within the polymeric matrix is obvious (Figure 7.3C). Therefore, the intercalation of the Hybrane into the Ka-DCA layers seems to destroy the rod-like structure of DCA, see Figure 7.3A, and thus an exfoliated morphology was obtained. This result confirms the interaction of OH groups of the Hybrane with the nanofiller.

For the higher concentration of the nanofiller (30, 50 and 70 wt-% Ka-DCA), it is noticed that the rod-like structure of the pure Ka-DCA is disappeared. In addition, the usual hexagonal Ka crystal is observed [96] (see Figure 7.3D, E and F), confirming the interaction between OH groups of the Hybrane and the Ka-DCA. This could be considered due to change of the Ka-DCA morphology [205]. To better understanding one can take into account that, in general, an intercalation or exfoliation process results in change of morphological features of silicate layers [193]. Therefore, the natural platy Ka could be changed from hexagonal plates into nano-rods by intercalation, like in the case of Ka-DCA, and further some of regular structure could

be partly destroyed or changed into plates by the interaction between the polymer and the Ka-DCA. Thus, one could conclude that the TEM images revealed a mixed structure of intercalated and exfoliated morphologies, for nanocomposites with 30, 50, and 70 wt-% Ka-DCA. This is consistent with SAXS patterns.

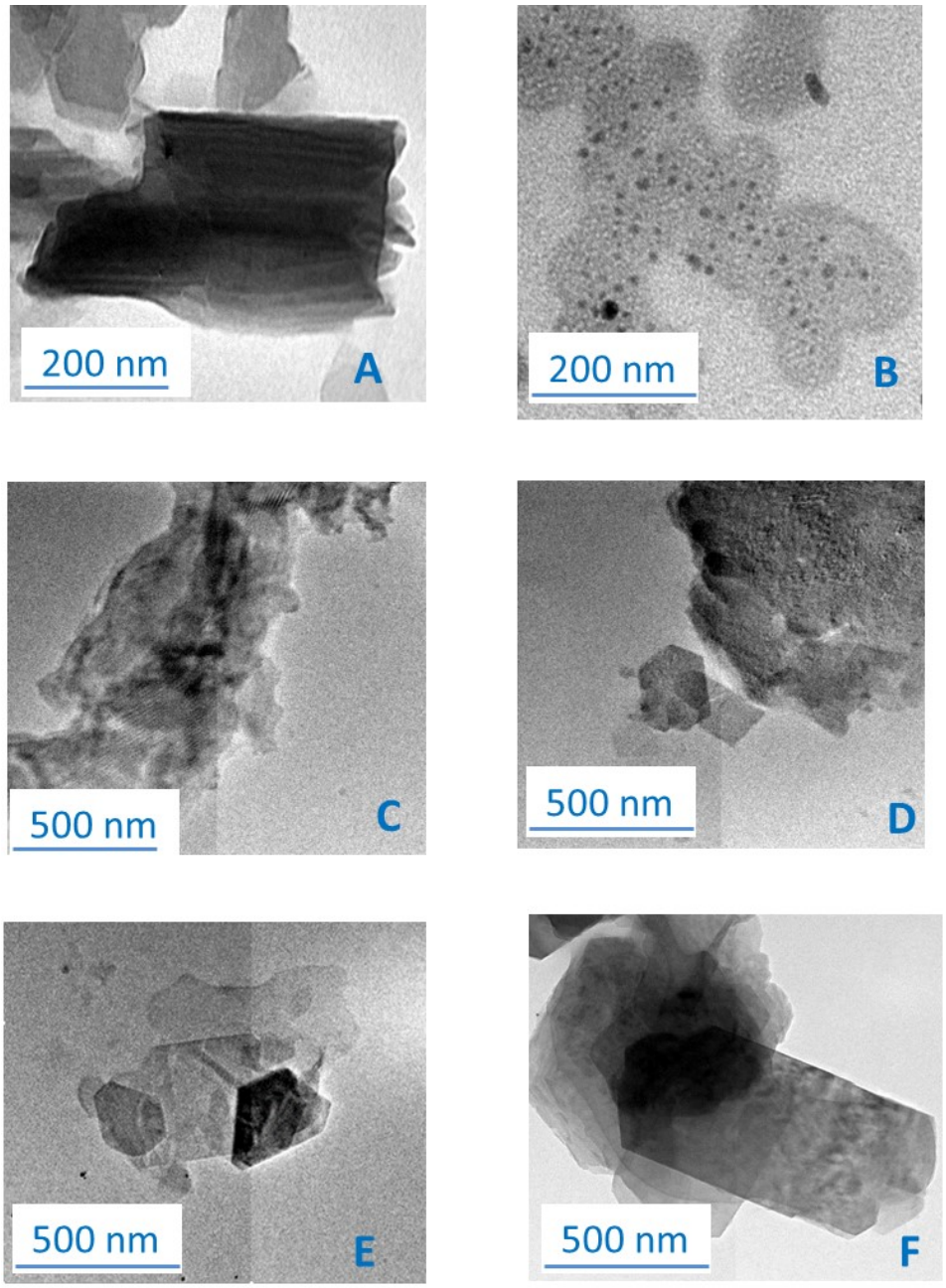

Figure 7.3: TEM pictures for modified kaolinite and the nanocomposites (Hybrane/ kaolinite nanocomposites): (A) pure Ka-DCA, and (B) 10 wt-% of the nanofiller. The size bar represents 200 nm.

(C) 20 wt-%, (D) 30 wt-%, (E) 50 wt-%, and (F) 70 wt-% of the nanofiller. This size bare represents 500 nm.

Figure 7.4 gives the DSC thermograms for Hybrane and the nanocomposites. The thermal glass transition temperature T_g is estimated from the midpoint of the second heating run and given in Table 7.2. For the nanocomposites, the T_g values decrease with increasing concentration of the nanofiller (see Figure 7.5). In addition to the glass transition, melting peaks were observed, for all nanocomposites investigated. Although the melting points varied to some degree ($T_m \sim 332 \pm 6$ K), the melting peaks should be related to the Ka-DCA. This is because of the fact that the pure Hybrane shows no phase transition (amorphous polymer). Probably, the long alkyl chains of DCA can cause an ordering or even semicrystalline structure in the polymer [33,206].

Table 7.2 Glass transition temperature T_g (10 K/min, second heating), VFT parameters estimated from BDS and the fragility parameter for the α-relaxation of Hybrane and its nanocomposites. In addition, the activation parameters for the β-relaxation are given.

Sample Hybrane/Ka-DCA	α-relaxation (BDS)					β-relaxation	
	T_g [K]	log (f_∞ [Hz])	A [K]	T_0 [K]	D_f	log (f_∞ [Hz])	E_A [kJ/mol]
Hybrane	309	12	862.70	259.7	3.3	17.6	65.7
10 wt-%	301	12	828.30	254.3	3.3	16.4	59.6
20 wt-%	294	12	833.40	256.4	3.3	17.6	63.1
30 wt-%	295	12	966.00	238.0	4.0	16.8	59.3
50 wt-%	281	12	1059.7	216.8	4.9	16.4	57.4
70 wt-%	284	12	1011.7	226.9	4.6	16.3	57.7

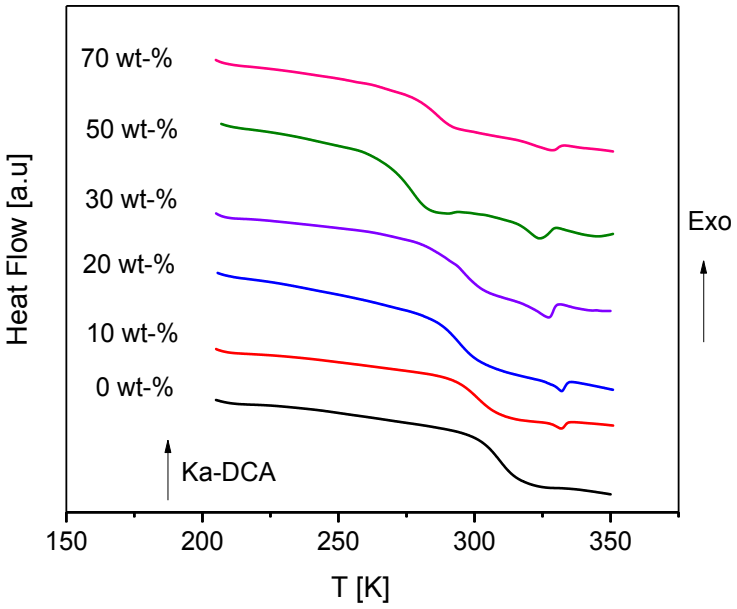

Figure 7.4: DSC thermograms for Hybrane and the nanocomposites with different concentrations of the nanofiller as indicated (10 K/min, second heating). The curves are shifted along the y scale for sake of clearness.

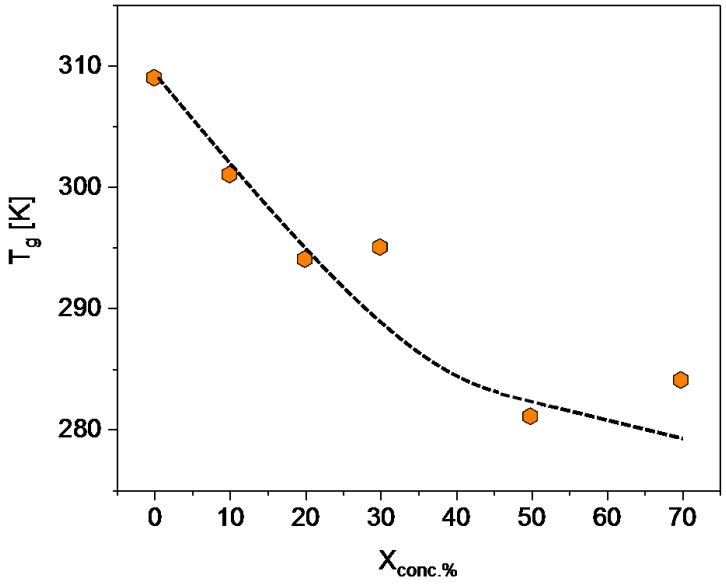

Figure 7.5: Glass transition temperature versus concentrations of the nanofiller.

7.2. Dielectric spectroscopy

The molecular mobility was investigated by BDS in a wide range of frequencies and temperatures, both above and below the glass transition temperature, T_g, for the Hybrane and the nanocomposites. Figure 7.6A displays the imaginary part of the complex dielectric function, ε'', for the Hybrane versus temperature at 1 kHz. At temperatures below T_g, the β-relaxation is observed. Close and above T_g, the segmental dynamics (α-relaxation) is detected. With further increasing temperature, the high values of ε'' may be due to the dc conductivity contributions, which is dominated in the dielectric behavior of the HBPs, as well as interfacial polarization. A similar behavior was observed for all samples investigated.

In the dielectric loss spectrum, the segmental dynamics (α-relaxation) is overlapped by dc conductivity. Thus, in this work, the complex electric modules ($M^*(f) = M'(f) + iM''(f) = 1/\varepsilon^*(f)$) representation is useful, where the conductivity contribution is converted into a peak. Figure 7.6B shows the imaginary part of complex electric modules, M'', versus frequency in the range of temperatures from 318 K to 366 K, for the Hybrane. The spectra show two pronounced peaks. Because of the selected temperatures shown in Figure 7.6B are above the polymer glass transition temperature (T_g = 309 K): Therefore, the relaxation process at lower frequencies could be attributed to the dc conductivity contribution and/or MWS polarization. Whereas, the second one is related to the segmental dynamics (α-relaxation). The α-relaxation is characterized by a peak in the electric modulus representation, like for the complex dielectric function. Obviously, the M'' peaks shift to higher frequencies and decrease in intensity with increasing temperatures.

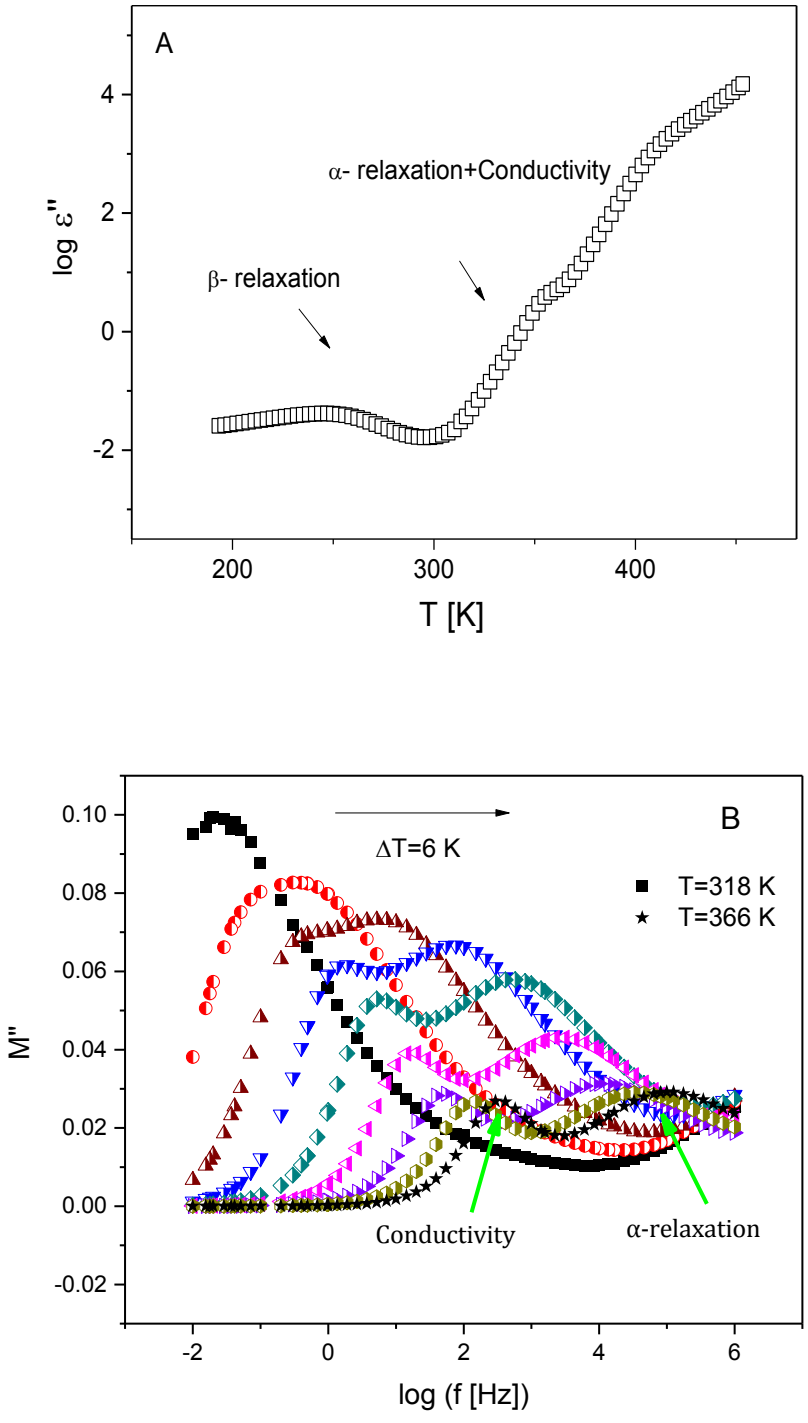

Figure 7.6: (A) Dielectric loss versus temperature at a frequency of 10^3 Hz for the Hybrane. (B) The imaginary part of the electric modulus versus frequency at different temperatures as indicated, for the Hybrane.

Figure 7.7 shows the temperature dependence of the imaginary part of the electric modulus *M*" at 1 kHz, for the Hybrane and its nanocomposites. Different relaxation processes are observed. At low temperatures, below the T_g, a broad peak is observed for all samples investigated, which is assigned as the β-relaxation due to the motion of localized groups. With increasing the temperature close to the T_g, an additional weak process is observed as a low-temperature shoulder of the main the segmental dynamics (α-relaxation) (see arrows), for the samples with 30, 50, and 70 wt-% Ka-DCA. Probably, it is related to the segmental dynamics of the polymer that is not confined within the layered silicate. The exact origin for this appears difficult to understand and would require a further investigation. Above the T_g, two relaxation processes are observed, for the Hybrane and nanocomposites. The first peak at lower temperatures is attributed to the α-relaxation and the second one at higher temperatures reflects the conductivity contribution. For higher concentration of the nanofiller (30, 50 and 70 wt-% Ka-DCA), the α-relaxation is overlapped by the dc conductivity and/ or interfacial polarization effects, further the maximum of *M*" shifts to lower temperatures with increasing concentration of the Ka-DCA.

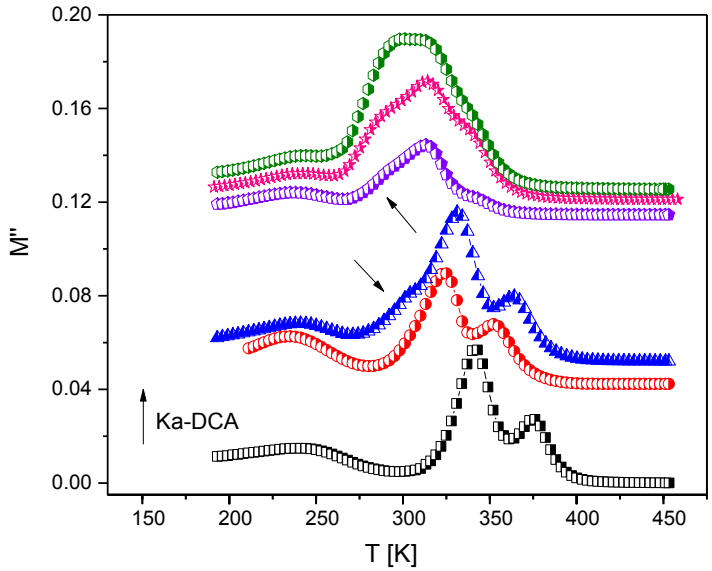

Figure 7.7: Imaginary part of the complex dielectric modules M" versus temperature for Hybrane/Ka-DCA samples: squares, Hybrane; circles, 10 wt-%; triangles, 20 wt-%; diamonds, 30 wt-%; stars, 50 wt-%, and pentagons, 70 wt-% of Ka-DCA at f = 1 kHz as. The curves are shifted along the y-scale for sake of clarity

For further analysis of the relaxation processes, the model function of Havriliak-Negami (HN) [134] (Eq 3.25) was fitted to the data. From the fit of the HN-function the relaxation rate f_p, (the relaxation map) is obtained [24]. Figure 7.8 gives the temperature dependence of the relaxation rate, $f_{p,\beta}$, for the β-relaxation in the relaxation map for Hybrane/Ka-DCA nanocomposites. Its relaxation times can be described by an Arrhenius relation (Eq. 3.2). The activation parameters for the β-relaxation of different samples are represented in Table 7.2. This process is attributed to local fluctuations and rotation of the end- and/or side groups of the Hybrane molecules, i.e., the methyl and/or the hydroxyl groups [31]. Recently, the molecular dynamics of hyperbranched polyester amide (Hybrane)/ montmorillonite (Na^+−MMT) nanocomposites was investigated, via a quasielastic neutron scattering [31]. The result showed that the local processes were not affected by the confinement. However, a recent BDS measurement for different generation of hyperbranched polyesters Boltorn, confined within the layered MMA, reported that the β-relaxation is significantly faster and with a lower activation energy than those of the Boltron [172].

Here, a similar behavior was observed for the Hybrane/Ka-DCA nanocomposites, where the activation energy decreased in confinement from 65 to 57 ± 2 kJ/mol. On a molecular level, this could be resulted from change or disruption of the systems of hydrogen bonding interaction under confinement. It could be considered by assuming that with increasing nanofiller content, the intramolecular hydrogen bonding is dominant and intermolecular hydrogen bonding is negligible, due to the interaction between OH groups of the Hybrane and the Ka-DCA. Therefore, the hydrogen bonding network is changed under confinement, which results in the fluctuations of the end- and/or side groups become less restricted. In this way, the activation energy clearly decreased in the nanocomposites, compared to the pure polymer. Nevertheless, the activation energy is more or less similar for the all nanocomposites (see Table 7.2).

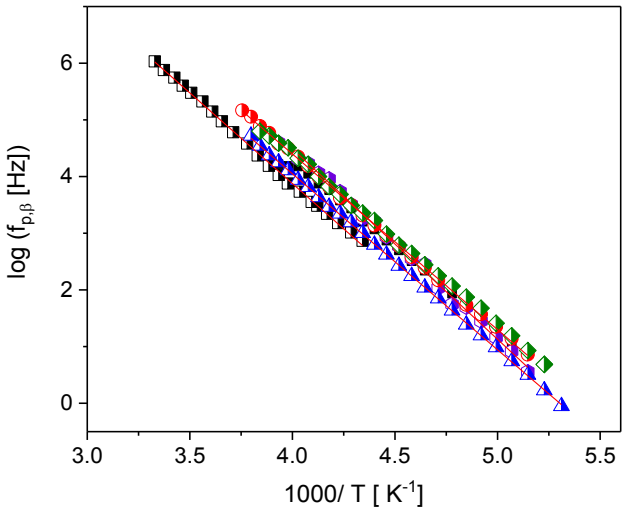

Figure 7.8: Relaxation rate of the β-relaxation inverses temperature (relaxation map), as obtained from the BDS, for the Hybrane/Ka-DCA samples: squares, Hybrane; circles, 10 wt-%; triangles, 20 wt-%; diamonds, 30 wt-%; stars, 50 wt-%, and pentagons, 70 wt-% of Ka-DCA. The solid lines are fits of the Arrhenius equation to the data.

Figure 7.9A shows Dielectric loss ε″ versus frequency for the α-relaxation the of the Hybrane/Ka−DCA samples at T = 347 K. There is a remarkable effect of the Ka-DCA on the α -relaxation in shifting the maximum peak position towards the higher frequencies. Please note that, for nanocomposites with 50 and 70 wt-% content, the fitting was done by using the so-called ‘‘conduction-free’’ approximation [24]. For a Debye-process

$$\varepsilon''^2 = -\frac{\partial \varepsilon'}{\partial log \omega}. \qquad (7.1)$$

is derived. According to Eq. 7.1, a relaxation peak in ε′′ depicts a minimum in $\partial\varepsilon'/\partial log$. As a result of the squared ε′′ in Eq. (7.1) the minimum is narrower than the peak in ε′′. Also, keeping in mind that the real part of complex dielectric function ε' is not affected by dc conductivity as long as electrode polarization and Maxwell/Wagner effects remain negligible. Thus, the α -relaxation was resolved via the derivate of ε′ (see Figure 7.9B). It is worth mentioning that the ‘‘conduction-free’’ model was also fitted to the data for the nanocomposites with a lower concentration of the Ka-DCA.

The result is consistent with that was estimated using the model function of Havriliak-Negami (HN).

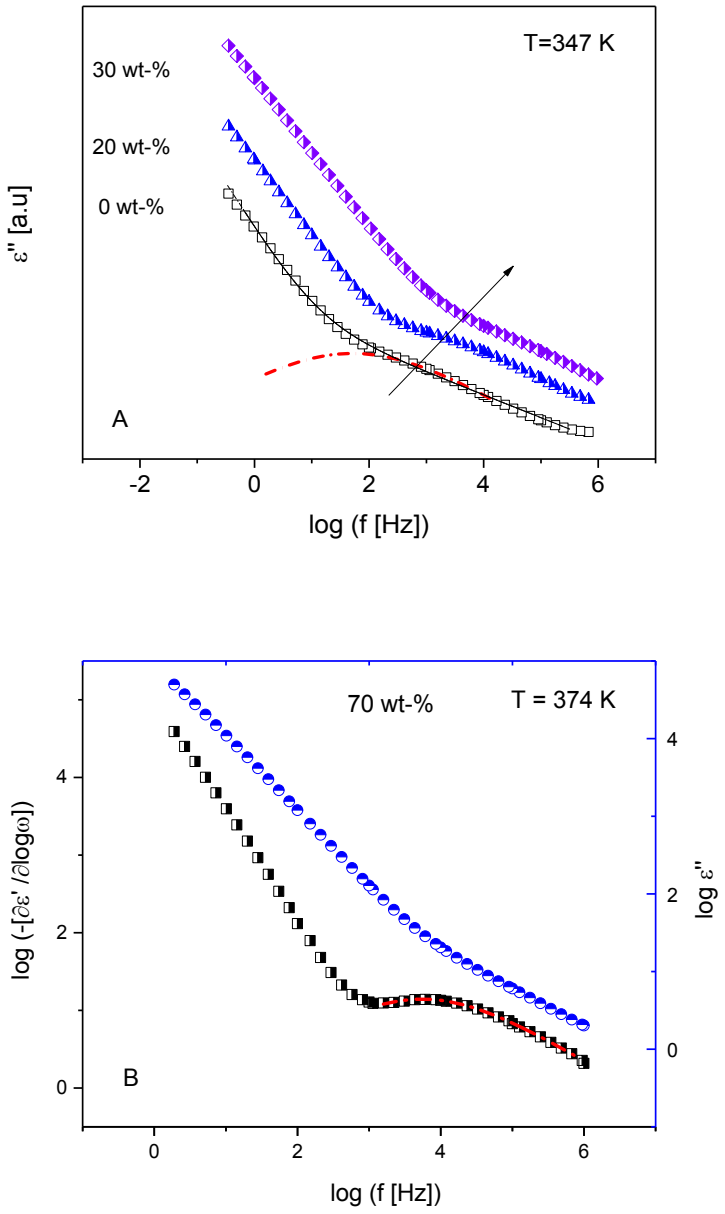

Figure 7.9: (A) Dielectric loss ε″ versus frequency for the α-relaxation the of the Hybrane/Ka–DCA samples at T = 347 K: squares, Hybrane; triangles, 20 wt-% Ka–DCA, and diamonds, 30 wt-% Ka–DCA. The solid line is a fit of the HN-function to the data of Hybrane including a conductivity contribution. The dashed-dotted line indicates the contribution of the relaxation process. (B) Comparison of ε″ (blue circles) and $\partial\varepsilon'/\partial \log \omega$ (black squares) versus frequency for the α-relaxation of the Hybrane/Ka–DCA with 70 wt-% Ka-DCA at T = 347 K. The dashed-dotted line is a fit of the HN-function to the data.

Figure 7.10 represents the temperature dependence of the relaxation rate $f_{p,\alpha,}$ for α-relaxation in the relaxation map, for Hybrane and nanocomposites. It is curved when plotted versus *1/T,* as expected, and can be described by a VFT formula (Eq. 2.3) [120-122]. The fitting parameters are given in Table 7.2. The most aspects from this result is that the Vogel temperature of the segmental dynamics decreases with increasing concentration of the nanofiller. Further, the fragility parameter is D= 3.3, for Hybrane and nanocomposites with 10 and 20 wt-% Ka-DCA. Whereas, the fragility increased with increasing concentration of the nanofiller to 30, 50, and 70 wt-% Ka-DCA, indicating that the increase in the filler content leads to stronger glasses.

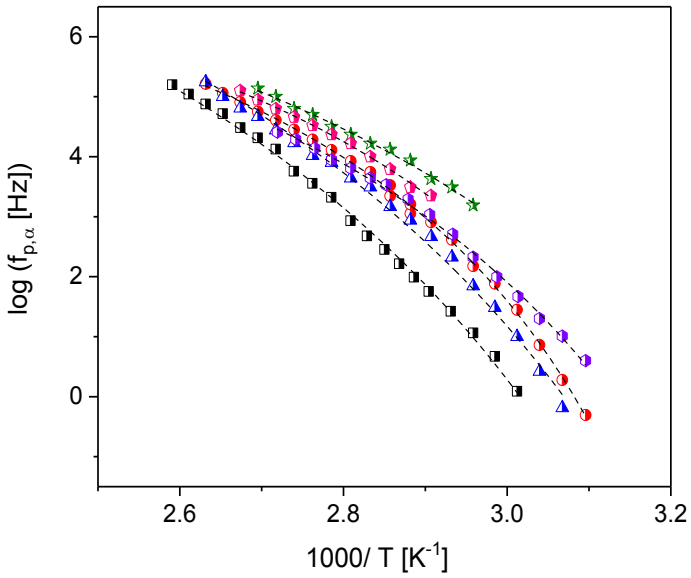

Figure 7.10: Relaxation rate of the α-relaxation versus invers temperature (relaxation map), as obtained from the BDS, for the Hybrane/Ka-DCA samples: squares, Hybrane; circles, 10 wt-%; triangles, 20 wt-%; diamonds, 30 wt-%; stars, 50 wt-%, and pentagons, 70 wt-% of Ka-DCA. The dashed lines are fits of the VFT equation to the data.

It noteworthy that the segmental dynamics (α-relaxation) becomes faster in nanocomposites and shifts to lower temperature with increasing concentration of the Ka-DCA. This process reflects the fluctuations of the Hybrane segments, involving cooperative motion of several groups as discussed elsewhere, for the Hybrane [207].

The result suggests that the confinement effect for the segmental dynamics becomes more pronounced in partly intercalated nanostructures (30, 50 and 70 wt-% of the Ka-DCA).

The frequency dependence of the real part of the complex conductivity, σ´, for Hybrane and nanocomposites is given in Figure 7.11A at T= T_g + 20 K. A selected temperature was taken as an example for the temperature that is higher than the T_g of each sample by 20 K. The plateau value which is corresponds to the dc conductivity is obvious, at temperatures above the T_g. Thus, the dc conductivity, having a contribution from the segmental dynamics as well as the motion charge carriers, can be estimated. The conductivity spectra show the typical behavior expected for semiconducting polymeric materials, as previously discussed (see section 3.1.5). Obviously, with increasing concentration of the nanofiller, the dc conductivity σ_{dc} increases up to 2 orders of magnitude, for the sample with 70 wt-% of Ka-DCA, compared to the pure polymer.

Figure 7.11B shows the dc conductivity at T= T_g + 20 K versus the concentration of the Ka-DCA where an almost linear increase of σ_{dc} with the concentration is observed. This linear relationship seems to indicate the increase of dc conductivity is due to increase the number of unboned DCA molecules. It was reported [192,205] that the interaction between the polymer and the basal oxygen plane of silicate layered is more favorable than that between clay and DCA. This favorable interaction leads to substitute of DCA molecules between the Ka-DCA sheets by the polymer segment. Thus, unboned DCA molecules might be acted as ions to charge transport. Further, according to the definitions of dc conductivity (see Eq.3.30), the increase of dc conductivity could be attributed to increase of the charge carrier density. Here, the number of protons could be increased due to the interaction of the OH groups in Hybrane with the OH groups of Ka-DCA, in addition to in the existence of small traces of water, which will increase the number density of charge carriers and, hence, the conductivity. Moreover, it was noted that increase filler concentration led to increase the confinement effect and, thus, the dynamics glass transition becomes faster, for the Hybrane/Ka-DCA nanocomposites. In this regard, the acceleration of segmental dynamics enhances in parallel the dc conductivity of the polymer.

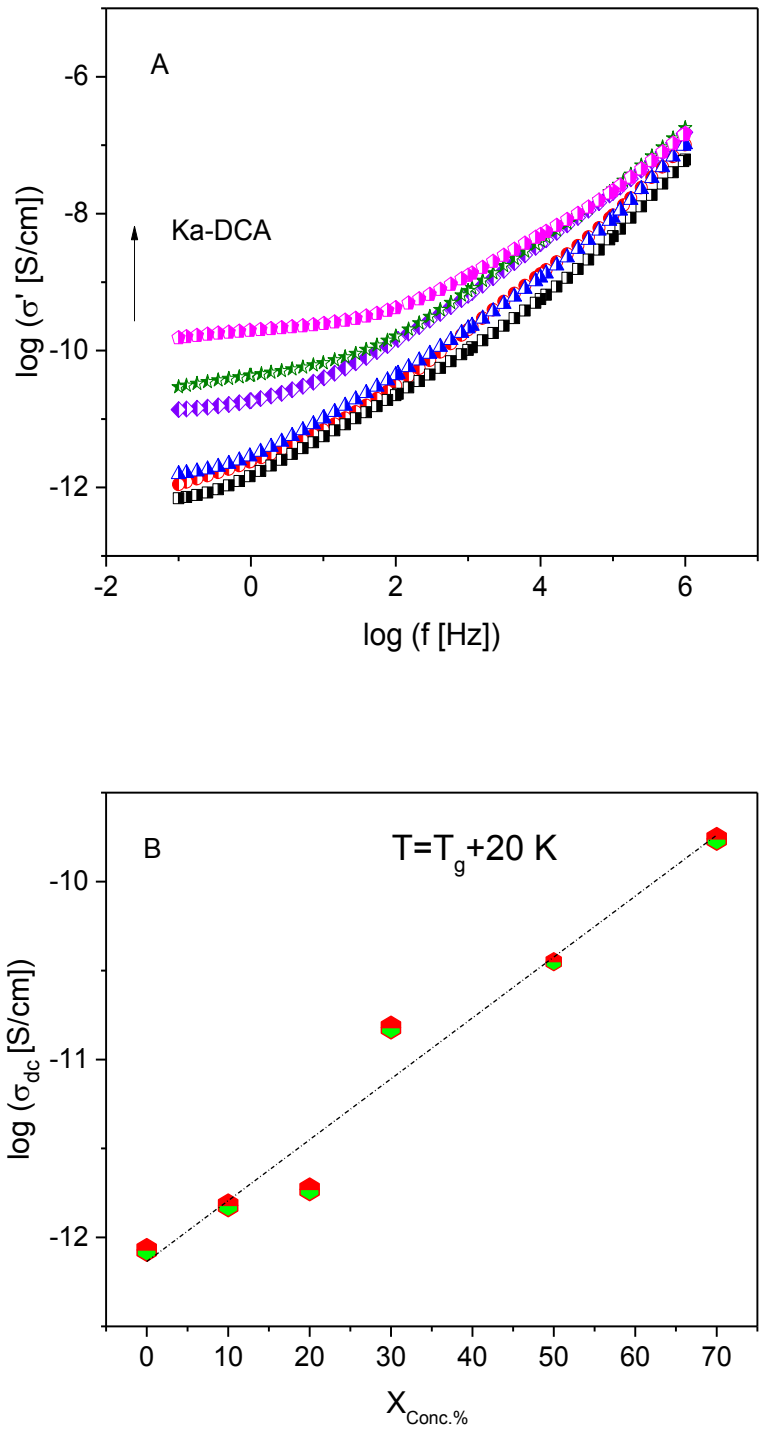

Figure 7.11: (A) Real part of the complex conductivity plotted versus frequency: squares, Hybrane; circles, 10 wt-%; triangles, 20 wt-%; diamonds, 30 wt-%; stars, 50 wt-%, and pentagons, 70 wt-% Ka-DCA at T= T_g+ 20 K. (B) dc conductivity versus the concentration of the nanofiller at T=T_g+20 K.

The frequency dependence of the real part of complex conductivity function can be approximated by the well-known Jonscher power law (see section 3.1 Eq.3.29) [139]. Figure 7.12A depicts the dc conductivity σ_{dc} as a function of inverse temperature for the Hybrane/ Ka-DCA nanocomposites. At high temperatures, above the T_g, the non-Arrhenius temperature dependency of the dc conductivity relaxation is observed, for all samples investigated. This relaxation rate can also be described by can be described by a VFT formula (Eq. 2.3) [120-122]. With decreasing temperature, both the segmental dynamics and the ionic motion slow down. For pure Hybrane and nanocomposites with 10 wt-%, in the temperature range around the T_g, the temperature dependence of the dc conductivity changes from a VFT dependence to an Arrhenius-like temperature dependence (Eq. 2.4). This transition suggests a decoupling phenomenon between the temperature dependence of segmental dynamics and that of charge transport. Noting that at temperatures below T_g in the glassy state the segmental dynamics is expected to be frozen, but however the motion of charges carriers is still possible.

For nanocomposites with high filler concentration (20, 30, 50, 70 wt-% Ka-DCA), at temperatures below T_g, the temperature dependence of the dc conductivity has different behavior as shown in Figure 7.12A. To confirm this a peculiar behavior a protocol of two subsequent cooling stages was used (see Figure 7.12B, as an example). Nevertheless, there is no reasonable explanation for such behavior. Probably, this effect is attributed to the high concentration of the nanofiller, which in turn could effect on the decoupling phenomenon. Further, there is still lack of qualitative studies on the effect of the nanofillers in decoupling phenomenon.

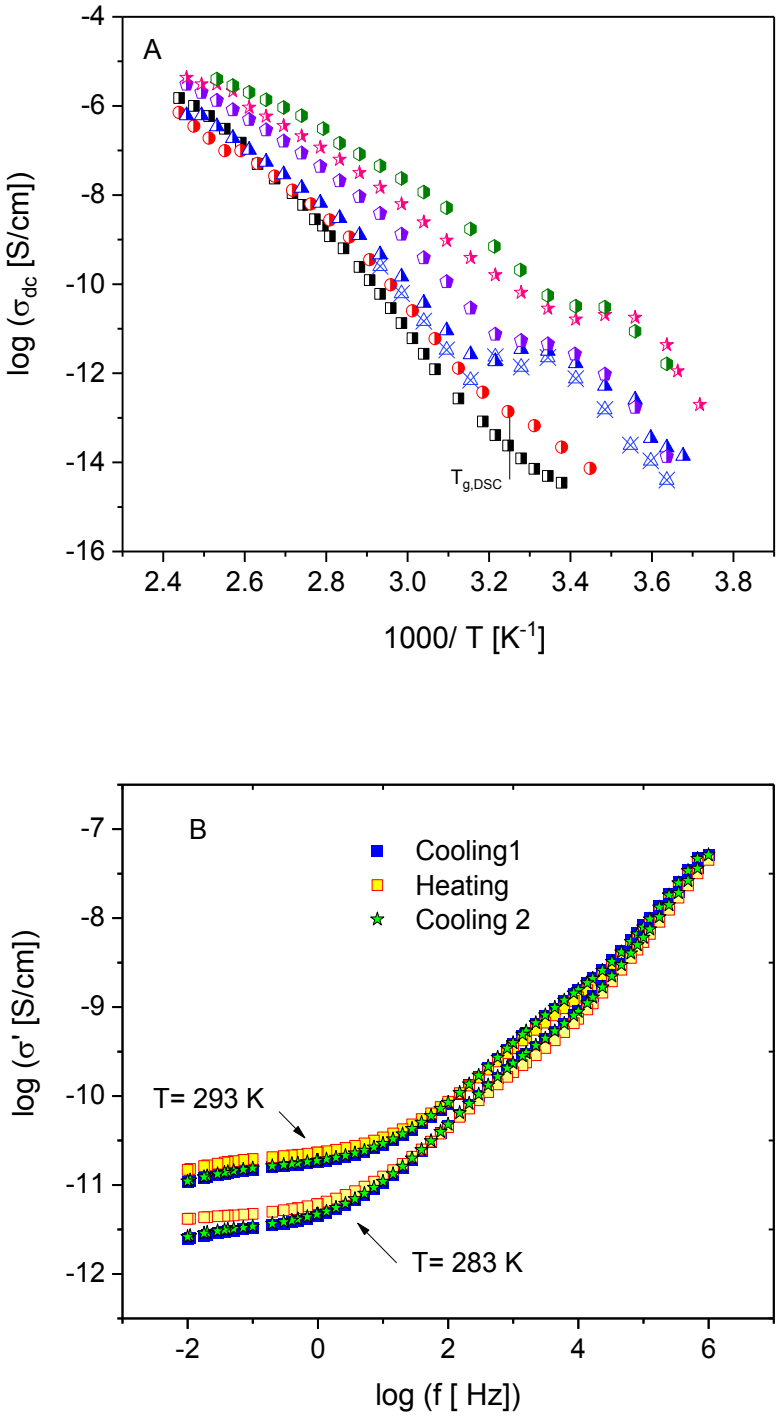

Figure 7.12: (A) dc conductivity σ_{dc} versus 1000/T for the Hybrane/ Ka-DCA samples: squares, Hybrane; circles, 10 wt-%; triangles, 20 wt-%; diamonds, 30 wt-%; stars, 50 wt-% and pentagons, 70 wt-% of Ka-DCA. Crosses open symbols correspond to the second cooling cycle for 30 wt-% Ka-CA. (B) An example for heating/ cooling cycles for the real part of the complex conductivity plotted versus frequency at T = 283 K and T= 293 K, for the data for the nanocomposite with 70 wt-% Ka-DCA.

8. CONCLUSIONS

In this study, different types of hyperbranched polymer (HBP)/kaolinite(Ka) nanocomposites were prepared. The structure of the polymer and the corresponding nanocomposites was investigated by different methods. As a first system (Chapter 5), nanocomposites based on hyperbranched polyamine ester (HPAE) and treated kaolinite were papered in two different ways. The first approach is an ex situ (solution-based) method, in which the prepared hyperbranched polyamine ester was inserted into the interlayers of the modified kaolinite. The second method is an in situ polymerization route. For the former method, the kaolinite has been modified by dodecylamine (DCA) and for the latter one by diethanolamine (DEA). SAXS measurements showed that the Ka interlayer space increased from 0.71 to 3.6 nm^{-1} for Ka-DCA and to 1.12 nm^{-1} for Ka-DEA. SAXS and TEM investigations showed that nanocomposites prepared by the in situ method have an intercalated morphology, where ex situ preparation results in a more or less exfoliated structure.

By a combination of BDS and SHS, the relaxation properties of the nanocomposites were investigated in dependence on frequency and temperature. The results revealed that for all prepared samples, the dielectric spectra are dominated on the lower frequency (higher temperature) side by a conductivity contribution. The segmental motion related to the dynamic glass transition was found to be screened out by the conductivity contribution. The in situ HPAE/Ka-DEA samples have more or less a similar thermal glass temperature. The localized molecular fluctuations (γ-relaxation) is unaffected by the nanofiller. The specific heat spectroscopy investigations reveal that the dynamic glass transition changes from a more fragile behavior observed for pure HPAE to a stronger one for the nanocomposites.

For ex situ HPAE/Ka-DCA nanocomposites, the activation energies of γ-relaxation for the nanocomposites were lower than the values found for the pure HPAE. This is probably due to change or partly disrupted network of hydrogen bonding due to the confinement and/or the presences of the nanofiller. The confinement effect of the Ka-DCA nanofillers reduces the glass transition temperature and enhances, at the same time, the electrical conductivity of the polymer. Further, a systematic change of the dynamic glass transition estimated by AC-chip calorimetry was observed, which is in agreement with a behavior expected for a confined sample.

By comparing the temperature dependence of the dynamic glass transition measured with AC-chip calorimetry and that of the dc conductivity measured by dielectric spectroscopy, a decoupling in their temperature dependencies was found. With increasing concentration of the nanofiller, which results in a stronger glass-formation behavior, this decoupling becomes weaker.

As a second system (Chapter 6), nanocomposites based on Hyperbranched poly(amidoamine) (HPAMAM) and kaolinite treated with dodecylamine (DCA) were prepared by an ex situ (solution-based) method. NMR spectroscopy proved the successful synthesis of the pure polymer. Further, the structure of obtained samples has been investigated by a combination of DSC, SAXS, and FTIR experiments. By FTIR measurements, the interaction of HPAMAM with Ka-DCA nanofiller was confirmed. An apparent increase number of carbonyl groups with regard to the amine groups were observed for the nanocomposites. This was related to a change in the hydrogen bonding network of the HBP, due to the filler particles. SAXS and TEM analysis result in a partly exfoliated structure for nanocomposites. DSC showed a decrease in the glass transition temperature with increasing the Ka-DCA nanofiller. The results indicate that with increasing the concentration of the nanofiller, an exfoliated structure becomes more pronounced, and thus the dynamics glass transition becomes faster, manifested by a lower T_g value.

The dielectric spectra are characterized by a high conductivity contribution at lower frequency and /or higher temperature for all samples. The analysis of the real part of complex conductivity showed that the dc conductivity increases with increasing the concentration of the nanofiller. This enhancement in dc conductivity is attributed to an increase of the number of protons abstracted from the carbonyl groups in the presence of small traces of water. It is important to notice that, due to the disruption of the hydrogen bonding network by the nanofiller, the number of free carbonyl groups increase.

A pronounced decoupling of conductivity from the segmental dynamics was found. The magnitude of the decoupling was characterized by a so-called decoupling index, which decreases almost linearly with increasing concentration of the Ka-DCA nanofiller. The high values of the decoupling indices evidences that the charge transport in the samples is controlled by proton conduction via a Grotthuss-type

mechanism in addition to the vehicle type mechanism. At temperature above the glass transition temperature T_g, the temperature dependence of the relaxation time of the conductivity follows the Vogel/Fulcher/Tammann (VFT) law, which changes to an Arrhenius-like dependence at temperatures below T_g. The estimated apparent activation energy of the proton conductivity decreases with increasing the concentration of the nanofiller by trend. This is attributed to the distortions of the hydrogen bonding network by the nanofiller. Moreover, the glass-formation behavior and the decoupling phenomenon become stronger for higher concentrations of the nanofiller. A qualitative correlation between the fragility, decoupling indices as well as the concentration of the nanofiller was concluded from the results.

Further, nanocomposites based on HPAMAM and kaolinite modified with ethylenediamine were prepared, via an in situ approach. The interaction of HPAMAM with Ka-EDA nanofiller was confirmed by FTIR measurement. SAXS proved an exfoliated structure of the nanocomposites, which was supported by TEM. For HPAMAM/Ka/EDA nanocomposites, a pronounced decrease in the glass transition temperature was detected by DSC, compared to pure polymer. By a combination of SHS and BDS, the dielectric properties of the samples investigated were studied in dependence on frequency and temperature. The result suggested that the dynamics glass transition becomes faster in the HPAMAM/Ka-EDA nanocomposites, which is consistent with decreasing the T_g. The activation energies of γ-relaxation for the nanocomposites were lower than the values found for the pure HPAMAM. This is likely produced from the confinement and/or the existence of the nanofiller, which resulted in change or partly disrupted network of hydrogen bonding.

The dc conductivity increased linearly with the concentration of Ka-EDA nanofiller, compared to pure HPAMAM. The decoupling between the conductivity relaxation time and that of segmental dynamics was observed. SHS showed that the 5 wt-% Ka-EDA nanofiller exhibits stronger deviations, compared to pure polymer. This result was also expected from the calculated fragility parameter.

In the last part (Chapter 7), hyperbranched polyester amide (Hybrane S 1200®)/ kaolinite-dodecylamine (Ka-DCA) nanocomposites, with different concentrations (10, 20, 30, 50 and 70 wt-%) of the Ka-DCA nanofiller, were prepared via an ex situ method. A complementary combination of methods such as DSC, BDS, SAXS, TEM and

SHS were used to investigate Hybrane and its nanocomposites. An exfoliated structure was suggested by SAXS and TEM, for a sample with 10 wt-% of Ka-DCA. With increasing concentration of the Ka-DCA, a partly intercalated structure was observed. DSC revealed that the T_g values decrease with increasing concentration of the nanofiller, due to the interaction between the methyl and/or the hydroxyl groups of Hybrane and the OH groups in the Ka-DCA. Probably, this interaction results in change and/ or partly distributed of the hydrogen bonding network.

The dielectric spectra of the Hybrane showed two relaxation processes. First process, the β-relaxation was observed at temperatures below T_g. This relaxation process is originated from localized motions of the methyl and/or the hydroxyl groups (the end- and/or side groups of the Hybrane molecule). Second relaxation process is an α-relaxation reflected the segmental motion of the Hybrane segments, involving cooperative motion of several groups and relating to the dynamic glass transition at temperatures above T_g.

For nanocomposites, at the one hand, the confinement effect was less pronounced in the case of β-relaxation, whereas a decrease in the activation energies was observed, due to distortions of the hydrogen bonding network. At the other hand, the α-relaxation, in confinement, becomes faster than that in the pure polymer, where it shifts to a lower temperature with increase concentration of the nanofiller. It is worth mentioning that the confinement effect for the segmental dynamics becomes more pronounced in a partly intercalated nanostructure (30, 50 and 70 wt-% of the Ka-DCA nanofiller). The dc conductivity of the nanocomposites shows a strong dependence on the concentration of the Ka-DCA, whereas it increases approximately linearly with increasing nanofiller concentration. On the one hand, the increase of dc conductivity could be attributed to increase unbonded DCA molecules, which may act as ions to charge transport. On the other hand, the increase of dc conductivity can be interpreted by taking into account that the deformation of the hydrogen bonding network could be increased with increasing concentration of the Ka-DCA. Thus, the number of protons increased. In addition to in the existence of small traces of water, additional free protons could be found, which lead to increase of the density of charge carriers and hence the dc conductivity. For Hybrane/ Ka-DCA nanocomposites with 20, 30, 50, and 70 wt-% nanofiller, A peculiar behavior was observed for the

temperature dependence of the dc conductivity at temperatures below T_g. Till now, there is no reasonable explanation for such behavior. Probably, this effect is attributed to the high concentration of the nanofiller, which in turn change the decoupling phenomenon.

In the framework of this thesis, it was evident that the method of the preparation of the nanostructures, the end-groups of HBPs, the concentration of the nanofiller, and the treatment of its surface have a significant effect on preparing exfoliated or intercalated nanocomposites. Thus, new nanocomposites with tailor made properties could be obtained. To sum up, at the moment, it looks like that there is still no limit and no end for studies on HBPs nanocomposites.

Based on the experimental data presented in this work, it is worthwhile to further quantify the transport behavior of charge carriers in a wider range of HBP/nanocomposites, via the BDS and other complementary methods. Despite the promising industrial application of HBP/nanocomposites, there are only few reports that discuss issues concerning the dynamics of charge carriers in HBP/nanocomposites. Thus, a systematic investigation of different types of HBP/nanocomposites, including HBPs with different end-groups, and other nanofillers could be vital to reveal out the optimum conditions, for design new materials using in specific application such as in energy storage [208].

Recently [209], a separation between the segmental dynamics and the conductivity relaxation (decoupling phenomenon) has attracted attention for design and development of highly conducting solid polymers. In HBP/ nanocomposite systems, some factors such as, the influence of the preparation method, the concentration of nanofiller, and fragility are reported to affect the decoupling phenomenon, but they are not well understood. Thus, a further investigation using the temperature-dependent infrared measurements to investigate intramolecular glass-transition dynamics of HBPs nanocomposites could be of interest. This because the temperature dependencies of integrated intensity of hydrogen band for system of HBPs/ nanocomposites can be estimated, which allows to reveal the distortion of hydrogen bonding network as well as the relation between the degree of decoupling and structure of HBPs/ nanocomposites.

It would be hypothesized that a large number of reactive end-groups of the HBPs would be available, for further reaction, after the exfoliation by nanoparticles. Therefore, the future study aims to explore the use of the samples prepared to improve the mechanical and gas transport properties of linear polymer such as polystyrene.

Confinement effects on HBPs in terms of thin film and polymer nanocomposites, which is different from that of linear polymers. A fundamental understanding is still missing. Such work can improve our understanding of the HBPs dynamics in geometric confinement. Future measurements, utilizing SHS and BDS, could be interesting, for both scientific research and potential applications.

9. REFERENCES

(1) Flory PJ. J. Am. Chem. Soc. **1952**, 74, 2718.

(2) Kim, Y.: US Patent 4857630, **1987**; YH Kim and OW Webster. Polym. Prep **1988**, 29, 310.

(3) Kienle, R. H.; Hovey, A. Journal of the American Chemical Society **1929**, 51, 509-519.

(4) Yan, D.; Gao, C.; Frey, H; John Wiley & Sons **2011**; Vol. 8.

(5) Voit, B., Part A: Polymer Chemistry **2000**, 38, 14, 2505-2525.

(6) Wang, D.; Zhao, T.; Zhu, X.; Yan, D.; Wang, W. Chemical Society Reviews **2015**, 44, 4023-4071.

(7) Tomalia, D. A.; Baker, H.; Dewald, J.; Hall, M.; Kallos, G.; Martin, S.; Roeck, J.; Ryder, J.; Smith, P. Polymer **1985**, 17, 117-132.

(8) Xu, Y.; Gao, C.; Kong, H.; Yan, D.; Luo, P.; Li, W.; Mai, Y. Macromolecules **2004**, 37, 6264-6267.

(9) Yik, B. J.; Guo, M.; Kwon, Y.; Goodson, T. Journal of Physical Chemistry C **2017**, 121, 7108-7122.

(10) Ratna, D.; Becker, O.; Krishnamurthy, R.; Simon, G.; Varley, R. Polymer **2003**, 44, 7449-7457.

(11) Rodlert, M.; Plummer, C. J.; Grünbauer, H. J.; Månson, J. A. Advanced Engineering Materials **2004**, 6, 715-719.

(12) Rodlert, M.; Plummer, C. J.; Garamszegi, L.; Leterrier, Y.; Grünbauer, H. J.; Månson, J.-A. E. Polymer **2004**, 45, 949-960.

(13) Plummer, C. J.; Rodlert, M.; Bucaille, J.-L.; Grünbauer, H. J.; Månson, J.-A. E. Polymer **2005**, 46, 6543-6553.

(14) Alongi, J.; Monticelli, O.; Russo, S.; Voit, B. Journal of Nanostructured Polymers and Nanocomposites **2007**, 3, 3-12.

(15) Zou, J; Shi Y; Z, Sheng, W X; Nie K.. Polym. Adv. Technol **2005**, 16, 55.

(16) Ruggerone, R.; Geiser, V. r.; Dalle Vacche, S.; Leterrier, Y.; Manson, J.-A. E.: Macromolecules **2010**, 43, 10490-10497.

(17) Huang, X.; Peng, P.; Peng, W.; Yu, J.; Liu, F.; Jiang, P. In Condition Monitoring and Diagnosis (CMD), 2012. International Conference on; IEEE **2012**, pp 1089-1092.

(18) Ghanem, A.; El-Gendi, A.; Rehim, M. A.; El-Khatib, K. RSC Advances **2016**, 6, 32245-32257.

(19) Somboonsub, B.; Thongyai, S.; Praserthdam, P.: J. Applied Polymer Science **2009**, 114, 3292-3302.

(20) Adachi K, Kotaka T. Prog. Polym. Sci. **1993**, 33, 60.

(21) McCrum N, Read B, Williams G. Wiley: NY reprinted by Dover Publications **1991**.

(22) Ngai KL, Randell RW. In T.A. Skotheim Editor, "Handbook of Conducting Polymer". Ch 28, Marcel Dekker, NY **1986**, 2, 967.

(23) Runt JP, Fitzgerald JJ. "Dielectric Spectroscopy of Polymeric Materials". Am. Chem. Soc. Washington. DC **1997**.

(24) Kremer, F., Schönhals, A., Eds. Broadband Dielectric Spectroscopy; Springer Verlag: Heidelberg **2003**.

(25) Okrasa, L.; Zigon, M.; Zagar, E.; Czech, P.; Boiteux, G.: Journal of Non-Crystalline Solids **2005**, 351, 2753-2758.

(26) Sangoro, J.; Turky, G.; Abdel Rehim, M.; Iacob, C.; Naumov, S.; Ghoneim, A.; Kärger, J.; Kremer, F. Macromolecules **2009**, 42, 1648-1651.

(27) Garcia-Bernabé, A.; Diaz-Calleja, R.; Haag, R. Macromolecular Chemistry and Physics. **2006**, 207, 970–977.

(28) Garcia-Bernabé, A.; Dominguez-Espinosa, G.; Diaz-Calleja, R.; Riande, E.; Haag, R. The Journal of chemical physics **2007**, 127, 124904.

(29) Román, F.; Colomer, P.; Calventus, Y.; Hutchinson, J. M. Materials **2016**, 9, 192-218.

(30) Turky, G.; Shaaban, S. S.; Schönhals, A. Journal of Applied Polymer Science **2009**, 113, 2477-2484.

(31) Fotiadou, S.; Karageorgaki, C.; Chrissopoulou, K.; Karatasos, K.; Tanis, I.; Tragoudaras, D.; Frick, B.; Anastasiadis, S. Macromolecules **2013**, 46, 2842-2855.

(32) Erber, M.; Khalyavina, A.; Eichhorn, K.-J.; Voit, B. Polymer **2010**, 51, 129-135.

(33) Omara, S. S.; Abdel Rehim, M. H.; Ghoneim, A.; Madkour, S.; Thünemann, A. F.; Turky, G.; Schönhals, A. Macromolecules **2015**, 48, 6562-6573.

(34) Huth, H.; Minakov, A.; Schick, C. Journal of Polymer Science Part B: Polymer Physics **2006**, 44, 2996-3005.

(35) Zhou, D. S.; Huth, H.; Gao, Y.; Xue, G.; Schick, C. Macromolecules 2008, 41, 7662-7666.

(36) Yin, H.; Schönhals, A. Soft Matter **2012**, 8, 9132-9139.

(37) Yin, H.; Schönhals, A. Polymer **2013**, 45, 2067-2070.

(38) Adrjanowicz, K.; Kaminski, K.; Dulski, M.; Jasiurkowska-Delaporte, M.; Kolodziejczyk, K.; Jarek, M.; Bartkowiak, G.; Hawelek, L.; Jurga, S.; Paluch, M. Macromolecules **2014**, 47, 5798-5807.

(39) Zhu, P. W.; Zheng, S.; Simon, G. Macromolecular Chemistry and Physics **2001**, 202, 3008-3017.

(40) Hult, A.; Johansson, M.; Malmström, E. Hyperbranched polymers Advances in Polymer Science **1999**, 143, 1-34.

(41) Voit, B. I. Acta Polymerica **1995**, 46, 87-99.

(42) Carlmark, A.; Hawker, C.; Hult, A.; Malkoch, M. Chemical Society Reviews **2009**, 38, 352-362.

(43) Tomalia, D. A.; Frechet, J. M. J. Journal of Polymer Science: Part A: Polymer Chemistry **2002**, 40, 2719–2728. x

(44) Tomalia, D. A.; Frechet, J. M. J. John Wiley & Sons Inc., NY **2002**, pp. 1–44, 197–208,

(45) Gao, C.; Yan, D. Progress in Polymer Science **2004**, 29, 183-275.

(46) Kim, Y. H.; Webster, O. W. Journal of the American Chemical Society **1990**, 112, 4592-4593.

(47) Voit, B. Journal of Polymer Science Part A: Polymer Chemistry **2005**, 43, 2679-2699..

(48) Voit, B. Journal of Polymer Science Part A: Polymer Chemistry **2000**, 38, 2505-2525.

(49) Tomalia D. A.; Fr´echet J. M. J., Eds.; John Wiley & Sons, Ltd., West Sussex, UK, 2001.

(50) Zheng, Y.; Li, S.; Weng, Z.; Gao, C., Chemical Society Reviews **2015**, 44, 4091-4130.

(51) Jikei, M.; Kakimoto, M., Progress in Polymer Science **2001**, 26, 1233-1285.

(52) Han, K.; Li, W.; Wu, C.; Yu, M. Polymer International **2006**, 55, 898-903.

(53) Sterescu, D. M.; Stamatialis, D. F.; Wessling, M **2008**, 310, 512-521.

(54) Schmidt, L. E.; Schmäh, D.; Leterrier, Y.; Månson, J.-A. E. Rheologica acta **2007**, *46*, 693-701.

(55) Dong, W.; Zhou, Y.; Yan, D.; Li, H.; Liu, Y. Physical Chemistry Chemical Physics **2007**, 9, 1255-1262.

(56) Reul, R.; Nguyen, J.; Kissel, T. Biomaterials **2009**, 30, 5815.

(57) Zhu, J.; Peng, H.; Connor, S. T.; Cui, Y. Small **2009**, 5, 437-439.

(58) Ihre, H.; Johansson, M.; Malmström, E.; Hult, A.; Newkome, G.: In Advances in dendritic macromolecules. JAI: Greenwich, CT **1996**.

(59) Luciani, A.; Plummer, C. J.; Nguyen, T.; Garamszegi, L.; Månson, J. A. E.: Journal of Polymer Science Part B: Polymer Physics **200**4, 42, 1218-1225.

(60) Fréchet. J. M. J. Science **1994**, 263, 1710.

(61) Magnusson, H.; Malmström, E.; Hult, A. Johansson, M. Polymer **2001**, 43, 301-306.

(62) Malmström, E.; Johansson, M.; Hult, A. Macromolecular Chemistry and Physics **1996**, 197, 3199-3207.

(63) Kim. Y. H, W. O. W. Macromolecules **1992**, 25, 5561.

(64) Flory, P. J., Principles of Polymer Chemistry. Cornell University Press, NY **1953**.

(65) Zhang, J.; Xie, S.; Zhang, X.; Lu, Z.; Xiao, H.; Li, C.; Li, G.; Xu, X.; Chen, X.; Bo, Z. Chemical Communications **2017**, 53, 537-540.

(66) Stockmayer W.H. J. Chem. Phys. **1943**, 11, 45.90.

(67) Stockmayer W.H. J. Chem. Phys. **1944**, 12, 125.

(68) Stockmayer W.H. J. Chem. Phys. **1950**, 18, 58

(69) Hölter, D.; Burgath, A.; Frey, H. Acta polymerica **1997**, 48, 30-35.

(70) Gao, C. Doctor Dissertation of Shanghai, Jiao Tong University **2001**.

(71) Gao, C.; Yan, D. Macromolecules **2003**, 36, 613-620.

(72) Gao, C.; Xu, Y.; Yan, D.; Chen, W. Biomacromolecules **2003**, 4, 704-712.

(73) Gao, C.; Yan, D. Macromolecules **2001**, 34, 156-161.

(74) Okpala, C. C.: International Journal of Advanced Engineering Technology **2014**, 12, 12-18.

(75) LeBaron, P. C.; Wang, Z.; Pinnavaia, T. J. Applied Clay Science **1999**, 15, 11-29.

(76) Giannelis, E. P. Advanced Materials **1996**, 8, 29-35.

(77) Okada, A.; Kawasumi, M.; Usuki, A.; Kojima, Y.; Kurauchi, T.; Kamigaito, O. Research Society Symposium Proceedings **1990**, 171, 45-50.

(78) Lee, H.-s.; Fasulo, P. D.; Rodgers, W. R.; Paul, D. R. Polymer **2005**, 46, 11673-11689.

(79) Kornmann, X.; Thomann, R.; Mulhaupt, R.; Finter, J.; Berglund, L. A. Polymer Engineering and Science **2002**, 42, 1815-1826.

(80) Chrissopoulou, K.; Altintzi, I.; Anastasiadis, S.; Giannelis, E.; Pitsikalis, M.; Hadjichristidis, N.; Theophilou, N. Polymer **2005**, 46, 12440-12451.

(81) Chrissopoulou, K.; Altintzi, I.; Andrianaki, I.; Shemesh, R.; Retsos, H.; Giannelis, E.; Anastasiadis, S. Journal of Polymer Science Part B: Polymer Physics **2008**, 46, 2683-2695.

(82) Chrissopoulou, K.; Anastasiadis, S. European Polymer Journal **2011**, 47, 600-613.

(83) Tanaka, T. IEEE Transactions on Dielectrics and Electrical Insulation **2005**, 12, 914-928.

(84) Tanaka, T.; Montanari, G.; Mulhaupt, R. IEEE Transactions on Dielectrics and Electrical Insulation **2004**, 11, 763-784.

(85) Roy M, Nelson J. K, MacCrone R. K, Schadler L. S, Reed C. W, and Keefe R. IEEE Transactions on Dielectrics and Electrical Insulation **2005,** 12, 629..

(86) Tanaka T.; Kozako, M. Fuse N, and. Ohki Y. IEEE Transactions on Dielectrics and Electrical Insulation **2005**, 12, 669.

(87) Hackett, E.; Manias, E.; Giannelis, E. The Journal of chemical physics **1998**, 108, 7410-7415.

(88) Alexandre, M.; Dubois, P. Materials Science and Engineering: R. Reports **2000**, 28, 1-63.

(89) Xu, Y.; Brittain, W. J.; Xue, C.; Eby, R. K. Polymer **2004**, 45, 3735-3746.

(90) Cortés, P.; Fraga, I.; Calventus, Y.; Román, F.; Hutchinson, J. M.; Ferrando, F. Materials **2014**, 7, 1830-1849.

(91) Guessoum, M.; Nekkaa, S.; Fenouillot-Rimlinger, F.; Haddaoui, N. International Journal of Polymer Science **2012**, 2012, 1-9.

(92) Murray, H. H. Reviews in Mineralogy and Geochemistry **1988**, 19, 67-89.

(93) M Murray, H. H. Applied clay mineralogy; Elsevier **2006**.

(94) Murray, H. H.: Applied clay mineralogy. Developments in clay science **2007**, 1, 1-179

(95) Uwins, P. J.; Mackinnon, I. D.; Thompson, J. G.; Yago, A. J. Clays and clay minerals **1993**, 41, 707-717.

(96) Ke, Y.; Stroeve, P. Polymer-Layered Silicate and Silica Nanocomposites; Elsevier: Amsterdam, the Netherlands **2005**.

(97) Carroll, D., Geological Society of America Bulletin **1959**, 70, 749-779.

(98) Dedzo, G. K., Detellier, C. Applied Clay Science **2016**, 130, 33-39.

(99) Detellier, C.; Schoonheydt, R. A. Elements **2014**, 10, 201-206.

(100) Kristóf, J.; Frost, R.L.; Martens, W.N.; Horváth, E. Langmuir **2002**, 18, 1244–1249.

(101) Olejnik, S.; Posner, A.; Quirk, J. Clay Minerals **1970**, 8, 421–434.

(102) Letaief, S.; Detellier, C J. Mater. Chem. **2007**, 17, 1476–1484.

(103) Liu, Q.; Zhang, S.; Cheng, H.; Wang, D.; Li, X.; Hou, X.; Frost, R.L. J. Therm. Anal. Calorim. **2014**, 117, 189–196.

(104) Adams, J.M.; Waltl, G. Clay Miner **1980**, 28, 130–134.

(105) Xie, X.; Hayashi, S. J. Phys. Chem. B **1999**, 103, 5949–5955.

(106) Horváth, E.; Kristóf, J.; Frost, R. L.; Jakab, E.; Mako, E.; Vagvoelgyi, V. Journal of colloid and interface science **2005**, 289, 132-138.

(107) Kelleher, B.P.; Sutton, D.; O'Dwyer, T.F. J. Colloid Interface Sci. **2002**, 255, 219–224.

(108) Komori, Y.; Sugahara, Y.; Kuroda, K. Chemistry of Materials **1999**, 11, 3-6.

(109) Detellier, C.; Letaief, S.: Kaolinite-polymer nanocomposites. Handbook of clay science **2013**, 5, 707-719.

(110) Turhan, Y., Doğan, M., Alkan, M., Industrial & Engineering Chemistry Research **2010**, 49, 1503-1513.

(111) Tunney, J.J., Detellier, C., Chemistry of Materials **1996**, 8, 927-935.

(112) Fafard, J., Detellier, C., Journal of colloid and interface science **2015**, 450, 361-365.

(113) Matsumura, A.; Komori, Y.; Itagaki, T.; Sugahara, Y.; Kuroda, K., Bulletin of the Chemical Society of Japan **2001**, 74, 1153-1158.

(114) Elbokl, T.A., Detellier, C. Canadian journal of chemistry **2009**, 87, 272–279.

(115) Walsh, D.; Zoller, P., Standard pressure volume temperature data for polymers; CRC Press **1995**.

(116) Donth, E.-J., The glass transition: relaxation dynamics in liquids and disordered materials. Springer: Berlin **2001**.

(117) Debenedetti, P. G.; Stillinger, F. H. Nature **2001**, 410, 259-267.

(118) Johari, G.P., The Journal of chemical physics **1973**, 58, 1766.

(119) Johari, G.P.; Goldstein, M. The Journal of chemical physics **1970**, 53, 2372.

(120) Vogel, H., Physikalische Zeitschrift **1921**, 22, 645-646.

(121) Fulcher, G. S., Journal of the American Ceramic Society **1925**, 8, 339-355.

(122) Tammann, G.; Hesse, W., Zeitschrift für Anorganische und Allgemeine Chemie **1926**, 156, 245-257.

(123) Angell, C.A., Journal of Research of the National Institute of Standards and Technology **1997**, 102, 171-85.

(124) Angell, C.A., Science **1995**, 267, 1924-1935.

(125) Maxwell, J. C, Philosophical transactions of the Royal Society of London **1865**, 155, 459-512.

(126) Maxwell, J. C., Philosophical transactions of the Royal Society of London **1868**, 158, 643-657.

(127) Kao, K. C., Dielectric phenomena in solids; Academic press **2004**.

(128) Debye P. "Polar Molecules" the Chemical Catalog Co. Inc. NY **1929**.

(129) Stockmayer, W.H, Pure and Applied Chemistry **1967**, 15, 539.

(130) Schönhals, A. In Dielectric Properties of Amorphous Polymers (Chapter 3) in Dielectric Spectroscopy of Polymeric Materials; Runt, J. P., Fitzgerald, J., Eds.; American Chemical Society Publication, 1999.

(131) Landau L.D,.Lifschitz E.M, Statistical Physics. Textbook of Theoretical Physics, Akademie-Verlag, Berlin, **1979**.

(132) Yin, H.; Schönhals, A.: Broadband dielectric spectroscopy on polymer blends. In Polymer Blends Handbook; Springer **2014**; pp 1299-1356.

(133) Fröhlich H. "Theory of Dielectrics" 2nd Ed. Oxford Unvi. Press, London, N Y **1958**.

(134) Havriliak, S.; Negami, S. Journal of Polymer Science Part C 1966, 14, 99-117; Havriliak, S.; Negami, S. Polymer **1967**, 8, 161

(135) Barton, J. L., Verres Refract **1966**, 20, 328.

(136) Nakajima, T. In 1971 Annual Report, Conference on Electrical Insulation and Dielectric Phenomena **1972**; pp 168-176.

(137) Namikawa, H. Journal of Non-Crystalline Solids **1975**, 18, 173-195.

(138) Dyre, J. C. Journal of Applied Physics **1988**, 64, 2456-2468.

(139) Jonscher, A. K. Nature **1977**, 267, 673-679.

(140) Sangoro, J.; Serghei, A.; Naumov, S.; Galvosas, P.; Kärger, J.; Wespe, C.; Bordusa, F.; Kremer, F.:. Physical Review E **2008**, 77, 051202.

(141) Angell, C.A. Solid state ionics **1983**, 9, 3-16.

(142) Angell, C.A., Solid state ionics **1986**,1872-88.

(143) Angell, C.A., Journal of Review of Physical Chemistry **1992,** 43, 693-717.

(144) Wagner, K. W., Electrical Engineering (Archiv fur Elektrotechnik) **1914**, 2, 371-387.

(145) Sillars, R. J., Institution of Electrical Engineers-Proceedings of the Wireless Section of the nstitution **1937**, 12, 139-155.

(146) Van Beek, L., Progress in dielectrics **1967**, 7, 113.

(147) Hale, D., Journal of materials science **1976**, 11, 2105-2141.

(148) Priou, A., Dielectric properties of heterogeneous materials; Elsevier Science Ltd **1992**.

(149) Asami, K., Progress in Polymer Science **2002**, 27, 1617-1659.

(150) Schawe J. E. K., Thermochchimica Acta **1995**, 1, 260-266.

(151) Herwaaden, S.; Application note for Xsensor's calorimtere chips of XEN-39390 series.

(152) Roe, R.-J. Oxford University Press on Demand **2000**; Vol. 739.

(153) Leng, Y., Materials Characterization: Introduction to Microscopic and Spectroscopic Methods **2008**, 45-77.

(154) Pauw, B. R., Journal of Physics: Condensed Matter **2013**, 25, 383201.

(155) Essawy, H., Colloid Polym. Sci. **2008** 286, 795–803.

(156) Rehim, M. H. A.; Youssef, A. M.; Essawy, H. A., Mater. Chem.Phys. **2010**, 119, 546–552.

(157) Letaief, S.; Detellier, C. Journal of Thermal Analysis and Calorimetry **2011**, 104, 831-839.

(158) Qiao, Q.; Yang, H.; Liu, J.-L.; Zhao, S.-P.; Ren, X.-M., Dalton Transactions **2014**, 43, 5427-5434.

(159) Gardolinski, J. E.; Peralta-Zamora, P.; Wypych, F. Journal of Colloid and Interface Science **1999**, 211, 137-141.

(160) Tunney, J. J., Detellier, C. Canadian Journal of Chemistry **1997**, 75, 1766-1772.

(161) Zhang, S.; Lui, Q.; Cheng, H.; Li, X.; Zeng, F.; Frost, R. L., Journal of Colloid and Interface Science **2014**, 430, 345-350.

(162) Magaraphan, R.; Lilayuthalert, W.; Sirivat, A.; Schwank, J. W. Composites Science and Technology **2001**, 61, 1253-1264.

(163) Komori, Y, Sugahara Y, Kuroda K., Applied Clay Science **1999**, 15, 241-252.

(164) Klaykruayat, B.; Siralertmukul, K.; Srikulkit, K., Carbohydrate Polymers **2010**, 80, 197-207.

(165) Zhang, L.; Yang, H. K.; Shi, G., E-Polymers **2010**, 10, 1516-1526.

(166) Hu, X.-L.; Hou, G.-M.; Zhang, M.-Q.; Rong, M.-Z.; Ruan, W.-H.; Giannelis, E. P., Journal of Materials Chemistry **2012**, 22,18961-18967.

(167) Rehab, A.; Salahuddin, N., Materials Science and Engineering **2005**, 399, 368-376.

(168) Corcione, C. E.; Frigione, M., Materials **2012**, 5, 2960-2980.

(169) Madkour, S.; Yin, H.; Füllbrandt, M.; Schönhals, A., Soft Matter **2015**, 11, 7942-7952.

(170) Schönhals, A.; Goering, H.; Schick, C.; Frick, B.; Zorn, R., Journal of Non-Crystalline Solids **2005**, 351, 2668 – 2677.

(171) Elmahdy, M. M.; Chrissopoulou, K.; Afratis, A.; Floudas, G.; Anastasiadis, S. H., Macromolecules **2006**, 39, 5170–5173.

(172) Androulaki, K.; Chrissopoulou, K.; Prevosto, D.; Labardi, M.; Anastasiadis, S. H., ACS Applied Materials & Interfaces 2015, 1, 43006.

(173) Elrehim, M. A.; Said, S.; Ghoneim, A.; Turky, G., Macromolecul Symposia, Wiley Online Library **2007**, 254, 1-8.

(174) Roling, B.; Happe, A.; Funke, K.; Ingram, M. D., Physical Review Letters **1997**, 78, 2160-2163.

(175) Sidebottom, D. L., Physical Review Letters **1999**, 82, 3653-3656.

(176) Zielniok, D.; Eckert, H.; Cramer, C. Physical Review Letters **2008**, 100, 035901.

(177) MacDonald, J. R., Journal of Non-Crystalline Solids **1996**, 197, 83-110.

(178) Iacob, C.; Sangoro, J.; Serghei, A.; Naumov, S.; Korth, Y.; Kärger, J.; Friedrich, C.; Kremer, F., The Journal of Chemical Physics **2008**, 129, 234511.

(179) Serghei, A.; Tress, M.; Sangoro, J.; Kremer, F., Physical Review B **2009**, 80, 184301.

(180) Dantras, E.; Dandurand, J.; Lacabanne, C.; Caminade, A. M. Majoral, J. P., Macromolecules **2004**, 37, 2812–2816.

(181) Wang, Y.; Fan, F.; Agapov, A. L.; Saito, T.; Yang, J.; Yu, X.; Hong, K.; Mays, J.; Sokolov, A. P. Polymer 2014, 55 4067-4076.

(182) Wang, Y.; Agapov, A. L.; Fan, F.; Hong, K.; Yu, X.; Mays, J.; Sokolov, A. P., Physical Review Letters **2012**, 108, 088303.

(183) Plazek, D. J.; O'Rourke, V. M, Journal of Polymer Science Part B: Polymer Physics **1971**, 9, 209-243.

(184) Plazek, D. J., Polymer Journal **1980**, 12, 43-53.

(185) Plazek, D. J.; Schlosser, E.; Schönhals, A.; Ngai, K. L. J. Chem. Phys. **1993**, 98, 4688.

(186) Schönhals, A., Macromolecules **1993**, 26, 1309-1312.

(187) Ding, Y.; Sokolov, A. P., Macromolecules **2006**, 39, 3322-3326.

(188) Ngai, K. L.; Schönhals, A.; Schlosser, E., Macromolecules, 1992, 25, 4915.

(189) Sokolov, A. P.; Schweizer, K. S. Phys. Rev. Lett. **2009**, 102, 248301.

(190) Mizuno, F.; Belieres, J.-P.; Kuwata, N.; Pradel, A.; Ribes, M., Angell, C. A. J. Non-Cryst. Solids **2006**, 352, 5147.

(191) Fahmy, A.; Mix, R.; Schönhals, A.; Friedrich, J. F. Plasma Processes and Polymers **2011**, 8, 147-159.

(192) Jacobs, J. D.; Koerner, H.; Heinz, H.; Farmer, B. L.; Mirau, P.; Garrett, P. H.; Vaia, R. A., The Journal of Physical Chemistry B **2006**, 110, 20143-20157.

(193) Liu, Q.; Li, X.; Cheng, H. Applied Clay Science **2016**, 124, 175-182.

(194) Frey, M.; Didzoleit, H.; Gainaru, C.; Böhmer, R., The Journal of Physical Chemistry B **2013**, 117, 12164-12174

(195) Frenzel, F.; Folikumah, M. Y.; Schulz, M.; Anton, A. M.; Binder, W. H.; Kremer, F., Macromolecules **2016**, 49, 2868-2875.

(196) Wojnarowska, Z.; Knapik, J.; Díaz, M.; Ortiz, A.; Ortiz, I.; Paluch, M., Macromolecules **2014**, 47, 4056-4065.

(197) Kreuer, K. D.; Rabenau, A.; Weppner, W. Angewandte Chemie International Edition in English **1982**, 21, 208-209.

(198) Marx, D., ChemPhysChem **2006**, 7, 1848-1870.

(199) Wojnarowska, Z.; Paluch, K. J.; Shoifet, E.; Schick, C.; Tajber, L.; Knapik, J.; Wlodarczyk, P.; Grzybowska, K.; Hensel-Bielowka, S.; Verevkin, S. P. Journal of the American Chemical Society **2015**, 137, 1157-1164.

(200) Agmon, N., Chemical Physics Letters **1995**, 244, 456-462.

(201) Fan, Fei, "Ion transport in polymer electrolytes" PhD diss., University of Tennessee **2015**. http://trace.tennessee.edu/utk_graddiss/3414.

(202) Paluch, M.; Wojnarowska, Z.; Hensel-Bielowka, S., Physical Review Letters **2013**, 110, 015702.

(203) Howell, F.; Bose, R.; Macedo, P.; Moynihan, C., The Journal of Physical Chemistry **1974**, 78, 639-648.

(204) Agapov, A. L.; Sokolov, A. P., Macromolecules **2011**, 44, 4410-4414.

(205) Omara, S. S.; Turky, G.; Ghoneim, A.; Thünemann, A. F.; Rehim, M. H. A.; Schönhals, A., Polymer **2017**, 121, 64-74.

(206) Turky, G.; Sangoro, J.; Abdel Rehim, M.; Kremer, F.: Journal of Polymer Science Part B: Polymer Physics **2010**, 48, 1651-1657.

(207) Tanis, I.; Tragoudaras, D.; Karatasos, K.; Anastasiadis, S., The Journal of Physical Chemistry B **2009**, 113, 5356-5368.

(208) Yik, B. J.; Guo, M.; Kwon, Y.; Goodson III, T., The Journal of Physical Chemistry C **2017**, 121, 7108-7122.

(209) Wojnarowska, Z.; Feng, H.; Fu, Y.; Cheng, S.; Carroll, B.; Kumar, R.; Novikov, V. N.; Kisliuk, A. M.; Saito, T.; Kang, N.-G., Macromolecules **2017**, 50, 6710-6721.

9. PUBLICATIONS

List of Peer-Reviewed Publications:

1. Omara, S. S.; Turky, G.; Ghoneim, A.; Thünemann, A. F.; Rehim, M. H. A.; Schönhals, A.: *Hyperbranched Poly(amidoamine)/Kaolinite Nanocomposites: Structure and Charge Carrier Dynamics. Polymer*. 121, 64-74, (2017).

2. Omara, S. S.; Abdel Rehim, M. H.; Ghoneim, A.; Madkour, S.; Thünemann, A. F.; Turky, G.; Schönhals, A.: *Structure–property relationships of hyperbranched polymer/kaolinite nanocomposites.* Macromolecules. 48, 6562-6573, (2015).

3. Omara, S. S.; Schönhals, A.: "*In situ polymerization of hyperbranched poly(amidoamine) / Kaolinite nanocomposites: A dielectric study ".* In progress.

4. Omara, S. S.; Turky, G.; Thünemann, A. F.; Rehim, M. H. A.; Schönhals, A.: *Dielectric Study of Molecular Mobility in Hybrane/ Kaolinite Nanocomposites.* In progress.

List of Talks:

1. Omara, S.S, Abdel Rehim, M., Turky G, and Schönhals A., DPG- spring conference, TU Berlin. 15 March. (2018).

2. Omara S.S Schönhals, A.: "*Preparation, characterization and electrical properties of some nanocomposites based on multifunctional polymers"* held as part of the doctoral seminar at Federal Institute for Materials Research and Testing (BAM) (2104).

3. Omara, S. S.; Turky, G.; Thünemann, A. F.; Rehim, M. H. A.; Schönhals, A. "*Dynamics of hyperbranched polymers in the confinement of nanofillers"* held as part of the doctoral seminar at Federal Institute for Materials Research and Testing (BAM) (2105).

List of posters:

1. S. Omara, M. Abdel Rehim, S.Madkour , G.Turky and A. Schönhals . DPG conference TU Berlin. 15 March. (2018).
2. S. Omara, M. Abdel Rehim, A. Ghoneim, S.Madkour , G.Turky and A. Schönhals . Polydays conference. University of Potsdam, Germany 26. September (2016).
3. S. Omara, M. Abdel Rehim, A. Ghoneim, S.Madkour , G.Turky and A. Schönhals . DPG conference TU Berlin. 15 March. (2015).

4. G. Turky. S. Omara, M. Abdel Rehim, A. Ghoneim, and A. Schönhals. Poster in 8th ECNP International Conference on Nanostructured Polymers and Nanocomposites Dresden, 16-19 Sept. (2014).